Cardiac MRI to Investigate Proinflammatory Epicardial Adipose Tissue, Macrophage Involvement, and Treatment Response in Cardiometabolic HFpEF

A

Dissertation

Presented to

The Faculty of the School of Engineering and Applied Science

University of Virginia

---

in partial fulfillment

of the requirements for the degree

Doctor of Philosophy

by

Julia Bresticker

May 2025

APPROVAL SHEET

This

Dissertation

is submitted in partial fulfillment of the requirements
for the degree of

Doctor of Philosophy

Author: Julia Bresticker

This Dissertation has been read and approved by the examing committee:

Advisor: Frederick Epstein

Advisor:

Committee Member: Craig Meyer

Committee Member: Amit Patel

Committee Member: Shayn Peirce-Cottler

Committee Member: Matthew Wolf

Committee Member:

Committee Member:

Accepted for the School of Engineering and Applied Science:

Jennifer L. West, School of Engineering and Applied Science

May 2025

Abstract

Heart failure with preserved ejection fraction (HFpEF) is a complex and increasingly prevalent syndrome closely linked to obesity, metabolic dysfunction, and inflammation, yet lacks effective therapies. HFpEF is characterized by visceral adiposity, coronary microvascular disease (CMD), and diastolic dysfunction, with the metabolic alteration-driven phenotype – cardiometabolic HFpEF – emerging as the most prevalent form[1,2]. Epicardial adipose tissue (EAT) – the visceral fat depot in direct contact with the myocardium and sharing an unobstructed microcirculation – has emerged as a key mediator of the adverse cardiac effects of systemic metabolic and inflammatory conditions, making it a potential therapeutic target[3].

The overarching goal of this dissertation was to develop and apply advanced magnetic resonance imaging (MRI) methods to: (1) establish noninvasive biomarkers of proinflammatory EAT and their relationships to underlying tissue biology, (2) investigate how sodium-glucose cotransporter-2 (SGLT2) inhibition modulates EAT inflammation in the setting of cardiometabolic HFpEF, and (3) identify the role of macrophage-derived inducible nitric oxide synthase (NOS2) in HFpEF pathogenesis.

The goal of **Aim 1 (Chapter 2)**, was to develop an accelerated MRI method for simultaneous mapping of EAT fatty acid composition (FAC) and T_1 relaxation time in mice. This technique enabled spatially resolved quantification of saturated (SFA), monounsaturated (MUFA), and polyunsaturated fatty acid (PUFA) content along with T_1 relaxation time in EAT and subcutaneous adipose tissue (SAT). In mouse models of diet-induced obesity, increased EAT SFA fraction and reduced T_1 values were associated with histologic and molecular features of

inflammation, including greater macrophage infiltration, proinflammatory cytokine expression, and adipocyte hypertrophy.

The goal of **Aim 2 (Chapter 3)**, was to use cardiac MRI (CMR) to assess the impact of early versus late empagliflozin (EMPA) treatment in a mouse model of early-stage cardiometabolic HFpEF induced by a high-fat high-sucrose diet (HFHSD). Early EMPA treatment prevented EAT accumulation, improved myocardial perfusion reserve (MPR), preserved diastolic function, and reduced markers of adipose tissue inflammation, including $NOS2^{+}$ M1 macrophages. In contrast, late EMPA treatment prevented EAT expansion but did not reverse impairments in MPR, diastolic function, or EAT inflammatory status, highlighting the importance of early intervention with SGLT2 inhibitors.

The goal of **Aim 3 (Chapter 4)**, was to test hypothesis that NOS2 in macrophages mediates CMD and diastolic dysfunction in a mouse model of early stage cardiometabolic HFpEF. Using a LysM-Cre *Nos2* knockout mouse model ($Nos2^{LysM\text{-}KO}$) fed an HFHSD, we found that macrophage-specific deletion of NOS2 preserved coronary vasodilation in response to adenosine and myocardial perfusion despite the presence of obesity and glucose intolerance. However, diastolic dysfunction persisted, suggesting that NOS2 drives microvascular, but not diastolic, dysfunction and implicating additional non-macrophage sources of NOS2 in HFpEF pathogenesis.

Together, these studies support a model in which proinflammatory EAT – marked by elevated SFA, increased macrophage infiltration, and adipocyte hypertrophy – may contribute to myocardial and vascular dysfunction. This work highlights the utility of MRI for noninvasively assessing proinflammatory EAT, establishes early EMPA treatment as a modulator of EAT biology and an effective therapy in preventing CMD and diastolic dysfunction in cardiometabolic

HFpEF, and identifies macrophage NOS2 as a key contributor to coronary microvascular dysfunction in cardiometabolic HFpEF.

Table of Contents

Figures and Tables

Chapter 1: Background

1.1 Magnetic resonance imaging (MRI)

MRI is a noninvasive imaging technique based on the principles of nuclear magnetic resonance (NMR), widely used in both clinical and preclinical settings. Unlike imaging modalities that use ionizing radiation, MRI provides excellent soft tissue contrast and enables both anatomical visualization and quantitative functional imaging, making it a powerful tool for diagnosis and research.

1.1.1 MR physics

The phenomenon of NMR arises in atoms with an odd number of protons and/or neutrons, which possess the property known as spin angular momentum. Atoms with spin have an associated magnetic dipole moment, $\vec{\mu}$, analogous to a charged sphere spinning about its axis, giving rise to a current loop and corresponding magnetic moment[4]. While several atoms in the human body exhibit nuclear spin, ^{1}H is the is the most commonly used for in vivo imaging due to its abundance in the human body – primarily in the form of water and fat. The source of the MR signal is due to the interaction of these nuclei with a static magnetic field ($\mathbf{B_0}$) and a radiofrequency (RF) field ($\mathbf{B_1}$). When nuclear spins are subjected to a $\mathbf{B_0}$ field in the *z* (longitudinal) direction, the spins align in the direction of $\mathbf{B_0}$, giving rise to a bulk magnetization vector **M**.

At thermal equilibrium, **M** and $\mathbf{B_0}$ will be oriented in the same direction. If **M** is made to point in a different direction than $\mathbf{B_0}$, precessional behavior of **M** about $\mathbf{B_0}$ will occur at the Larmor frequency (in Hz), given by

$$f = \frac{\gamma}{2\pi} B_0 \tag{1.1}$$

where γ is the gyromagnetic ratio unique to each nuclear species and for ^{1}H, $\gamma/2\pi$ = 42.58 MHz/T. Application of an oscillating RF pulse at the Larmor frequency enables magnetization "excitation",

which classically, is the rotation of **M** by some flip angle, α, away from its equilibrium position along the *z*-axis. The magnitudes of the magnetization after the RF excitation are

$$M_{xy} = M_0 \sin(\alpha) \tag{1.2}$$

$$M_z = M_0 \cos(\alpha) \tag{1.3}$$

where M_0 is the longitudinal magnetization (M_z) prior to excitation[4]. Following excitation, **M** eventually returns to its equilibrium state. Thus, the transverse component M_{xy} decays away while the longitudinal component M_z regrows. The relaxation time constants, T_1 and T_2, characterize this return to equilibrium[5].

1.1.2 Relaxation

Longitudinal (T_1)

The longitudinal component of the magnetization following an excitation pulse can be described using a solution to the Bloch equation, which governs the dynamics of the nuclear magnetization

$$M_z = M_0 + (M_z(0) - M_0)e^{-\frac{t}{T_1}} \tag{1.4}$$

where $M_z(0)$ is the longitudinal magnetization at time zero, directly following the RF pulse. **Figure 1** plots the longitudinal magnetization when $M_z(0) = 0$ (i.e., 90° excitation pulse). Thus, T_1 is approximately the time it takes for M_z to regrow to 63% of its original value[6].

Physically, the longitudinal relaxation time, T_1 – also referred to as the thermal or spin-lattice time constant – involves the exchange of energy between spins and their external environment. Energy transfer occurs through collisions, rotations, and other interactions between nuclei that take place at the resonant frequency of the spins. Since greater energy exchange is required at higher frequencies, this relaxation effect will take longer at higher field strengths, thus, T_1 values lengthen with increasing B_0. It is important to note that fat (lipids), with closely packed molecules and slow molecular tumbling rates, will have more efficient energy exchange and thus,

shorter T_1. Whereas water, with further spaced molecules and fast tumbling, will have less efficient energy exchange and thus, longer T_1.

Transverse (T_2)

The transverse component of the magnetization is

$$M_{xy} = M_{xy}(0)e^{-\frac{t}{T_2}} \tag{1.5}$$

where T_2, the spin-spin time constant, characterizes the time it takes the transverse component to decay or dephase[6]. Following a simple exponential decay, T_2 is the time it takes the transverse component of the magnetization to fall to 37% of its original value (**Figure 1**). The same processes that contribute to T_1 relaxation also contribute to T_2 relaxation. However, in addition to energy exchange with its external environment, spins can experience local static magnetic field disturbances resulting in a spread of resonant frequencies and dephasing. These effects often dominate the T_2 relaxation process, therefore $T_2 \leq T_1$. Slow molecular tumbling in large, dense solids results in rapid dephasing and short T_2 decay, whereas relatively mobile spins, such as those in liquid form, exhibit much slower decay and have a long T_2.

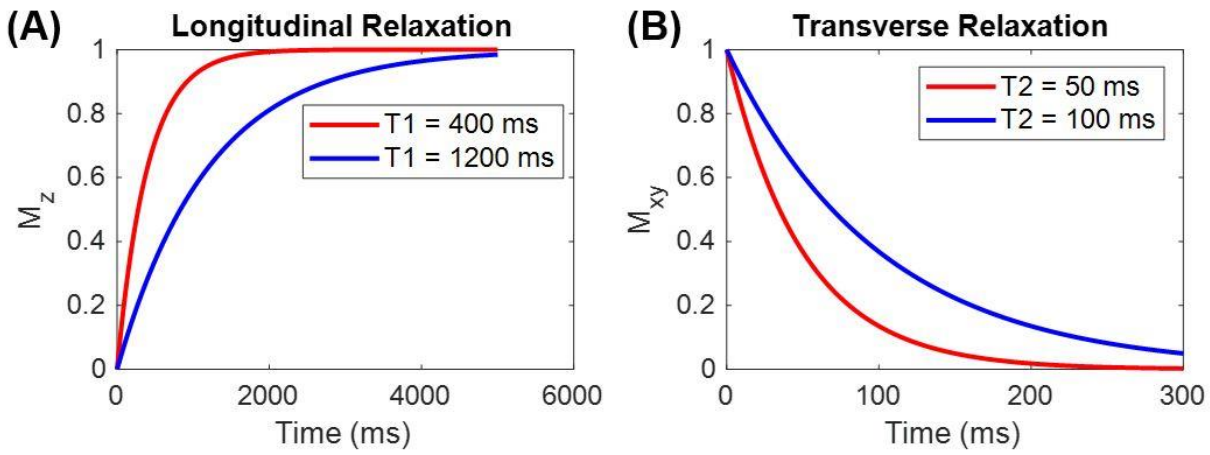

Figure 1 – Simulated (A) longitudinal and (B) transverse relaxation curves following a 90° excitation pulse for tissues with different T_1 and T_2 times.

In practice, transverse relaxation is further influenced by additional dephasing from local B_0 field inhomogeneities leading to an accelerated decay of the transverse magnetization characterized by T_2^*. This effective relaxation time (T_2^*) is always shorter than T_2 and represents the combined effects of spin-spin interactions and reversible magnetic field variations[7].

1.1.3 Imaging acquisition

In order to generate an image, the MR signal must contain spatial information. The spatial distribution information comes from the addition of three gradient fields – G_x, G_y, and G_z – that vary both spatially and temporally and enable the imaging of the nuclear magnetization. These gradient fields create a linear variation in the longitudinal magnetic field strength such that the magnetic field will vary with time and position and can be expressed as $B(x, y, z, t) = B_0 + G_x(t)x + G_y(t)y + G_z(t)z$.

For 2D imaging, the received time signal from an excited plane can be expressed as:

$$s(t) = \int_x \int_y m(x, y) e^{-i2\pi[k_x(t)x + k_y(t)y]}\, dx\, dy \tag{1.6}$$

where

$$k_x(t) = \frac{\gamma}{2\pi}\int_0^t G_x(\tau)d\tau \tag{1.7}$$

and

$$k_y(t) = \frac{\gamma}{2\pi}\int_0^t G_y(\tau)d\tau \tag{1.8}$$

are the integrals of the gradient waveforms that are expressed in units of spatial frequency (cycles/mm)[4].

To construct an MR image, the goal is to measure appropriate $s(t)$ such that $m(x, y)$ can be determined. Equation 1.6 reveals that at any given time, $s(t)$ equals the 2D Fourier transform (FT) of $m(x, y)$ at some spatial frequency, (k_x, k_y). Therefore, the total recorded signal maps to a trajectory through spatial frequency (Fourier) space as determined by the time integrals of the gradient waveforms. This frequency space is referred to as "k-space" (**Figure 2**).

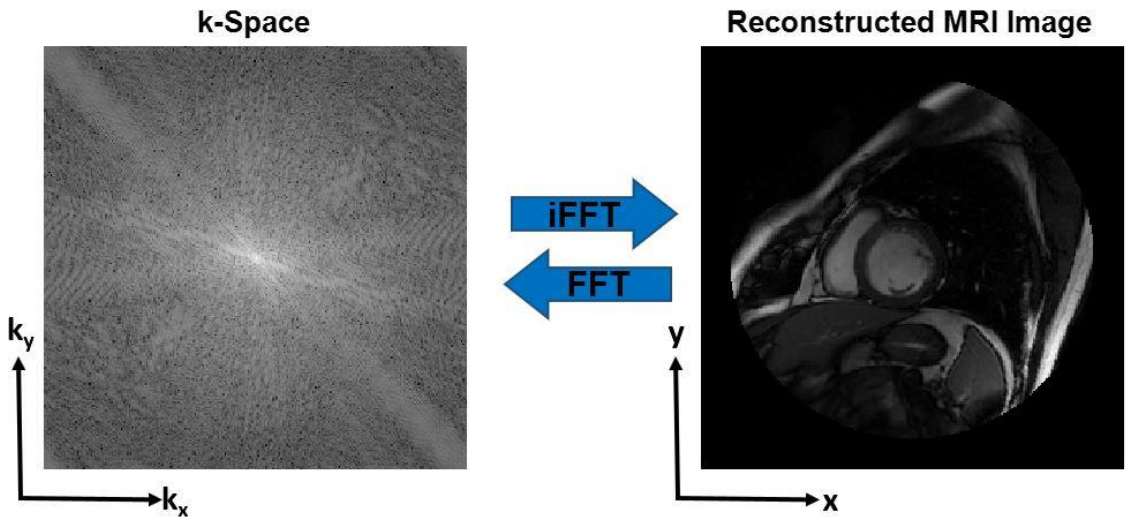

Figure 2 – MRI data are acquired in sptial frequency space (k-space), and the final image is reconstructed via an inverse fast Fourier transform (iFFT).

1.1.4 K-space sampling

K-space is an array of numbers representing spatial frequencies in an image. Sufficient sampling of k-space is necessary for proper image generation. The image field of view (FOV) is governed by the sampling rate along k_x and k_y, whereas the image resolution is governed by the maximum spatial frequencies, k_{xmax} and k_{ymax}, which determine the width of k-space sampling. A "fully sampled" acquisition follows the Nyquist-Shannon sampling rule, therefore acquiring less data – "undersampling" – results in aliasing artifacts in the image.

The cartesian grid of k-space has axes k_x and k_y which correspond to x and y axes of the image, but individual points in k-space don't map to individual pixels in an image. Instead, locations in k-space map to spatial frequencies in the MR image with data near the center of k-space containing information about the general shapes and contours in the image (low frequency) and data near the edges containing information about the edges and details of the image (high frequency)[8]. Filling this grid of k-space is commonly done by acquiring data along the cartesian

grid. However, non-Cartesian sampling trajectories, such as radial sampling, have also been widely applied as they offer many advantages over Cartesian sampling often due to the varying phase-encoding direction and dense sampling of the center of k-space (**Figure 3**).

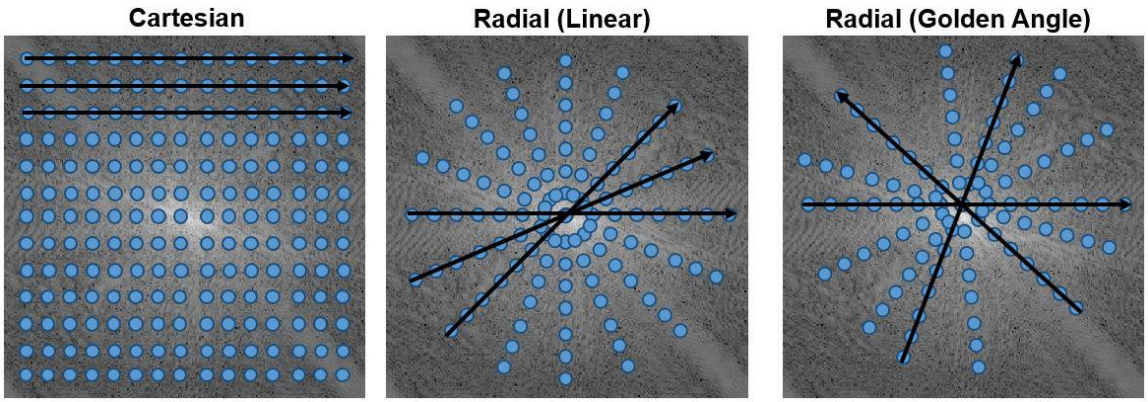

Figure 3 - Examples of k-space sampling trajectories: Cartesian (left), radial with linear angular increments (center), and radial with golden angle increments (right). Radial trajectories oversample the center of k-space and reduce motion sensitivity and aliasing artifacts.

Golden angle radial sampling

Radial acquisitions offer flexibility in the design of how radial spokes are rotated from one to the next. Whereas traditional radial imaging rotates the spokes linearly so they are evenly spaced with each increment, golden angle radial sampling rotates each spoke by a "golden angle" (e.g. 111.25° for 2D radial sampling)[9], therefore the i^{th} spoke out of N_r spokes is calculated as

$$\theta_i = mod\left((i-1) * \pi * \frac{\sqrt{5}-1}{2}, \pi\right), i = 1, 2, \ldots N_r \quad (1.9)$$

When the number of golden angle radial spokes equals one of the Fibonacci numbers, the acquired k-space has uniform coverage (**Figure 4**)[9]. A major advantage of this type of trajectory is the

incoherent undersampling property. Incoherent undersampling in this context implies that undersampling-induced artifacts resemble added noise, such that the bulk image can still be visualized in the presence of these artifacts[9]. This can enable faster, undersampled image acquisitions with advanced denoising techniques used during image reconstruction. Despite the advantages, golden angle sampling has its limitations, including prolonged reconstruction time (due to k-space regridding prior to FT), and susceptibility to gradient delay and eddy current artifacts.

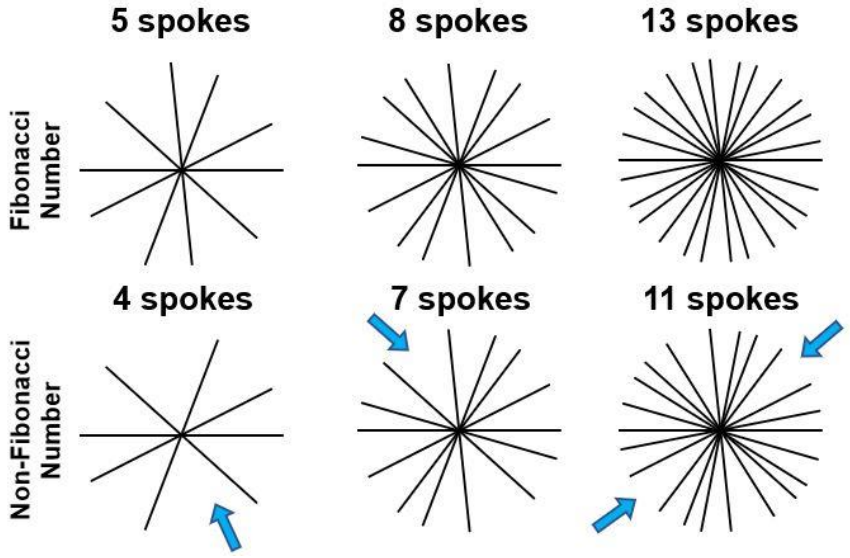

Figure 4 - Golden angle radial sampling produces uniform k-space coverage when the number of spokes corresponds to a Fibonacci number (top row), while non-Fibonacci numbers (bottom row, arrows) result in uneven coverage.

Recently, the rotated stack-of-stars trajectory has emerged as a more advanced golden angle radial sampling scheme[10]. In this trajectory, radial sampling is employed in-plane ($k_x - k_y$) and a smaller golden-angle rotation is implemented along the partition-encoding direction, thus creating additional varying aliasing patterns along the partition direction which improves the

incoherent undersampling property. The partition angle offsets for a given partition index *j* out of N_{PE} partitions are given by

$$\phi_j = mod\left((j-1) * \frac{\pi}{N_r} * \frac{\sqrt{5}-1}{2}, \frac{\pi}{N_r}\right), j = 1,2, \dots N_{PE} \quad (1.10)$$

1.1.5 Pulse sequences

MRI pulse sequences are specific combinations of RF pulses and gradient waveforms that are used to generate images with different contrasts. Generally, pulse sequences have three components: (1) preparatory modules that alter the properties of the magnetization prior to acquisition, (2) acquisition pulse(s) and gradients that generate an MR signal, and (3) recovery time involving gradient spoilers or rewind gradients to eliminate remaining phase coherence before the sequence repeats.

Gradient echo (GRE) imaging

Gradient echo (GRE) imaging is the basis of many applications in MRI. Pulse sequence elements used to generate an MR signal in GRE imaging are a single RF excitation pulse in combination with systematic gradient dephasing of the transverse magnetization and subsequent rephasing such that the net gradient area is zero at each echo time (TE), corresponding the zero-crossing of k-space[11]. Mechanisms of dephasing such as field inhomogeneity or susceptibility are not refocused with the gradient echo. Therefore, GRE imaging is sensitive to T_2^* effects.

Inversion recovery (IR) prepped sequences

For inversion recovery (IR) prepped sequences, a 180° RF pulse is applied prior to acquisition that inverts the initial longitudinal magnetization of all tissues in the imaged slice or volume antiparallel to the main magnetic field. During an interval TI (inversion time), the inverted tissues undergo T_1 relaxation. When signal acquisition occurs at TI, the initial longitudinal magnetizations

of different tissues are separated based on their different intrinsic T_1 relaxation times, thus creating T_1-weighted image contrast[12].

1.1.6 T_1 mapping

T_1 mapping is a pixel-by-pixel method of quantifying T_1 relaxation time of soft tissues. It has shown promise in characterizing diffuse and focal myocardial diseases, including edema, fibrosis, and infiltrative diseases, and is thus used commonly in cardiac applications. While numerous techniques have been developed for the purpose of T_1 mapping, the methods described by Look and Locker have been the basis for several commonly used cardiac T_1 mapping sequences today[13]. In the Look-Locker approach, signals are acquired repeatedly after an inversion pulse with a distinct TI, to obtain different T_1 weighted images. The image acquisition process is repeated after $5*T_1$ to allow for complete recovery of the magnetization between each inversion pulse. These images are then fit to an exponential inversion recovery curve on a pixel-wise basis (**Figure 5**). The signal recovers with an apparent T_1 time, T_1^*, due to repetitive RF excitations and readouts altering the magnetization as it recovers. Therefore, the true T_1 is determined analytically by applying a Look-Locker correction factor[14].

Cardiac motion necessitates the use of modified Look-Locker inversion recovery (MOLLI) techniques that use electrocardiographic (ECG) gating and single-shot or segmented acquisitions at end-diastole in consecutive cardiac cycles separated by multiples of the RR interval[15]. **Figure 5** illustrates an example MOLLI sequence with T_1 differences between myocardium, blood, and fat surrounding the heart seen as signal intensity differences in the images at different TIs and in the rate of signal regrowth in the exponential recovery curves[16].

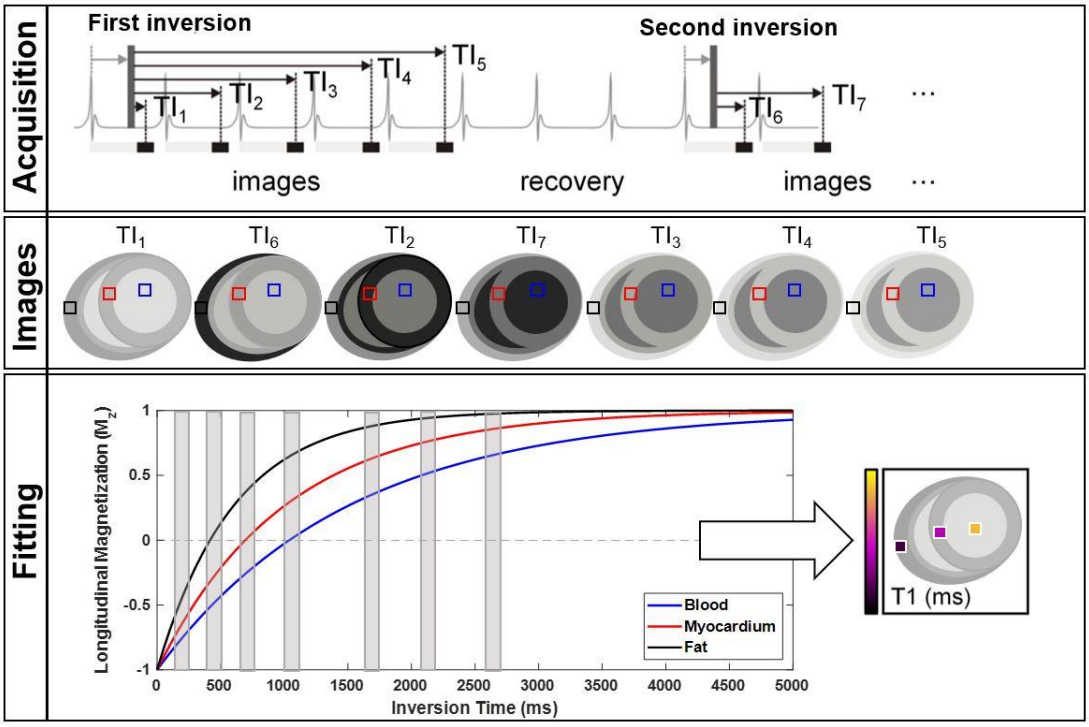

Figure 5 - T_1 mapping using a modified Look-Locker inversion recovery (MOLLI) sequence. Multiple images are acquired at different inversion times (TI) following an inversion pulse, and pixel-wise signal intensities are fit to an exponential recovery curve to calculate T_1 values. The example shows distinct T_1 relaxation curves for blood (blue box), myocardium (red box), and fat (black box). Schematic adapted from Reiter et al.[16]

1.1.7 Chemical shift-encoded MRI

Chemical shift

In MRI, the resonance frequency of a nucleus is determined not only by the external magnetic field, but also by the local magnetic environment created by surrounding electrons. This phenomenon, known as chemical shift, arises because electrons partially shield the nucleus from the external magnetic field. This shielding factor σ, gives way to an induced magnetic field $B_{ind} = \sigma B_0$ such that the local effective magnetic field experienced by the nucleus is $B_{loc} = B_0(1 - \sigma)$. The extent of this shielding depends on the molecular environment in which a nucleus resides. As

a result, nuclei in different chemical environments resonate at slightly different frequencies, even within the same magnetic field.

Chemical shift is the basis for magnetic resonance spectroscopy and imaging. It enables the discrimination of distinct molecular species based on their unique resonant frequencies. The chemical shift (δ) is typically measured in parts per million (ppm) such that the frequency shift Δf in Hz scales linearly with the strength of the magnetic field[17]

$$\Delta f = \frac{\gamma}{2\pi} B_0 \times \Delta\delta[\text{ppm}] \times 10^{-6} \quad (1.11)$$

For example, a chemical shift of 3.5 ppm between two species corresponds to a frequency shift of approximately 448 Hz at 3T or 1400 Hz at 9.4T.

In biological tissues, the chemical shift between water and fat protons is especially relevant. Water molecules contain hydrogen atoms bound to oxygen, while fat is composed mainly of triglycerides with hydrogen atoms in a variety of chemical environments. These environments provide greater electron shielding in fat than in water, which causes fat protons to resonate at a slightly lower frequency. The main fat resonance, from methylene protons, is typically about 3.5 ppm lower than the water resonance (**Figure 6**).

Fat/Water MRI

The frequency offset between fat and water species leads to a difference in their phase evolution over time. By acquiring MR images at specific TEs when the signals from fat and water are either in-phase or out-of-phase, it is possible to separate the signal based on their relative signal contributions (**Figure 6**). This concept is the basis of Dixon-based imaging techniques, first introduced in the 1980s[18]. Early implementations used two echo times corresponding to phase shifts of 0 and π (in-phase and out-of-phase). This evolved into three-point Dixon methods, which add a third echo with phase shift of -π to account for off-resonance effects[19]. Modern approaches

use multiple (>3) echoes and apply complex signal models to generate separate fat-only and water-only images, with corrections for confounding effects such as T_2^* decay and B_0 inhomogeneities.

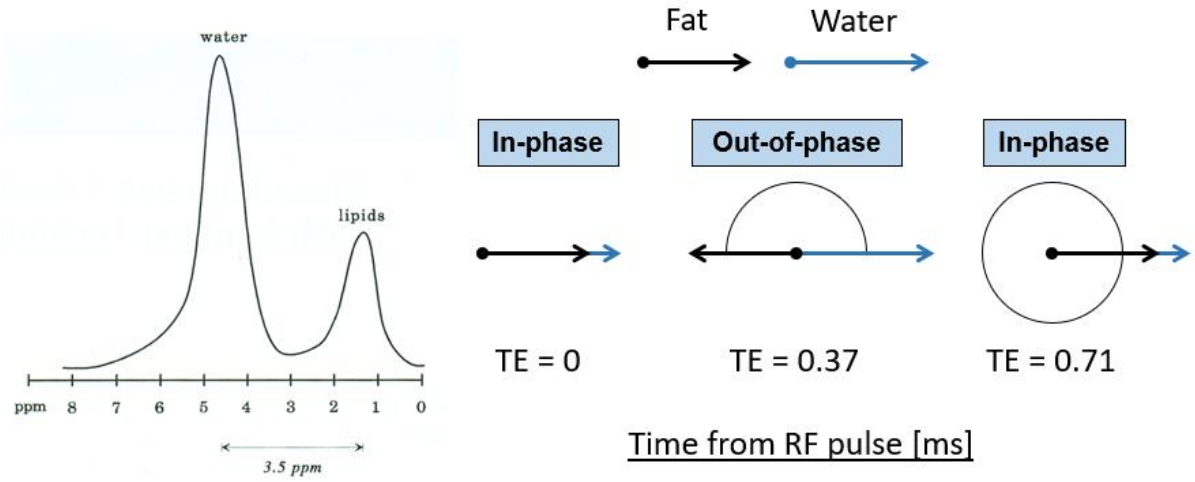

Figure 6 – Water and the main fat resonance (methylene) precess at different frequencies (~3.5 ppm apart), enabling signal separation based on their phase differences at specific echo times (TEs). TEs correspond to in-phase and out-of-phase conditions at 9.4T.

Importantly, fat/water MRI techniques allow not only qualitative separation but also quantitative estimation of tissue fat content. The proton density fat fraction (PDFF) – defined as the ratio of fat signal to the combined fat and water signal, corrected for confounding factors – is a widely used metric that reflects the fraction of hydrogen nuclei attributable to fat within a voxel. PDFF serves as an established biomarker of tissue triglyceride content, most commonly used to assess intracellular fat in the liver[20].

To accurately estimate the PDFF, several confounding factors must be addressed, including B_0 inhomogeneity, T_2^* decay, and the spectral complexity of fat[21]. Traditional models often represent fat as a single resonance near 1.3 ppm, but this captures only about 65% of the total fat

proton signal[22]. In reality, fat stored as triglycerides produces multiple resonance peaks from chemically distinct proton groups. Multi-peak spectral models more accurately reflect this complexity, reducing bias in PDFF quantification[23].

Multi-resonance model of fat

Fat in tissues is primarily stored as triglycerides, which consist of a glycerol backbone esterified with three fatty acid chains. These chains vary in carbon length and degree of unsaturation—classified as saturated (no double bonds), monounsaturated (one double bond), or polyunsaturated (two or more double bonds). This molecular variability alters the local chemical environment of hydrogen nuclei, giving rise to a complex fat spectrum composed of multiple resonance peaks rather than a single fat peak (**Figure 7**).

Each peak corresponds to protons in a specific chemical environment, such as methyl, methylene, or olefinic, among others (**Figure 7**). The number of protons in each group—and thus the relative amplitude of each peak—is determined by the composition of the triglyceride. Specifically, the number of double bonds per molecule (*ndb*), number of methylene-interrupted double bonds (*nmidb*), and average chain length (*cl*) govern the distribution of these protons. For example, each triglyceride contains nine terminal methyl protons (A), five glycerol protons (four G and one H), and 12 carbonyl-adjacent protons (six E and six C). Double bonds add olefinic (I) and allylic (D) protons, and each methylene-interrupted double bond adds diallylic (F) protons. The remaining methylene protons (B) scale with chain length.

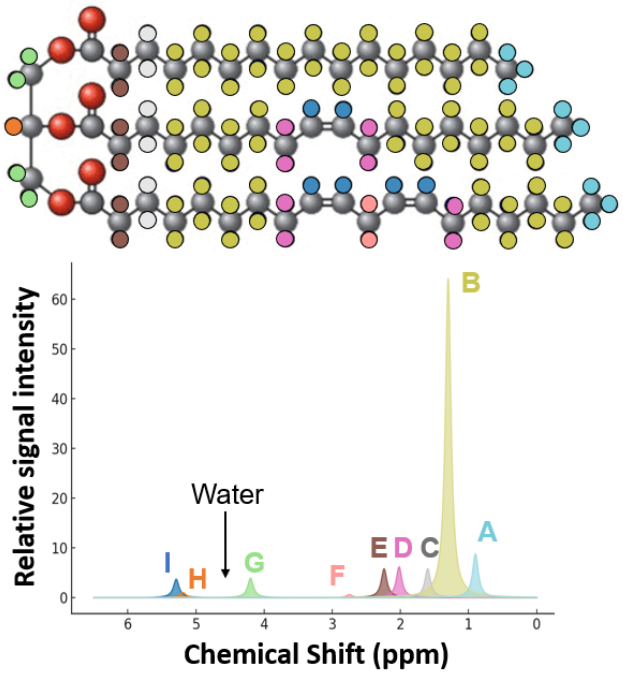

Peak	Type	δ[ppm]	Relative amplitude
A	methyl	0.9	9
B	methylene	1.3	$[cl - 4 \times 6] - (ndb \times 8) - (nmidb \times 2)$
C	β-carboxyl	1.6	6
D	α-olefinic	2.02	$(ndb - nmidb) \times 4$
E	α-carboxyl	2.24	6
F	diacyl	2.75	$nmidb \times 2$
G	glycerol	4.2	4
Water	-	4.7	-
H	glycerol	5.19	1
I	olefinic	5.29	$ndb \times 2$

Figure 7 - Triglyceride structure and corresponding fat spectrum with nine distinct resonance peaks (A–I). Each peak represents a chemically distinct proton group. Their relative amplitudes vary with fatty acid composition, characterized by the number of double bonds (ndb), methylene-interrupted double bonds (nmidb), and chain length (cl). Gray = carbon atoms; red = oxygen atoms.

Traditional PDFF models use a fixed fat spectrum, assuming constant *ndb*, *nmidb*, and *cl* values[21]. In contrast, composition-dependent fat models allow these parameters to vary, enabling the relative amplitudes of each peak to reflect the actual fatty acid profile. These flexible models improve the accuracy of fat quantification and support noninvasive estimation of fatty acid composition.

Fatty acid composition (FAC) mapping

FAC mapping builds on these models to estimate triglyceride composition from MRI data. This goes beyond measuring fat quantity, providing insight into the types of fatty acids stored in tissues. The FAC has growing relevance in metabolic disease, with polyunsaturated fatty acid

(PUFA)-, monounsaturated fatty acid (MUFA)-, and saturated fatty acid (SFA)-rich triglycerides having different implications in conditions such as obesity, insulin resistance, and nonalcoholic fatty liver disease. FAC also reflects dietary intake and lipid metabolism.

Different fatty acids have distinct spectral signatures: saturated fats are rich in methylene protons (~1.3 ppm), monounsaturated fats contribute olefinic peaks (~5.3 ppm), and polyunsaturated fats produce diacyl peaks (~2.75 ppm). These peaks can be detected using chemical-shift-encoded MRI, which acquires multiple gradient echo images at different echo times to capture the phase evolution of fat and water signals. Compared to MR spectroscopy, this enables spatially resolved FAC maps across tissues.

The general MR signal model from water (*W*) and fat (*F*) substances incorporates multiple fat peaks (with relative amplitudes ρ_m and frequencies f_m relative to water), B_0 off-resonance (ψ), and transverse relaxation ($T_2^* = 1/R_2^*$), as follows:

$$S(t) = \left(W + F \sum_{m=A,B,C\ldots}^{I} \rho_m \alpha_m(t) \right) e^{(i2\pi\psi - R_2^*)t} \tag{1.12}$$

A more detailed discussion of this topic appears in Chapter 2. The outputs of FAC MRI include estimates of *ndb* and *nmidb* per triglyceride, which are then used to compute the relative proportions of SFA, MUFA, and PUFA within each image voxel (**Figure 8**).

These techniques have been applied to liver[24,25], bone marrow[26,27], and adipose tissue[28,29] (subcutaneous and visceral) in both preclinical[30,31] and clinical settings[26,28]. Their use in spatially mapping fat composition has opened new opportunities for studying metabolic disease and tissue-specific lipid biology.

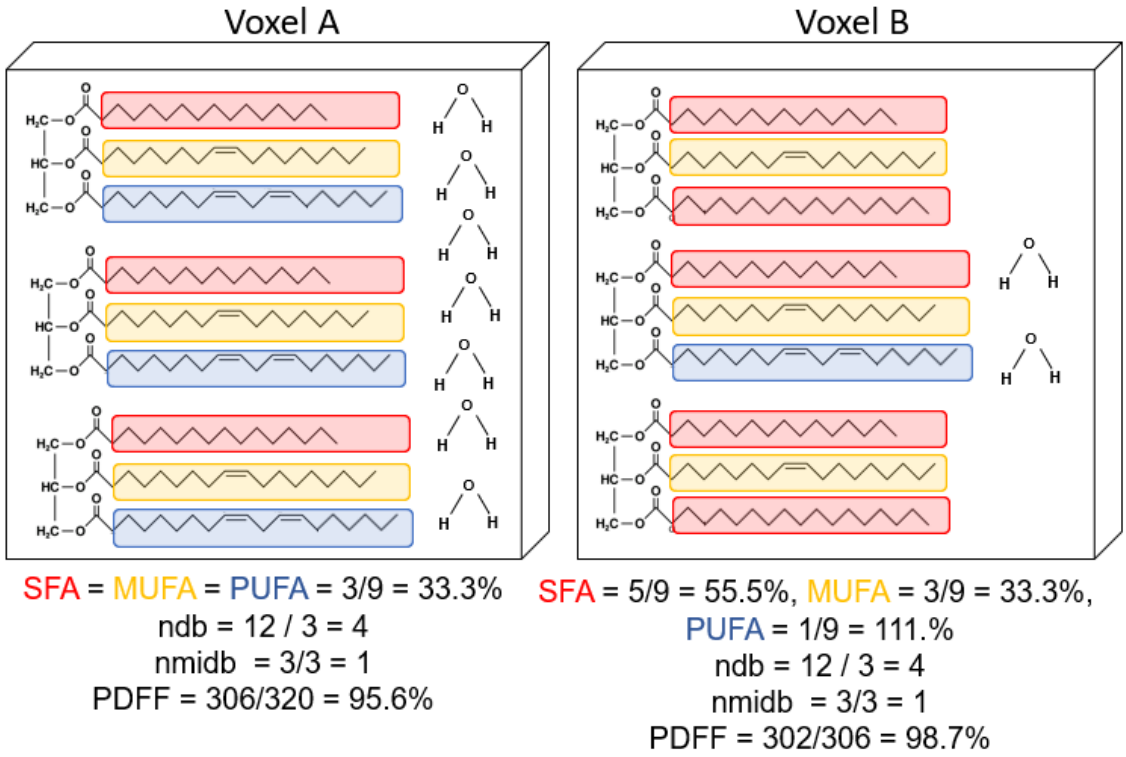

Figure 8 – Simplified illustration of fatty acid composition (FAC) MRI metrics in adipose tissue. Each voxel contains a mixture of triglycerides with varying saturated (SFA), monounsaturated (MUFA), and polyunsaturated (PUFA) fatty acid content. SFA, MUFA, and PUFA are reported as fractions of fatty acids, while the number of double bonds (ndb) and methylene-interrupted double bonds (nmidb) are calculated per triglyceride. Proton density fat fraction (PDFF) reflects the proportion of fat protons relative to total proton signal.

1.2 Heart failure with preserved ejection fraction (HFpEF)

Heart failure (HF) affects approximately six million people in the United States[32], with heart failure with preserved ejection fraction (HFpEF) accounting for about 50% of all HF cases. HFpEF is defined by an ejection fraction (EF) greater than 50% and is associated with a poor prognosis, with a five-year survival rate of only 35%[33]. The prevalence of HFpEF has increased over recent decades. Data from the Framingham Heart Study show that the ratio of HFpEF to heart failure with reduced ejection fraction (HFrEF) shifted from 41:59 between 1985 and 1994 to 56:44

between 2005 and 2014[33]. This increase is partly due to improved recognition and diagnostic criteria but also reflects broader epidemiologic trends, including the rising prevalence of metabolic syndrome.

Clinically, HFpEF most commonly presents with dyspnea on exertion and signs of volume overload, including peripheral edema, jugular venous distension, and ascites. A third heart sound (S3 gallop) may also be present[34]. Unlike HFrEF, where systolic dysfunction is prominent, HFpEF is characterized by diastolic dysfunction, where the heart muscle becomes stiff and fails to relax normally.

HFpEF is increasingly recognized as a heterogeneous, multiorgan syndrome driven by systemic comorbidities such as obesity, diabetes, and hypertension[34]. Cardiac abnormalities in HFpEF include left ventricular (LV) hypertrophy or remodeling, impaired LV relaxation, myocardial microvascular dysfunction, fibrosis, elevated LV filling pressures, left atrial enlargement, and increased epicardial adipose tissue (EAT). While uncontrolled hypertension has long been considered a key driver of myocardial hypertrophy and fibrosis in HFpEF[35], studies show that fewer than 50% of HFpEF patients meet criteria for LV hypertrophy, and myocardial fibrosis is typically only mildly increased[34].

An emerging pathophysiological paradigm suggests that systemic inflammation, particularly in the context of metabolic comorbidities, plays a central role in HFpEF progression. Chronic low-grade inflammation, oxidative stress, and myocardial microvascular dysfunction contribute to increased myocardial stiffness, fibrosis, and reduced perfusion reserve[36]. Given this, the interplay between inflammation and microvascular dysfunction has become an area of increasing interest in HFpEF research.

1.2.1 Coronary microvascular disease (CMD) and its role in HFpEF

Coronary microvascular disease (CMD) refers to dysfunction of the coronary microvasculature, which includes pre-arterioles (100–400 μm) and arterioles (<100 μm) that regulate myocardial blood flow[37]. Because myocardial oxygen extraction is near maximal at rest, coronary blood flow must increase to meet higher metabolic demands. Impaired vasodilation or microvascular structural abnormalities can lead to myocardial ischemia[37]. CMD encompasses both structural and functional impairments. Structural abnormalities include vascular remodeling, rarefaction, luminal obstruction, and perivascular fibrosis, while functional impairments involve endothelial and vascular smooth muscle dysfunction. Specifically, endothelial dysfunction may stem from reduced nitric oxide (NO) production, whereas vascular smooth muscle dysfunction results from impaired NO-mediated vasodilation[38]. CMD presents as two overlapping endotypes: functional CMD, characterized by normal minimal microvascular resistance and increased resting coronary blood flow, often linked to neuronal nitric oxide synthase (nNOS) dysfunction; and structural CMD, which is defined by heightened minimal microvascular resistance and impaired stress-induced coronary blood flow, associated with endothelial nitric oxide synthase (eNOS) dysfunction[38].

In clinical practice, both endotypes often coexist. CMD is associated with cardiovascular comorbidities, including diabetes, metabolic syndrome, dyslipidemia, hypertension, obesity, and smoking[38]. It presents with exertional or rest angina, dyspnea, and, in some cases, HF. However, because conventional coronary angiography cannot visualize the microcirculation, CMD diagnosis relies on measuring coronary microvascular function via direct myocardial blood flow changes at rest and during stress. Noninvasive imaging modalities such as positron emission tomography (PET), cardiac magnetic resonance (CMR), and Doppler echocardiography assess coronary flow

reserve (CFR) or myocardial perfusion reserve (MPR), defined as the ratio of hyperemic to resting myocardial blood flow[39].

CMD plays a major role in HFpEF pathophysiology, such that a CMD-HFpEF endotype has been described[40]. Patients with CMD and diastolic dysfunction have a more than five-fold increased risk of HFpEF hospitalization[41]. The PROMIS-HFpEF trial found that approximately 75% of HFpEF patients had CMD[1]. It has also been shown that the presence of CMD is associated with greater disease severity and worse clinical outcomes[1,42]. Emerging evidence suggests that microvascular endothelial dysfunction, reduced NO bioavailability, and inflammatory cytokine signaling drive microvascular rarefaction and myocardial fibrosis in HFpEF[43,44]. It is thought that cardiovascular risk factors, such as obesity and diabetes, induce systemic inflammation, leading to endothelial dysfunction via eNOS uncoupling and NO depletion. Impaired NO-cGMP-PKG signaling disrupts ventricular relaxation and contributes to subendocardial ischemia, which in turn promotes HFpEF development[40].

1.2.2 Inducible nitric oxide synthase (NOS2) in CMD and HFpEF

Inducible nitric oxide synthase (NOS2, formerly iNOS) is an enzyme responsible for producing NO in response to inflammatory stimuli[45,46]. While moderate levels of NO produced by eNOS and nNOS maintain normal biological function including cardiac contractility and vasodilation, in healthy conditions, NOS2 expression is minimal[47,48]. NOS2 production increases under inflammatory conditions and leads to 100-1,000 times more NO production than other NOS isoforms and contributes to tissue damage[49]. Dysregulated NOS2 activity has been implicated in several chronic diseases, including diabetes, atherosclerosis, and HFpEF[45,48–51].

NOS2 upregulation has been observed in human HFpEF hearts and in preclinical models. In a “two-hit” mouse model of HFpEF, in which metabolic stress was induced by a high-fat diet

(HFD) and mechanical stress by L-NAME (a NOS inhibitor), Schiattarella et al. identified a central role for nitrosative stress in HFpEF progression[51]. Because L-NAME preferentially inhibits eNOS and nNOS over NOS2, it paradoxically induces NOS2 upregulation. Similarly, NOS2 is elevated in rodents exposed to HFD[52]. Consistent with this, Schiattarella et al. found that their HFpEF model triggered systemic inflammation alongside increased NOS2 levels in the myocardium, a finding mirrored in left ventricular samples from human HFpEF hearts. Inhibition of NOS2 via genetic deletion improved diastolic function and exercise tolerance, while short-term pharmacological inhibition with the NOS2 inhibitor L-NIL partially improved ventricular relaxation and exercise performance, although through a different mechanism. These findings underscore the role of NOS2 in HFpEF pathophysiology and suggest that the specific mechanisms by which NOS2 contributes to HFpEF remain largely unknown.

NOS2 also contributes to CMD and diastolic impairment in a high-fat, high-sucrose diet (HFHSD) mouse model[53]. NOS2 genetic deletion preserved coronary arteriolar and myocardial perfusion responses to adenosine, which are otherwise impaired by HFHSD-induced obesity, glucose intolerance, metabolic inflammation, and oxidative stress. Pharmacological inhibition partially restored myocardial perfusion and fully preserved the vascular perfusion response to adenosine. NOS2 deletion also improved longitudinal myocardial strain compared to HFHSD controls.

Despite the findings that metabolic inflammation drives production of NOS2, the specific cell type responsible for NOS2 production in HFpEF remains unidentified. Notably, NOS2 is known to be expressed in almost every cell type. Given the failure of NO-inducing therapies for HFpEF[54,55], targeting NOS2 and other proinflammatory mediators may offer a more promising therapeutic approach.

1.2.3 Obesity and inflammation in HFpEF

The increasing prevalence of HFpEF mirrors the global obesity epidemic, with projections indicating that nearly half of U.S. adults will have obesity (BMI ≥ 30 kg/m²) and one in four adults will have severe obesity (BMI ≥ 35 kg/m^2) by 2030[56]. Central obesity and metabolic syndrome are highly prevalent among patients with HFpEF and are now recognized as major drivers of its pathophysiology. This has led to the classification of a cardiometabolic HFpEF phenotype, which is the most common among HFpEF phenotypes and carries the worst prognosis[2,57]. Cardiometabolic HFpEF is characterized by low-grade, systemic inflammation, accompanied by dysregulation of inflammatory and immune responses, adipose tissue accumulation and dysfunction, microvascular impairment, and metabolic abnormalities, which together, directly affect myocardial structure and function[2,58] (**Figure 9**).

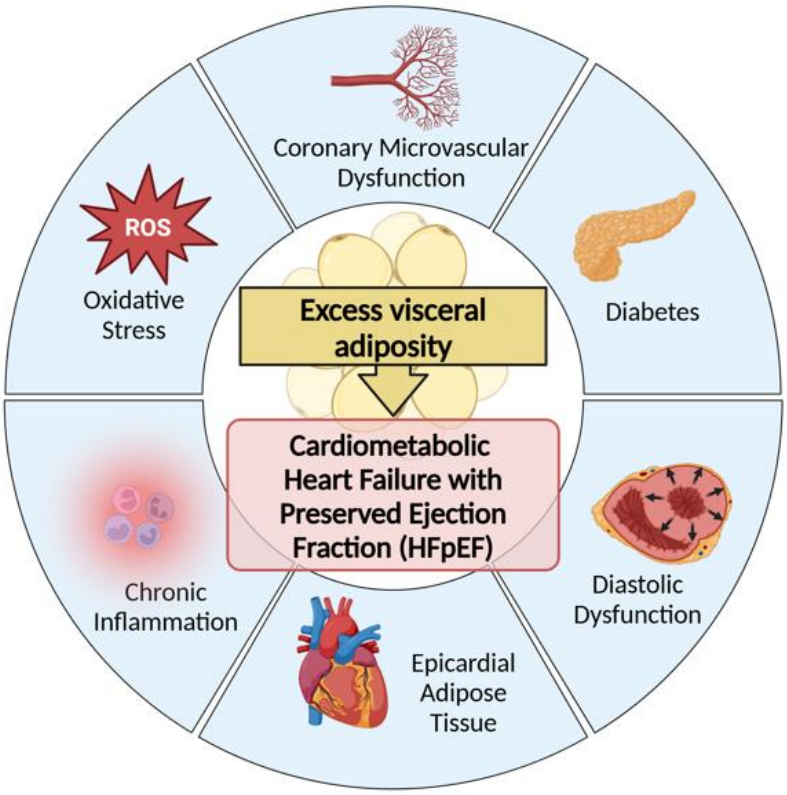

Figure 9 - Excess visceral adiposity in contributes to the development of cardiometabolic heart failure with preserved ejection fraction (HFpEF) through multiple related mechanisms including oxidative stress, chronic inflammation, coronary microvascular dysfunction, diabetes, diastolic dysfunction, and epicardial adipose tissue dysfunction.

Adipose tissue distribution

A major driver of cardiometabolic HFpEF is the accumulation of visceral adipose tissue (VAT). Although obesity is a well-established risk factor for HFpEF, BMI alone is an imprecise measure of obesity-related cardiovascular risk. BMI does not account for differences in fat distribution, which is critical since VAT is far more metabolically active and inflammatory than subcutaneous adipose tissue (SAT)[59]. VAT expansion is more strongly associated with an adverse metabolic risk profile. Thus, measurement of VAT may provide a more complete understanding of cardiovascular

risk than total adipose tissue mass[60]. The PARAGON-HF trial highlighted the limitations of BMI and the significance of VAT in HFpEF, showing that while only 49% of HFpEF patients in the trial were classified as obese by BMI, 96% had central (abdominal/visceral) adiposity when assessed by waist-to-hip ratio (WHtR)[61]. This suggests that VAT-driven metabolic dysfunction is intrinsic to HFpEF, even in individuals who do not meet traditional BMI criteria for obesity. Unlike BMI, WHtR is a more accurate marker of obesity-related inflammation and cardiometabolic risk because it better reflects VAT accumulation.

Adipose tissue as an endocrine and inflammatory organ

In addition to adipose tissue distribution, adipose tissue quality plays a role in the development of cardiometabolic HFpEF. Adipose tissue is more than just a fat depot—it is a highly active endocrine organ that regulates systemic metabolism and inflammation. In the context of obesity, the VAT is a prominent site of adipose tissue dysfunction and inflammation. VAT dysfunction in obesity is characterized by adipocyte hypertrophy, hypoxia, oxidative stress, production of proinflammatory cytokines, and subsequent infiltration of immune cells, especially macrophages[62]. Infiltrating macrophages may be recruited in response to death of hypertrophied adipocytes and form "crown-like structures" surrounding the adipocytes[62,63]. Furthermore, macrophages undergo a phenotypic shift in response to inflammatory signals from an anti-inflammatory M2 phenotype to a pro-inflammatory M1 phenotype, leading to increased secretion of proinflammatory cytokines and a decrease in anti-inflammatory cytokines[64]. It has been shown that macrophage infiltration is associated with tissue specific-changes in lipid metabolism and cytokine production[65]. It has been proposed that the action of inflammatory molecules from adipose tissue macrophages may represent the link between adipose tissue and the cardiometabolic complications of obesity[62].

1.2.4 Epicardial adipose tissue (EAT): function and dysfunction

EAT has gained increasing attention due to its unique anatomical and functional properties, distinguishing it from other visceral fat depots. Unlike other adipose tissues, EAT sits directly atop the myocardium without a physical barrier or fascial layer, allowing unobstructed crosstalk between EAT and the heart via paracrine and vasocrine signaling[3]. While EAT plays a protective metabolic and structural role in healthy conditions, it undergoes pathological transformation in disease states such as obesity, metabolic syndrome, and HFpEF, where it becomes pro-inflammatory, pro-fibrotic, and contributes to myocardial dysfunction[66]. This has positioned EAT as a key transducer of systemic inflammation in cardiovascular diseases, including atherosclerosis, atrial fibrillation, and HFpEF[67] (**Figure 10**).

EAT in health

Under healthy conditions, EAT serves as an energy reservoir, supplying the heart with fatty acids while also acting as a metabolic buffer, preventing excess free fatty acids from accumulating in the coronary circulation. Healthy EAT has brown and beige fat-like properties, with small adipocytes and increased thermogenic capacity, acting as a source of heat and protecting the heart during ischemic or hypoxic stress[3,68]. Studies suggest that EAT accounts for approximately 20% of total ventricular weight in individuals who died of non-cardiovascular causes, with men generally having greater EAT volume than women[66]. EAT may also serve as a mechanical cushion, protecting the coronary arteries during cardiac contraction[66].

Pathological transformation of EAT

In pathological states such as obesity and metabolic syndrome, EAT undergoes maladaptive remodeling, shifting from a metabolically active, brown-like fat depot to a white adipose-like phenotype characterized by larger, unilocular adipocytes primed for fat storage. While this

transition occurs naturally with aging, metabolic stress further exacerbates these changes, leading to increased inflammation, fibrosis, and myocardial dysfunction[67].

One contributor to this transformation may be adipose tissue hypoxia. As EAT expands, oxygen delivery becomes insufficient, leading to chronic hypoxic stress. Despite this growth, angiogenesis remains impaired, and hypertrophied adipocytes can exceed the normal oxygen diffusion limit (100–200 μm)[69,70]. This state triggers the release of pro-inflammatory cytokines from adipocytes and the recruitment of immune cells, perpetuating local and systemic inflammation[66].

The FAC of EAT has also been proposed as a mediator of its inflammatory properties[71]. SFAs activate toll-like receptor 4 (TLR4), inducing NF-κB signaling and increasing the production of pro-inflammatory cytokines such as tumor necrosis factor-alpha (TNF-α) and interleukin-6 (IL-6)[72,73] (**Figure 10**). These cytokines promote oxidative stress, microvascular dysfunction, and myocardial remodeling[74], contributing to diastolic dysfunction and HFpEF progression. In contrast, MUFAs and PUFAs exhibit anti-inflammatory properties by suppressing NF-κB activation and reducing cytokine production[75]. Compared to SAT, EAT is disproportionately enriched in SFAs, while MUFAs and PUFAs are less abundant, further promoting a pro-inflammatory and pro-fibrotic environment[76]. While diet influences adipose tissue FAC, depot-specific factors such as differential fatty acid mobilization, deposition rates, and endogenous synthesis also contribute to metabolic differences between EAT and other adipose depots[76].

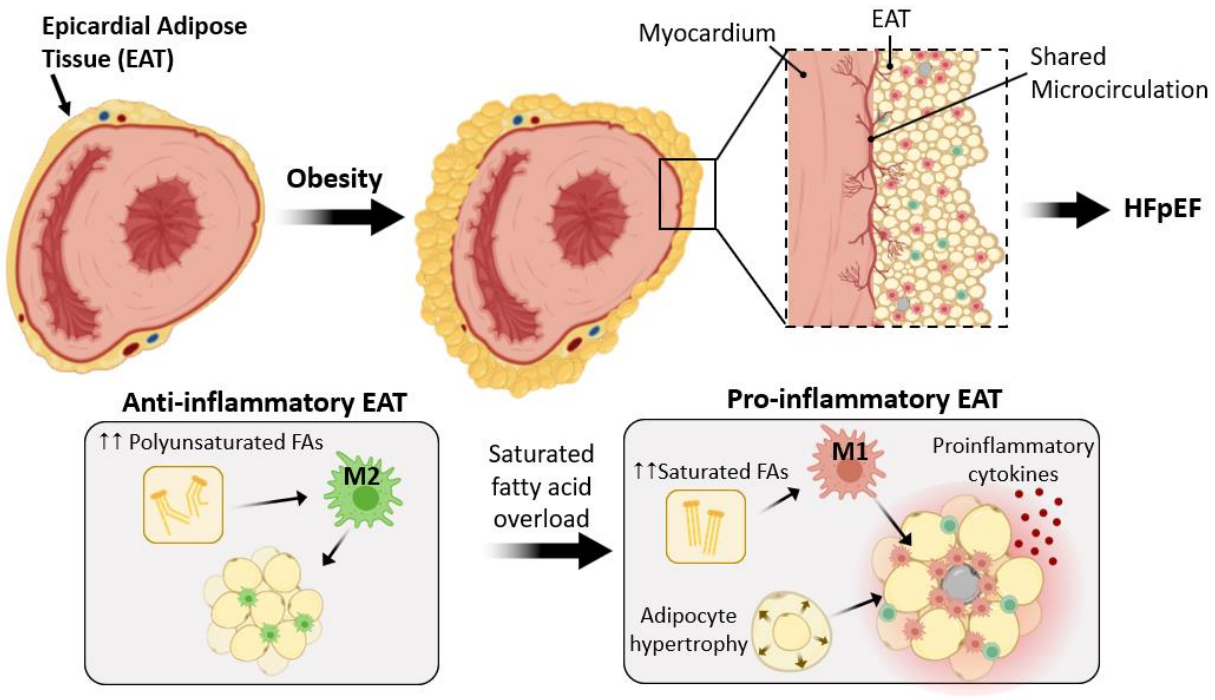

Figure 10 - Epicardial adipose tissue (EAT) contributes to heart failure with preserved ejection fraction (HFpEF) through its direct proximity to the myocardium and shared microcirculation, promoting inflammation through adipocyte hypertrophy, saturated fatty acid (FA) overload, and immune cell (macrophage) polarization and infiltration[77].

Role of EAT in HFpEF

Excess EAT accumulation is strongly associated with HFpEF, contributing to myocardial fibrosis, ventricular hypertrophy, and elevated cardiac filling pressures, all hallmark features of the disease[78]. Studies have demonstrated that patients with HFpEF have increased EAT thickness and volume, even when adjusting for BMI[79,80]. Higher baseline EAT is predictive of new-onset HFpEF, suggesting a causal role in disease progression[81]. Additionally, EAT volume is independently associated with worse clinical outcomes, including reduced exercise capacity and increased risk of hospitalization, regardless of BMI or New York Heart Association class[82,83]. EAT

also plays a role in CMD which is closely linked with HFpEF, with elevated EAT volume strongly associated with the presence of CMD[84].

The role of EAT in HFpEF pathophysiology is likely multifactorial. Accumulation of EAT physically restricts myocardial expansion, impairing diastolic function[66]. Infiltration of EAT-derived fatty acids and inflammatory mediators into the myocardium may induce cellular toxicity and metabolic dysregulation, contributing to worsening cardiac function[66]. Indeed, patients with HFpEF exhibit higher levels of intramyocardial fat, which correlate with the severity of diastolic dysfunction[85]. Additionally, dysfunctional EAT secretes pro-inflammatory cytokines and adipokines, exacerbating local inflammation, which is central to obesity-related HFpEF[86].

1.2.5 Assessing EAT

EAT can be evaluated using several noninvasive imaging techniques, including echocardiography, CT, MRI, and PET. Each modality provides distinct information on EAT volume, distribution, composition, and potential inflammatory activity.

^{18}F-FDG-PET, can detect metabolic activity within EAT, which may indicate inflammation[87]. However, its use is limited due to cost and availability. Echocardiography is widely available and identifies EAT as a hypoechoic space between the myocardium and the visceral pericardium. It allows for thickness measurement but is limited by inter- and intra-operator variability and does not provide volumetric data[67].

CT offers higher spatial resolution and enables volumetric assessment of EAT, which has been associated with clinical outcomes[88,89]. Additionally, CT-derived fat attenuation index (FAI), expressed in Hounsfield units, provides information on fat composition. FAI has been proposed as a biomarker of EAT and perivascular inflammation, with higher values linked to coronary artery disease, atrial fibrillation, and microvascular dysfunction[90,91].

MRI provides volumetric and thickness measurements while also characterizing tissue properties. It can assess relaxation properties that may reflect inflammation[92] and measure EAT PDFF and fat composition, including its fatty acid profile[28,31]. These capabilities may help identify triggers of inflammation and changes in adipose tissue morphology. These noninvasive imaging modalities provide insights into EAT structure and function. Ongoing research continues to refine their applications in assessing cardiovascular risk.

1.3 Sodium-glucose cotransporter-2 (SGLT2) inhibitors

In healthy individuals, nearly all glucose filtered at the glomerulus is reabsorbed into the bloodstream, thus no glucose is detected in the urine. However, when a threshold of glucose in the plasma is exceeded, urinary glucose excretion increases[93]. This process of glucose transport across epithelial cells is mediated by sodium-glucose transporters (SGLTs). SGLT2, located primarily in the proximal tubule and at much lower concentrations in the brain, liver, thyroid, and skeletal muscle, is responsible for >90% of the glucose reabsorption, while SGLT1 is more widely distributed and responsible for remaining glucose reabsorption[94].

SGLT2 inhibitors lower blood glucose levels by blocking renal glucose reabsorption, leading to increased urinary glucose excretion (**Figure 11**). Despite near-complete SGLT2 inhibition, only 50–60% of filtered glucose is excreted due to compensatory SGLT1 activity in more distal tubule segments[95]. Several selective SGLT2 inhibitors have been developed and approved for clinical use, including canagliflozin, dapagliflozin, empagliflozin, and ertugliflozin. These agents effectively reduce hyperglycemia in type 2 diabetes mellitus and provide additional benefits such as weight loss and improved cardiovascular outcomes[93].

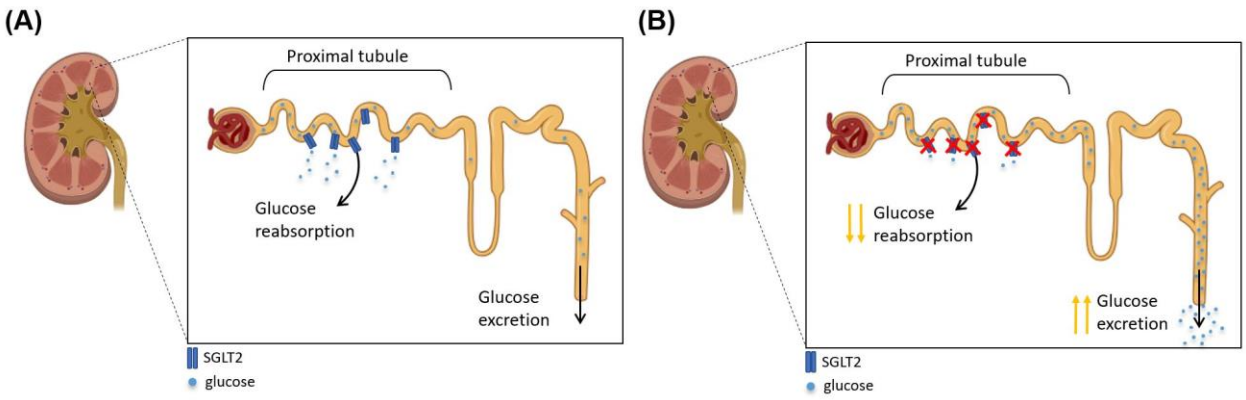

Figure 11 - Mechanism of action of SGLT2 inhibitors. (A) Under normal conditions, SGLT2 transporters in the proximal tubule reabsorb the majority of filtered glucose back into the bloodstream, preventing glucose loss in urine. (B) SGLT2 inhibitors block glucose reabsorption in the proximal tubule, leading to increased urinary glucose excretion and reduced blood glucose levels.

1.3.1 Therapeutic efficacy in HFpEF

Treating HFpEF has been challenging due to its complex pathophysiology and diverse phenotypes. SGLT2 inhibitors were initially found to provide unexpected cardiovascular benefits in patients with HFpEF and diabetes, leading to further investigation in patients with HFpEF regardless of diabetes status[96]. Recent Phase III trials, DELIVER[97] and EMPEROR-Preserved[98], evaluated the effects of 10 mg dapagliflozin or empagliflozin daily in patients with HFpEF and demonstrated significant clinical benefits. These studies, along with others, have shown that SGLT2 inhibitors reduce the composite outcome of heart failure hospitalizations and cardiovascular death across the full spectrum of ejection fraction, including in patients with worsening or acute heart failure, and in both diabetic and non-diabetic populations. The reduction in heart failure hospitalizations was the primary driver of these benefits.

1.3.2 Mechanisms of cardiovascular benefit

The mechanisms underlying the beneficial effects of SGLT2 inhibitors in HFpEF are complex and likely multifactorial. While improvements in traditional HF risk factors such as diabetes, hypertension, and chronic kidney disease may contribute, the rapid onset of clinical benefit and cardiac remodeling observed with SGLT2 inhibitors suggests additional mechanisms are involved[99]. Translational research continues to explore how these agents exert their cardioprotective effects. Below are a few proposed mechanisms through which SGLT2 inhibitors exert their cardiovascular benefit.

Blood pressure, blood sugar, and diuresis

SGLT2 inhibitors improve several traditional risk factors for HFpEF, including lowering blood pressure and blood sugar, and improving renal function, but these effects alone do not fully explain their cardiovascular benefits[99,100]. While SGLT2 inhibitors have been shown to reduce blood pressure, in the EMPEROR-Preserved trial, empagliflozin had similar benefits in patients regardless of baseline systolic blood pressure[98]. With regard to blood sugar, the magnitude of the blood glucose-lowering effect is modest, other agents that exert greater antihyperglycemic effects have not shown the same beneficial effects in HF[101]. Furthermore, these benefits are seen in patients both with and without diabetes, suggesting that the blood glucose lowering effects are not primarily responsible for the cardiovascular benefits[98,102]. Similarly, while SGLT2 inhibitors slow the decline of kidney function, these mechanisms do not entirely account for their efficacy, as benefits are seen across all levels of kidney function[99]. Natriuresis and diuresis may contribute, particularly in acute HF, where empagliflozin has been shown to increase urine output and fluid loss and have a rapid time-course benefit. However, diuresis is unlikely to be the primary mechanism in chronic HF, as studies have not demonstrated greater efficacy in volume-overloaded

patients[103]. Instead, sustained weight loss associated with SGLT2 inhibitors is thought to result from glycosuria and reductions in visceral fat, potentially playing a role in their long-term benefits[103,104].

Metabolism, autophagy, and cardiac energetics

SGLT2 inhibitors may exert cardioprotective effects by inducing metabolic adaptations that mimic fasting and hypoxia[99,102,105]. By promoting glycosuria, they create a perceived nutrient deficit, triggering increased ketone production, which serves as an alternative energy source for the failing heart[105]. Since fatty acid oxidation is impaired in heart failure, ketones may improve cardiac efficiency and function. However, the benefit is likely not attributed to ketogenesis, since SGLT2 inhibition does not predicably increase ketone body utilization in the myocardium, and evidence that these drugs increase ketone production is primarily seen in patients with diabetes[106]. Yet, benefits of SGLT2 inhibitors are observed in patients with and without diabetes[97]. Additionally, SGLT2 inhibitors enhance autophagy, a cellular process that recycles damaged organelles/proteins and reduces inflammasome activation, which is typically impaired in heart failure[106]. This may help reduce oxidative stress and inflammation while supporting overall cellular function[105].

Beyond metabolism, SGLT2 inhibitors also influence iron regulation and erythropoiesis, which may contribute to their cardiovascular benefits[107]. Iron deficiency is common in heart failure and is associated with poor outcomes[108]. These agents appear to improve iron mobilization and utilization, potentially by reducing inflammatory mediators and altering iron storage proteins[99]. They also consistently increase erythropoietin levels within weeks of treatment, which may enhance red blood cell production and improve oxygen delivery[99]. However, while SGLT2 inhibitors enhance red blood cell mass, increased erythropoiesis does not favorably influence HF outcomes[106,109]. While further research is needed to fully understand these mechanisms, these

metabolic and cellular effects likely contribute to the broader benefits of SGLT2 inhibitors in heart failure.

Adipose Tissue

SGLT2 inhibitors may exert cardioprotective effects, in part, by modulating EAT. Meta-analyses have shown that these agents reduce EAT volume without significantly affecting overall body mass index[104]. This reduction is thought to mitigate myocardial inflammation and fibrosis, potentially through altered adipokine signaling. SGLT2 inhibitors increase adiponectin, an insulin-sensitizing and anti-inflammatory hormone, while decreasing leptin, a hormone linked to cardiac fibrosis and microvascular dysfunction[110].

Beyond reducing EAT volume, SGLT2 inhibitors appear to directly influence adipose tissue function. Studies in EAT-derived preadipocytes have shown that SGLT2 is expressed in these cells, and empagliflozin treatment affects lipid accumulation and suppresses pro-inflammatory cytokines such as IL-1α, IL-1β, and IL-6, but only when administered before differentiation into mature adipocytes[111]. This suggests a role in adipose tissue remodeling rather than just volume reduction. In the same study, cardiomyocytes co-cultured with empagliflozin-treated adipocytes exhibited lower oxidative stress and reduced natriuretic peptide expression, though the clinical significance of these findings remains uncertain. Additionally, SGLT2 inhibitors have been associated with a shift in adipose tissue macrophage polarization, reducing pro-inflammatory M1-like macrophages and increasing anti-inflammatory M2-like macrophages, further supporting their role in promoting a healthier adipose tissue environment[112].

Inflammation and oxidative stress

SGLT2 inhibitors reduce oxidative stress and inflammation through multiple mechanisms. They lower circulating pro-inflammatory markers (C-reactive protein, TNF-α, IL-6) while also

decreasing myocardial oxidative stress and reactive oxygen species[113]. These effects may be driven by reductions in uric acid, epicardial fat, and adipokine alterations. Additionally, SGLT2 inhibitors inhibit activation of the NLRP3 inflammasome, a protein complex in macrophages that plays an important role in chronic inflammation in heart failure[114,115]. Since oxidative stress is a strong modulator of the inflammatory response through ROS-induced expressions of NLRP3 inflammasome and NF-kB, these effects may be closely related. This inhibition reduces macrophage infiltration and pro-inflammatory cytokine release, with potential systemic benefits[114].

Diastolic function and cardiac remodeling

SGLT1, but not SGLT2 is expressed in the heart suggesting that the potential effect of SGLT2 inhibitors on LV structure and function is likely to be indirectly mediated by hemodynamic and systemic metabolic improvements[93,116]. SGLT2 inhibitors have been shown to improve diastolic function and cardiac remodeling, likely through multiple mechanisms. Clinical studies have demonstrated improvements in LV diastolic function and reductions in LV hypertrophy after just a few months of SGLT2 inhibitor treatment[117,118]. Diastolic dysfunction in HFpEF has several components, including myofilament stiffness and extracellular matrix-related stiffness/myocardial fibrosis[119]. SGLT2 inhibitors may reduce diastolic dysfunction by improving NO bioavailability, modulating titin phosphorylation – a myofilament in cardiac muscle with a large role in diastolic function[120] – and decreasing myocardial stiffness[119]. Beyond direct cardiomyocyte effects, SGLT2 inhibitors have been shown to reduce inflammation which can have beneficial effects on myocardial fibrosis. Specifically, SGLT2 inhibitors have been shown to reduce macrophage infiltration, regulate macrophage polarization, and inhibit cardiac fibroblast differentiation, thus attenuating fibrosis and adverse cardiac remodeling[99].

1.4 Preclinical methods to investigate HFpEF

The heterogeneity of HFpEF presents challenges in developing mouse models that accurately replicate its complex pathophysiology. HFpEF is characterized by typical HF symptoms alongside a combination of cardiac features—such as LV hypertrophy, diastolic dysfunction, fibrosis, atrial enlargement, and microvascular dysfunction—and extra-cardiac comorbidities, including hypertension, obesity, and type 2 diabetes mellitus. Given the rising prevalence, poor prognosis, and lack of effective therapies, preclinical models are essential for studying HFpEF mechanisms and potential treatments.

However, most preclinical models capture only specific aspects of the syndrome, and even multifactorial models fail to fully replicate its heterogeneity[121,122]. Ideally, an HFpEF model should encompass key clinical features, including elevated natriuretic peptide levels, impaired exercise capacity, lung congestion, preserved systolic LV function, concentric hypertrophy, diastolic dysfunction, and microvascular dysfunction along with relevant comorbidities[121]. While no single model fully represents HFpEF, various approaches have been developed to study different aspects of the disease.

1.4.1 Overview of HFpEF mouse models

Angiotensin-II infusion models

Chronic activation of the angiotensin II type 1 receptor through osmotic mini-pump infusion induces HF characterized by cardiac hypertrophy and remodeling[123]. In C57BL/6 mice, ANGII infusion leads to lung congestion, exercise intolerance, concentric remodeling with fibrosis, and elevated natriuretic peptides[121,124]. While ANGII-induced hypertension models share many cardiac features with human HFpEF, they do not account for aging or obesity, limiting their relevance as HFpEF models. As a result, these are considered low-probability HFpEF models[121].

Genetic models

Genetically modified mouse models may also serve as preclinical HFpEF models, particularly in the context of cardiometabolic disease. The leptin receptor-deficient (*db/db*) model is widely used to study type 2 diabetes[125], as young *db/db* mice develop obesity and hyperglycemia without hypertension[126]. However, disease onset occurs at an early age, which does not align with the gradual disease progression seen in humans. With age, *db/db* mice develop diastolic dysfunction, atrial enlargement, concentric hypertrophy, and fibrosis, making them a potential HFpEF model[121,127].

Similarly, leptin-deficient (*ob/ob*) mice develop obesity and diabetes within four weeks[128]. These mice exhibit concentric hypertrophy and diastolic dysfunction with preserved EF but do not show exercise impairment, congestion, or natriuretic peptide elevation. Because leptin deficiency is rare in human HFpEF, *ob/ob* mice are likely do not accurately depict the clinical pathophysiology of HFpEF[121].

Aged mice (24-30 months)

Aging is a major contributor to HFpEF pathophysiology, and aged mice naturally develop key disease features even without dietary or pharmacologic intervention[129]. By 24–30 months, mice exhibit diastolic dysfunction, concentric hypertrophy with fibrosis, reduced exercise capacity, lung congestion, and elevated natriuretic peptides[129,130]. However, they do not always develop common HFpEF comorbidities such as hypertension or diabetes. While aged mice closely model clinical HFpEF, they lack the full comorbidity burden seen in patients[121].

Diet-induced models

Since obesity is a major HFpEF comorbidity and is present in most HFpEF patients, diet-induced obesity models may provide a promising approach for studying HFpEF pathophysiology. High-fat

diets (HFD, >60% kcal from fat) and Western/high-fat high-sucrose diets (HFHSD, 36–40% kcal from fat, 36–40% kcal from sucrose) induce obesity and glucose intolerance, with phenotypes worsening over time[131]. These models develop concentric LV hypertrophy with preserved EF, moderate diastolic dysfunction, pulmonary hypertension, and increased cardiac fibrosis[132].

However, they generally lack pulmonary congestion and natriuretic peptide elevation[121]. Mice on these diets exhibit reduced exercise capacity, likely due to obesity rather than intrinsic skeletal muscle dysfunction[51]. Because these models better replicate HFpEF-related comorbidities than genetic or ANGII models, they may be more physiologically relevant. However, they still remain imperfect HFpEF models due to inconsistencies in natriuretic peptide elevation and lung congestion[121].

Multifactorial models

Multifactorial models incorporate multiple stressors to better replicate human HFpEF. The deoxycorticosterone acetate salt-sensitive model, which combines deoxycorticosterone acetate administration, high salt intake, and uninephrectomy, and the uninephrectomy with aldosterone infusion model have been evaluated as possible as HFpEF models, yet they do not completely capture the complex pathophysiology of clinical HFpEF[121]. A more recent two-hit model, developed by Schiattarella et al., shows promise as it combines an HFD with L-NAME, a nitric oxide synthase inhibitor, to induce HFpEF[51]. Mice subjected to both stressors develop lung congestion, reduced exercise tolerance, and increased natriuretic peptides. Another multifactorial approach pairs an HFD with ANGII infusion, leading to hypertension, obesity, and diabetes in young male mice[133]. While these mice exhibit preserved LV function, diastolic dysfunction, concentric hypertrophy, fibrosis, and elevated natriuretic peptides, lung congestion is absent, and the effect on exercise capacity is unclear[121].

1.4.2 High-fat high-sucrose mouse model

The HFHSD mouse model (40% kcal from fat, 40% kcal from sucrose) used in this work induces cardiometabolic comorbidities, including glucose intolerance, obesity, and elevated mean arterial pressure after 18 weeks. Compared to standard diet (SD)-fed mice, HFHSD-fed mice gain approximately 50% more body weight (30 g SD vs. 45 g HFHSD) and exhibit persistently elevated blood glucose levels following a glucose tolerance challenge[53].

C57BL/6J mice fed an HFHSD for 18 weeks develop key cardiac features of HFpEF, including impaired systolic strain, diastolic dysfunction, and microvascular dysfunction[53]. Specifically, they exhibit reduced coronary microvascular dilation in response to adenosine, indicating endothelial-independent microvascular dysfunction. MRI strain imaging detects impaired systolic strain and diastolic strain rate despite preserved EF. Myocardial oxidative stress is also elevated in these mice.

In addition to cardiac dysfunction, HFHSD-fed mice develop metabolic alterations and chronic low-grade inflammation characteristic of cardiometabolic HFpEF[134]. They accumulate significant visceral adipose tissue, particularly epicardial adipose tissue, which has been implicated in HFpEF pathophysiology[31]. While this model does not fully recapitulate clinical HFpEF symptoms such as pulmonary congestion or elevated natriuretic peptides[121], it closely resembles the earlier stages of the cardiometabolic HFpEF phenotype, making it a valuable tool for studying the relationship between adiposity, coronary microvascular dysfunction, and diastolic dysfunction.

1.4.3 Preclinical cardiac MRI

CMR is a powerful noninvasive imaging modality used to assess cardiac anatomy, function, perfusion, and metabolism. In preclinical research, CMR enables high-resolution, serial in vivo characterization of cardiovascular structure and function in mouse models of disease, making it a

valuable tool for both basic and translational studies. However, the small size of the mouse heart (<1 cm) and its rapid rate (>600 bpm) pose significant technical challenges that require high spatial and temporal resolution[135].

Most preclinical CMR studies are performed on dedicated small-bore, high-field MRI scanners (4.7–9.4 T or higher), which provide the signal-to-noise ratio and gradient performance necessary for sub-millimeter resolution. High field strengths, however, come with trade-offs, including greater magnetic field inhomogeneity and gradient imperfections. Physiological gating is essential to reduce motion artifacts: ECG gating synchronizes acquisition to the cardiac cycle, while respiratory motion is managed through gating or retrospective correction, since breath-holding is not feasible in mice. Consistent anesthesia and careful physiological monitoring are also critical, as variations in agents like isoflurane can affect vascular tone and heart rate.

The imaging protocols used in this work include advanced methods to assess cardiac and vascular function—black-blood cine imaging, displacement encoding with stimulated echoes (DENSE), and arterial spin labeling (ASL)—along with newly developed techniques for characterizing adipose tissue properties.

Black-blood cine

Black blood cine imaging is a CMR technique that enables assessment of myocardial structure and function by suppressing signal from circulating blood. In the preclinical setting, it is commonly implemented using a double inversion recovery (DIR) preparation followed by a gated cine acquisition, typically with a FLASH (Fast Low Angle Shot) readout[136]. The DIR sequence begins with a non-selective inversion pulse that inverts all magnetization, followed immediately by a

slice-selective inversion pulse that re-inverts only stationary spins within the imaging slice. As inverted blood flows into the slice during the inversion time, it passes through the null point at the time of image acquisition, resulting in minimal signal, while stationary tissue recovers and appears bright. This blood suppression enhances contrast at the myocardial borders for improved definition of the endocardial border. Cine images are acquired across the cardiac cycle and through the short-axis stack of the left ventricle, enabling calculation of standard functional and morphological parameters, including ejection fraction (EF), end-diastolic (EDV) and end-systolic (ESV) volumes, end-diastolic (EDWT) and end-systolic (ESWT) wall thickness, and myocardial mass[135]. Accurate contouring of endocardial and epicardial borders, with attention to papillary muscles, is critical for deriving these measurements (**Figure 12**).

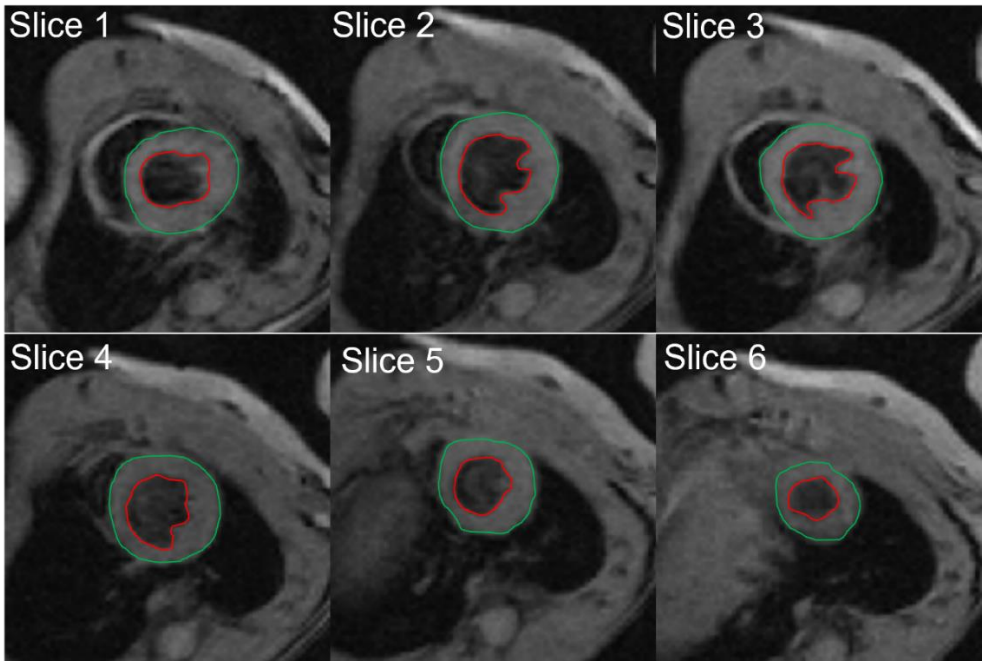

Figure 12 - Short-axis stack of black blood cine images from base to apex, with segmented endocardial (red) and epicardial (green) contours. Endocardial contours include papillary muscles for quantification of ejection fraction and

ventricular volumes. Additional contours excluding papillary muscles are used for calculating myocardial mass and wall thickness.

Myocardial Perfusion with Arterial spin labeling (ASL)

ASL is a noninvasive MRI technique that enables absolute quantification of myocardial blood flow (MBF) without contrast agents and has been applied to both cerebral[137] and cardiac perfusion imaging[138]. Cine-ASL combines ECG-gated cine gradient-echo imaging with steady-pulsed arterial labeling. Following each ECG trigger, a series of gradient echoes is acquired, with one replaced by a spatially selective inversion pulse to label coronary blood before it enters the myocardium. A control scan using a symmetrically placed slab accounts for magnetization transfer effects. **Figure 13A** shows the tag slab placed at the base of the heart to label the coronary arterial blood prior to its entry into the myocardium, and the control slab below the apex. Also included are representative images from a single cardiac phase include the control, tag, difference map, and quantified MBF map. The perfusion signal is derived from the difference between tag and control images and reflects MBF.

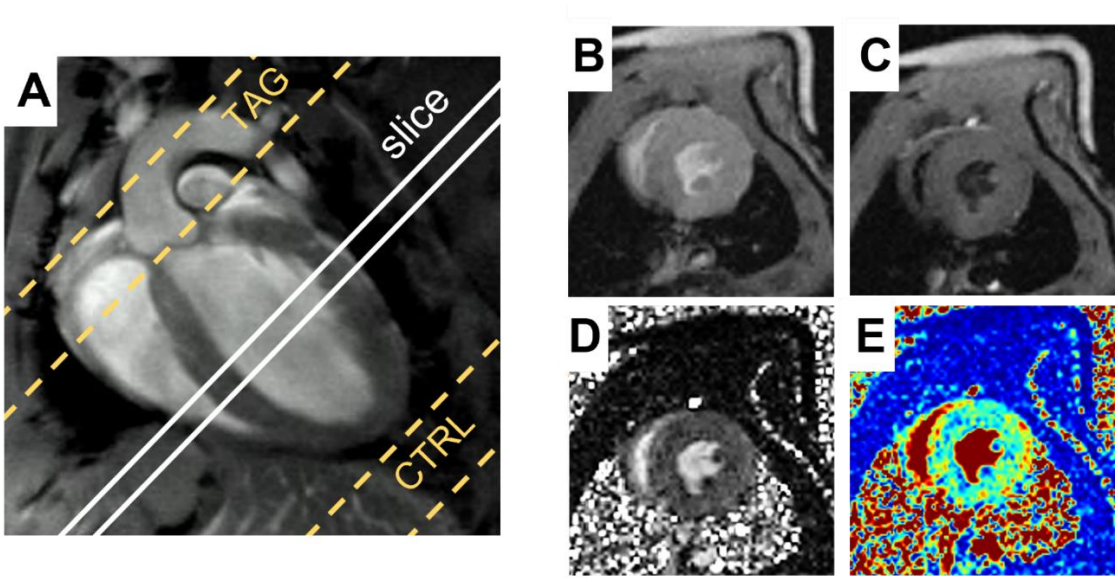

Figure 13 – Cine-ASL setup and resulting myocardial perfusion maps. (A) Long-axis view illustrating the positioning of the tagging (TAG) and control (CTRL) slabs relative to the mid-ventricular imaging slice. Short axis (B) control image, (C) tag image following arterial inversion, (D) difference image used to determine the myocardial blood flow (MBF), and (E) quantified MBF map.

By alternating tag and control scans across the cardiac cycle, cine-ASL generates high-resolution, temporally resolved perfusion maps. A typical protocol includes rest MBF acquisition, followed by a 10-minute intraperitoneal infusion of adenosine for stress imaging (**Figure 14**). Myocardial perfusion reserve (MPR), calculated as the ratio of stress to rest MBF, averages ~2.1 in healthy mice but is reduced to ~1.4 in HFHSD-fed models of coronary microvascular dysfunction. **Figure 14** illustrates impaired stress perfusion in an HFHSD-fed mouse compared to a healthy control.

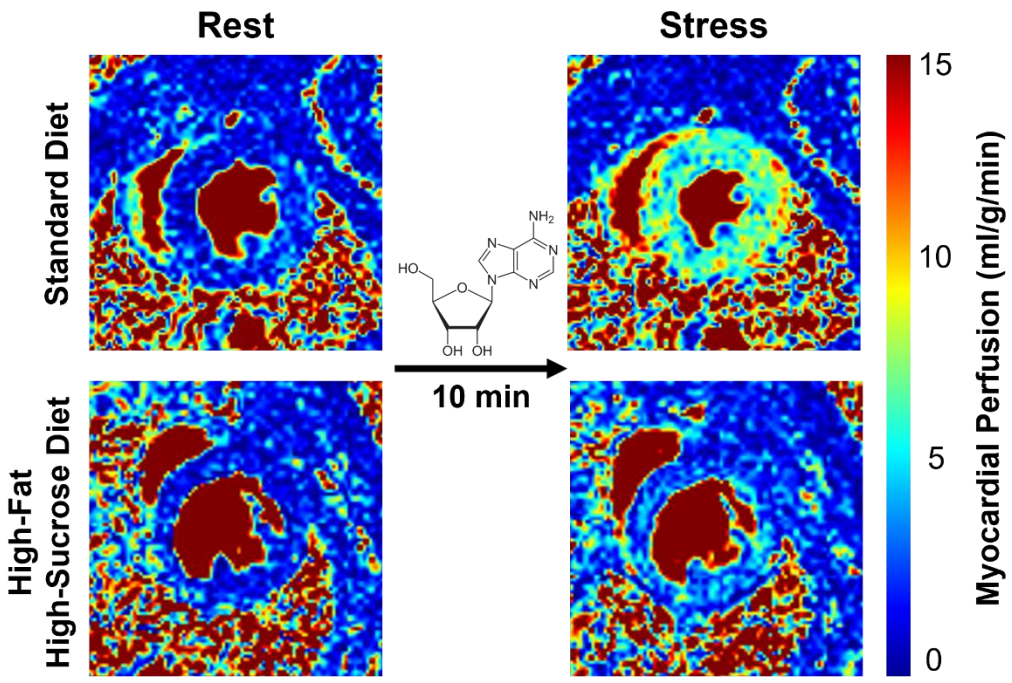

Figure 14 - Myocardial blood flow (MBF) maps at rest and after adenosine-induced stress in a standard diet-fed mouse (top row) and an HFHSD-fed mouse (bottom row). Stress-induced perfusion increases markedly in the healthy control, whereas the HFHSD-fed mouse shows a blunted response, consistent with impaired coronary microvascular function. Color bar indicates MBF in mL/g/min.

Myocardial strain imaging with displacement encoding with stimulated echoes (DENSE)

Myocardial strain imaging provides a sensitive measure of ventricular function by quantifying tissue deformation—specifically, the shortening, lengthening, and thickening of myocardial fibers—throughout the cardiac cycle. Unlike traditional metrics such as ejection fraction, strain can detect subclinical dysfunction earlier and has been shown to predict adverse cardiovascular outcomes[139].

DENSE is a CMR technique that encodes tissue displacement directly into the phase of the MR signal using a stimulated echo acquisition[140–142]. DENSE enables pixel-wise quantification of myocardial motion and has been adapted for use in small animal models[143,144]. Commonly

measured myocardial strains, including LV longitudinal and circumferential shortening and radial thickening, are depicted in **Figure 15A**[142]. Strain metrics include peak systolic strain, which reflects maximum contractile function, and peak diastolic strain rate, a load-independent marker of myocardial relaxation. Longitudinal strain maps in systole and global longitudinal strain-time curves from a HFHSD-fed obese mouse and a healthy mouse are shown in **Figure 15B-D**. Impaired diastolic strain rates, particularly in the longitudinal direction, have been associated with early diastolic dysfunction and adverse outcomes in heart failure with preserved ejection fraction (HFpEF)[145].

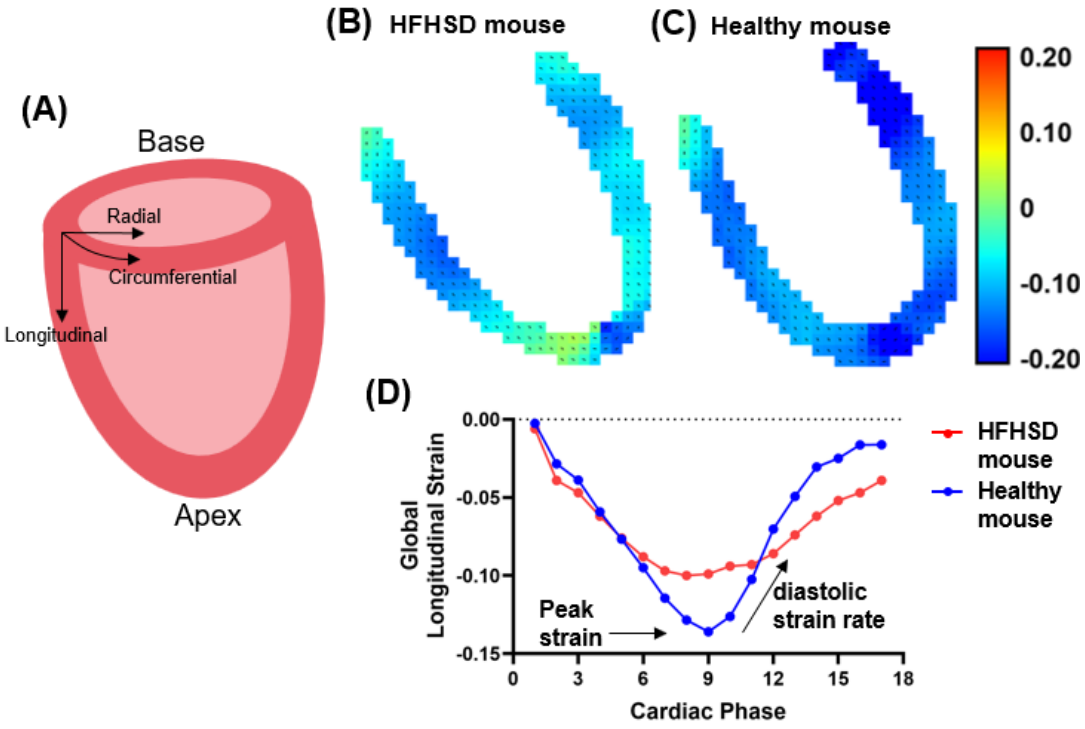

Figure 15 - Myocardial strain analysis using DENSE MRI. (A) Schematic of myocardial strain directions: radial, circumferential, and longitudinal.(B–C) DENSE-derived strain maps showing impaired strain in a HFHSD-fed mouse vs a healthy mouse. (D) Example global longitudinal strain curves across the cardiac cycle for a HFHSD-fed and healthy mouse highlighting peak systolic strain and diastolic strain rate differences.

Chapter 2: MRI of proinflammatory epicardial adipose tissue: Accelerated methods for simultaneous fatty acid composition and T_1 mapping and relationships to tissue biomarkers

2.1 Introduction

Epicardial adipose tissue (EAT) is a metabolically active visceral fat depot surrounding the heart which has emerged as a key player in the pathophysiology of various heart diseases, including atrial fibrillation, coronary artery disease, coronary microvascular disease, and heart failure with preserved ejection fraction (HFpEF)[66,67,82]. Notably, recent studies have shown that increased visceral adiposity is a near-universal feature of HFpEF, highlighting its integral role in disease pathophysiology[61]. Unlike other visceral fat depots, EAT is in direct contact with the myocardium and coronary arteries, without a fascia or other physical barrier to separate it from the heart. This unique anatomical feature allows for direct crosstalk between EAT and the myocardium through a shared microcirculation[3]. In healthy conditions, EAT supports cardiac function by providing fatty acids as an energy source, buffering excess circulating lipids, and maintaining features of brown and beige adipose tissue that support thermogenesis and cardiometabolic health[86]. However, in obesity and metabolic disease, EAT undergoes pathological remodeling, characterized by adipocyte hypertrophy, oxidative stress, and a shift in fatty acid composition (FAC) toward a proinflammatory profile[75,146,147]. Specifically, EAT in obesity becomes enriched with saturated fatty acids (SFAs) which activate toll-like receptor 4 (TLR4) signaling and the NLRP3 inflammasome[71,148]. This cascade promotes macrophage recruitment, polarization toward a proinflammatory M1 phenotype, and secretion of proinflammatory cytokines into the coronary microcirculation[149]. In contrast, monounsaturated (MUFAs) and polyunsaturated fatty acids (PUFAs) have been shown to impede NLRP3 inflammasome activity and mitigate inflammation, highlighting the FAC as a key mediator of EAT-driven cardiometabolic dysfunction[75,148]. Given the role of proinflammatory EAT in cardiovascular disease, it is emerging as a target for therapies such as sodium-glucose cotransporter-2 inhibitors (SGLT2i), which significantly improve

cardiovascular outcomes in HFpEF[98,150]. These drugs may exert their cardioprotective effects in part by modulating EAT biology, decreasing macrophage infiltration and promoting adipose tissue browning[151]. In this context, noninvasive imaging to assess proinflammatory EAT would have many potential applications.

MRI-based assessment of EAT has primarily focused on volume quantification, yet volume alone may not best reflect its proinflammatory state. Beyond EAT quantity, MRI techniques such as proton density fat fraction (PDFF) and FAC mapping enable the evaluation of adipose tissue quality. Prior studies using MRI FAC methods have shown that EAT SFA fraction is associated with left ventricular structural and functional impairments[28] as well as coronary microvascular dysfunction[31], suggesting their potential as biomarkers of proinflammatory EAT. Separately, T_1 mapping has shown promise in detecting adipose tissue remodeling, with longer T_1 relaxation times observed in adipose tissue from healthy individuals compared to those with obesity and in visceral adipose tissue (VAT) compared to subcutaneous adipose tissue (SAT)[92]. While EAT FAC MRI techniques have been applied in both preclinical[31] and clinical[28] settings, EAT T_1 mapping remains largely unexplored, and a joint approach to estimate both EAT FAC and T_1 has yet to be developed. Currently, FAC and T_1 mapping utilize separate acquisitions, which is time-inefficient. A joint approach to EAT FAC and T_1 mapping could offer a time-efficient and comprehensive characterization of EAT beyond volume alone.

While MRI-derived biomarkers for the assessment of EAT quality show promise, their relationships with direct histological and molecular tissue biomarkers remain largely unexamined. Establishing these relationships is essential for validating MRI as a noninvasive tool to assess proinflammatory EAT and its role in heart disease. In particular, showing how MRI mapping parameters relate to adipocyte morphology, macrophage infiltration, and cytokine expression

would establish a foundation for using MRI biomarkers for risk stratification and treatment monitoring.

This study presents an accelerated MRI method for simultaneous FAC and T_1 mapping of EAT in mice at 9.4T, enabling a more comprehensive assessment of its proinflammatory phenotype. Applying this novel method to diet-induced mouse models of metabolic heart disease, we investigate relationships between MRI-derived EAT parameters and ex vivo tissue measurements of inflammation, including macrophage presence, adipocyte morphology, and cytokine expression. Through these studies we aim to establish MRI-based biomarkers for the noninvasive assessment of proinflammatory EAT.

2.2 Theory

2.2.1 Signal model for joint FAC and T_1 mapping

The mean triglyceride spectrum can be characterized by nine distinct hydrogen-1 (^{1}H) resonances ($j \in \{A, \dots, I\}$) with relative magnitudes ρ_j and chemical shifts δ_j relative to the water proton resonance δ_w (Table 1)[22]. The relative phase of each resonance at time, t, after excitation is given by $\alpha_j(t) = \exp(i\gamma B_0(\delta_j - \delta_w)t)$, where B_0 is the main magnetic field strength and γ is the gyromagnetic ratio.

Water (W) and fat (F) components along with the T_1 relaxation time can be determined from a set of inversion recovery (IR) gradient echo (GRE) images acquired at multiple inversion times (TI_m, $m = 1, \dots, M$) and echo times (TE_n, $n = 1, \dots, N$) . The complex MR signal y at a given voxel is expressed as:

$$y(TE_n, TI_m) = \left(W + F \sum_{j=1}^{9} \rho_j \alpha_j(TE_n) \right) e^{i2\pi\psi TE_n} e^{i\phi} e^{-R_2^* TE_n} \left(A_0 - B_{diff} e^{-\frac{TI_m}{T_1^*}} \right) \quad (2.1)$$

Here, ψ represents off-resonance frequency due to static field inhomogeneity, ϕ is the initial phase, R_2^* is the transverse relaxation rate, and T_1^* is the apparent longitudinal relaxation time that differs from the true T_1 due to radiofrequency (RF) pulse effects on signal recovery. The constants, A_0 and B_{diff} correspond to the equilibrium signal and the signal difference between the initial (post-inversion) and equilibrium states. The true T_1 can be approximated using the conventional Look-Locker correction[152]:

$$T_1 = T_1^* \left(\frac{B_{diff}}{A_0} - 1 \right) \tag{2.2}$$

2.2.2 Characterization of triglyceride saturation

The relative magnitude of each triglyceride resonance is determined by the (1) number of -CH=CH- double bonds per triglyceride (ndb), (2) number of methylene- interrupted double bonds ($nmidb$), and (3) the fatty acid chain length (cl) (**Table 1**)[22]. To reduce the number of unknown parameters, the average chain length can be estimated based on prior knowledge. These parameters allow decomposition of the fat signal, F, into distinct triglyceride subcomponents:

$$F = F_{ntg} + F_{ndb} + F_{nmidb} \tag{2.3}$$

where F_{ntg} is proportional to the number of triglycerides, F_{ndb} to the number of double bonds, and F_{nmidb} to the number of methylene-interrupted double bonds.

The absolute values of ndb and $nmidb$ per "mean triglyceride" within a voxel are calculated as:

$$ndb = \frac{F_{ndb}}{F_{ntg}} \tag{2.4}$$

$$nmidb = \frac{F_{nmidb}}{F_{ntg}}. \tag{2.5}$$

The relative fractions of unsaturated fatty acids (UFAs) and PUFAs are given by:

$$\text{UFA} = \frac{ndb - nmidb}{3} \tag{2.6}$$

$$\text{PUFA} = \frac{nmidb}{3}. \tag{2.7}$$

Relative amounts of SFAs and MUFAs are determined using the relationships UFA = MUFA + PUFA and UFA + SFA = 100%[29].

Table 1 - Triglyceride ^{1}H resonances and their corresponding chemical shifts (δ) and relative magnitudes (ρ). cl = chain length, ndb = number of double bonds, $nmidb$ = number of methylene interrupted double bonds.

Resonance	Type	δ [ppm]	Relative magnitude ($\boldsymbol{\rho}$)
A	Methyl	0.90	9
B	Methylene	1.30	$[(cl-4)\times 6]-(ndb\times 8)+(nmidb\times 2)$
C	β-Carboxyl	1.60	6
D	α-Olefinic	2.02	$(ndb-nmidb)\times 4$
E	α -Carboxyl	2.24	6
F	Diacyl	2.75	$nmidb\times 2$
G	Glycerol	4.20	4
H	Glycerol	5.19	1
I	Olefinic	5.29	$ndb\times 2$

2.2.3 Least squares approximation

The complex signal for N echo times and M inversion times $\boldsymbol{y} = [y(TE_1, TI_1), \dots, y(TE_N, TI_1), \dots, y(TE_1, TI_M), \dots, y(TE_N, TI_M)]^T$ can be expressed in matrix form as

$$\boldsymbol{y} = \boldsymbol{\Psi}\mathbf{A}\mathbf{x}e^{-i\phi}, \tag{2.8}$$

where

$$\boldsymbol{A}_{(N*M)\times 4} = \begin{bmatrix} \alpha_{1,1,W} & \alpha_{1,1,A} & \dots & \alpha_{1,1,I} \\ \vdots & \vdots & \ddots & \vdots \\ \alpha_{N,1,W} & \alpha_{N,1,A} & \dots & \alpha_{N,1,I} \\ \alpha_{1,2,W} & \alpha_{1,2,A} & \dots & \alpha_{1,2,I} \\ \vdots & \vdots & \ddots & \vdots \\ \alpha_{N,M,W} & \alpha_{N,M,A} & \dots & \alpha_{N,M,I} \end{bmatrix} \times \underbrace{\begin{bmatrix} 1 & 0 & 0 & 0 \\ 0 & 9 & 0 & 0 \\ 0 & 6(cl-4) & -8 & 2 \\ 0 & 6 & 0 & 0 \\ 0 & 0 & 4 & -4 \\ 0 & 6 & 0 & 0 \\ 0 & 0 & 0 & 2 \\ 0 & 4 & 0 & 0 \\ 0 & 1 & 0 & 0 \\ 0 & 0 & 2 & 0 \end{bmatrix}}_{\boldsymbol{\rho}}. \tag{2.9}$$

Here, $\boldsymbol{x} = \left[W, F_{ntg}, F_{ndb}, F_{nmidb}\right]^T$ is the unknown parameter vector, and $\boldsymbol{\Psi}$ is the $(N * M) \times (N * M)$ block-diagonal matrix:

$$\boldsymbol{\Psi} = \text{blkdiag}\underbrace{(\boldsymbol{D}, \boldsymbol{D}, \dots \boldsymbol{D})}_{M \text{ times}}, \tag{2.10}$$

where each $N \times N$ diagonal block is

$$\boldsymbol{D} = diag\big(\exp(i2\pi\psi TE_1), \dots, \exp(i2\pi\psi TE_N)\big). \tag{2.11}$$

The $\boldsymbol{\rho}$ matrix describes the relative weights of water and ^{1}H triglyceride resonances as a function of the average fatty acid chain length, which is set to 16.12 based on prior knowledge of the visceral adipose tissue lipidome of mice fed a high-fat high-sucrose diet[153]. The terms

$$\alpha_{n,m,W} = \left(A_0 - B_{diff} e^{-\frac{TI_m}{T_1^*}}\right) \exp(-R_2^* TE_n) \tag{2.12}$$

and

$$\alpha_{n,m,j} = \left(A_0 - B_{diff} e^{-\frac{TI_m}{T_1^*}}\right) \exp\big(i\gamma B_0\big(\delta_j - \delta_w\big)TE_n\big) \exp(-R_2^* TE_n) \tag{2.13}$$

account for transverse and longitudinal relaxation effects and chemical shift-induced frequency changes of water and the j^{th} fat resonance.

The objective is to estimate the unknown parameter T_1^* and the vector $\boldsymbol{x}$ containing the water and fat components along with the confounding parameters ψ, ϕ, R_2^*, A_0, and B_{diff}. The

longitudinal relaxation parameters A_0, B_{diff}, and T_1^* are estimated by minimizing the squared residual error between the signal at TE_1, $\boldsymbol{y_{TE_1}} = [y(TE_1, TI_1), \dots, y(TE_1, TI_M)]$, and the three parameter model $\left(A_0 - B_{diff}e^{-TI/T_1^*}\right)$ using the Levenberg-Marquart algorithm. Once A_0, B_{diff}, and T_1^* are determined, the separable nonlinear problem can be solved using variable projection[29].

The confounding parameters ψ, ϕ, and R_2^* are estimated by minimizing

$$J(R_2^*, \psi, \phi) = \left\| \boldsymbol{y} - \boldsymbol{\Psi A}[Re(\mathbf{A}^H\mathbf{A})]^{-1}Re\left(\mathbf{A}^H\boldsymbol{\Psi}^H\boldsymbol{y}e^{-i\phi}\right)e^{i\phi}\right\|^2. \tag{2.14}$$

The phase term is determined analytically as

$$\hat{\phi} = \frac{1}{2}\arg((\boldsymbol{A}^H\boldsymbol{\Psi}^H\boldsymbol{y})^T[Re(\boldsymbol{A}^H\boldsymbol{A})]^{-1}(\boldsymbol{A}^H\boldsymbol{\Psi}^H\boldsymbol{y})) \tag{2.15}$$

for a given R_2^* and ψ.

2.2.4 Multicontrast image reconstruction

Images acquired at multiple TEs and TIs can be modeled as a superposition of a limited number of spectral components. Assuming that nonlinear variations vary smoothly over small regions, local image patches can be approximated as spectrally sparse, with signal primarily arising from modeled water and fat components. These properties support the use of higher-order low-rank regularization to exploit spatial similarity and redundancy through contrast dimensions.

A high-dimensionality undersampled patch-based reconstruction (HD-PROST) framework was employed to jointly enforce data consistency and a local low-rank structure[154]. The objective is to recover denoised images $\boldsymbol{X} \in \mathbb{C}^{n_x \times n_y \times N \times M}$ of size $n_x \times n_y$ with N TEs and M TIs from undersampled radial k-space data $\boldsymbol{Y}$. Assuming that $\boldsymbol{X}$ can be represented as a higher-order low-rank tensor on a patch scale, the reconstruction problem is formulated as:

$$\underset{\boldsymbol{X}}{\operatorname{argmin}} \frac{1}{2}\|\boldsymbol{\mathcal{E}X} - \boldsymbol{Y}\|_F^2 + \sum\nolimits_p \lambda_p \left\|\boldsymbol{T}_p\right\|_* \quad s.t. \boldsymbol{T}_p = \boldsymbol{P}_p(\boldsymbol{X}) \tag{2.16}$$

Here, $\boldsymbol{\mathcal{E}} = \boldsymbol{\mathcal{F}}\boldsymbol{E}$, where $\boldsymbol{\mathcal{F}}$ is the nonuniform fast Fourier transform (NUFFT) [155] and $\boldsymbol{E}$ is the ESPIRiT operator[156]. The operator $\boldsymbol{P}_p(\boldsymbol{X})$ extracts a patch of size P centered at pixel p, with patches stacked along the contrast dimensions to form a tensor $\boldsymbol{T}_p \in \mathbb{C}^{P\times N\times M}$. The nuclear norm $\|\boldsymbol{T}_p\|_*$ and regularization parameter λ_p promote low-rank across spatial, TE, and TI dimensions.

This problem is solved using the alternating direction method of multipliers (ADMM), which decomposes the problem into two alternating subproblems[157]. This process is outlined in **Figure 16**.

2.2.4.1 Optimization 1: Joint reconstruction

Given a denoised tensor $\boldsymbol{T}$ from Optimization 2 (as shown in **Figure 16**), the image $\boldsymbol{X}$ is updated by solving a Tikhonov-regularized least squares problem to enforce consistency with the measured k-space data:

$$\underset{\boldsymbol{X}}{\operatorname{argmin}} \frac{1}{2}\|\boldsymbol{\mathcal{E}}\boldsymbol{X} - \boldsymbol{Y}\|_F^2 + \frac{\mu}{2}\left\|\boldsymbol{T} - \boldsymbol{X} - \frac{\boldsymbol{b}}{\mu}\right\|_F^2 \tag{2.17}$$

where μ is a penalty parameter and $\boldsymbol{b}$ is the augmented Lagrange multiplier. The problem is solved using the conjugate gradient algorithm. After each iteration, the Lagrange multiplier is updated as $\boldsymbol{b}^{(i)} = \boldsymbol{b}^{(i-1)} + \boldsymbol{X}^{(i)} - \boldsymbol{T}^{(i)}$.

2.2.4.2 Optimization 2: Local low-rank denoising

The current image estimate $\boldsymbol{X}$ is divided into overlapping patches, each reshaped into a tensor $\widetilde{\boldsymbol{T}}_p \in \mathbb{C}^{P\times N\times M}$. Due to spatial similarity and redundancy across contrast dimensions, each tensor is expected to exhibit low-rank structure and is denoised using higher-order singular value decomposition (HOSVD). Orthonormal basis matrices $\boldsymbol{U}_{(1)}$, $\boldsymbol{U}_{(2)}$, and $\boldsymbol{U}_{(3)}$ are computed for the spatial, TE, and TI modes, respectively, and used to compute the core tensor :

$$\boldsymbol{S}_P = \widetilde{\boldsymbol{T}}_P \times_1 \boldsymbol{U}_{(1)}^H \times_2 \boldsymbol{U}_{(2)}^H \times_3 \boldsymbol{U}_{(3)}^H \tag{2.18}$$

where $\times_i$ represents the i^{th} mode product.

Singular value hard thresholding (SVHT) is applied to the core tensor, where components below an adaptive threshold are removed as they are assumed to primarily represent noise. Following the method proposed by Gavish and Donoho, the optimal hard threshold for a given patch core tensor λ_p is set to 2.39 times the median singular value across all dimensions[158]. The denoised patch tensor is then reconstructed by multiplying the thresholded core tensor with the corresponding orthonormal bases along each mode. All denoised patches are combined using weighted averaging of overlapping voxels yielding the tensor $\boldsymbol{T}$, which is used as the reference image in Optimization 1.

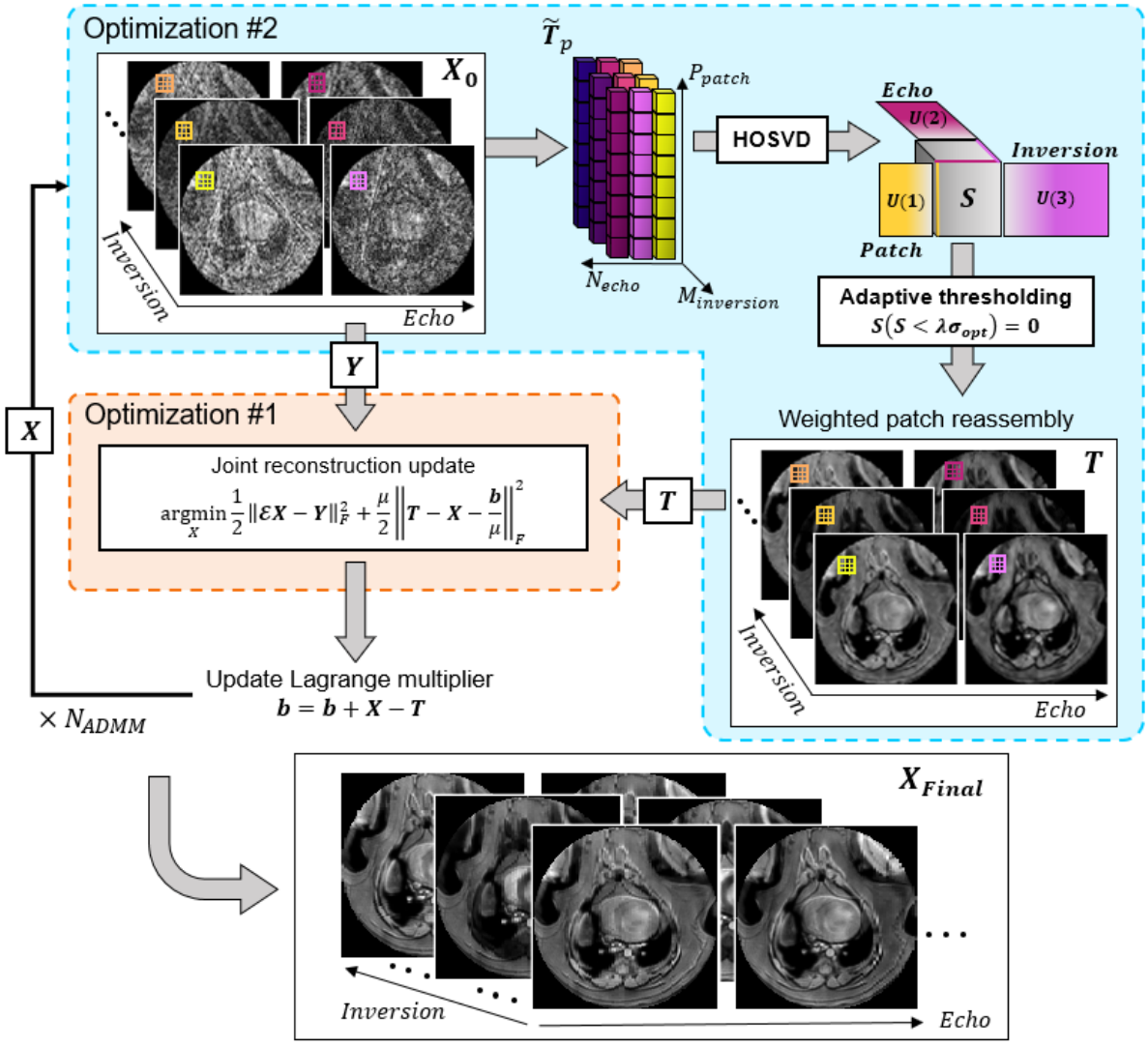

Figure 16 - Image reconstruction framework. The HD-PROST-based reconstruction alternates between two subproblems to recover denoised multicontrast images from undersampled radial k-space data. **Optimization 2:** The initial image estimate X_0, generated via NUFFT, is divided into overlapping patches. Patches from the same spatial location across all contrast dimensions are unfolded into 3D tensors ($\tilde{T}_p$) and denoised using higher-order singular value decomposition (HOSVD) followed by adaptive hard thresholding. Denoised patches are reassembled into a tensor $\boldsymbol{T}$. **Optimization 1:** A joint reconstruction update enforces data consistency with the measured k-space data Y and regularization toward the denoised image $\boldsymbol{T}$, yielding an updated image X. The Lagrange multiplier (b) is updated

after each iteration. This process is repeated for N_{ADMM} iterations to produce the final reconstructed image series X_{Final}. $\sigma_{opt} = median(S)$.

2.3 Methods

2.3.1 Pulse sequence

The proposed joint FAC and T_1 mapping pulse sequence is shown in **Figure 17A**. An electrocardiogram (ECG)-gated IR prepared interleaved multi-echo GRE pulse sequence with radial trajectories was developed to obtain images at multiple TEs and TIs. A slab-selective adiabatic 180° pulse was applied prior to initial excitation. Following a 15° excitation pulse, a monopolar double-echo readout was acquired using flyback gradient pulses with 2 ms echo spacing. Only two echoes were acquired per RF excitation because EAT in mice at 9.4T can have T_2^* values in the range of 5 ms, thus the signal-to-noise ratio (SNR) can be very low for additional echoes. Monopolar readouts were used to reduce the effects of eddy currents and gradient delays. Excitation and readout were repeated after each subsequent ECG trigger for approximately three times the maximum T_1 of interest followed by RR interval pauses for two times the maximum T_1 of interest to allow for complete magnetization recovery. Given a maximum T_1 of interest of 1000 ms and an average mouse RR interval of 100 ms, 30 TI acquisitions with TI_1 = 3.7 ms and ΔTI = RR interval were acquired followed by 20 RR pauses. This acquisition scheme was repeated for each radial spoke and again for each interleave. With each subsequent interleave, a delay of 0.2 ms was inserted prior to the double echo readout, enabling the acquisition of various echo times. Using 10 interleaves, 20 TE images were acquired with effective echo spacing of 0.2 ms. The choice of TEs and echo spacing were chosen to minimize the variance in the estimates of the water and fat components as shown by Berglund et al[159].

To create spatiotemporally incoherent aliasing patterns at each TE and TI, a golden-angle rotated stack-of-stars sampling scheme was implemented as shown in Figure 2B. For N_S radial spokes, the projection angle for the i^{th} projection, n^{th} echo time, and m^{th} inversion time was calculated as:

$$\theta(i,n,m) = \text{mod}\left((i-1)\times\pi\times\frac{\sqrt{5}-1}{2},\pi\right) + \text{mod}\left((n-1)\times\frac{\pi}{N_S}\times\frac{\sqrt{5}-1}{2},\frac{\pi}{N_S}\right) + \text{mod}\left((m-1)\times\frac{\pi}{N_S}\times\frac{\sqrt{5}-1}{2},\frac{\pi}{N_S}\right). \quad (19)$$

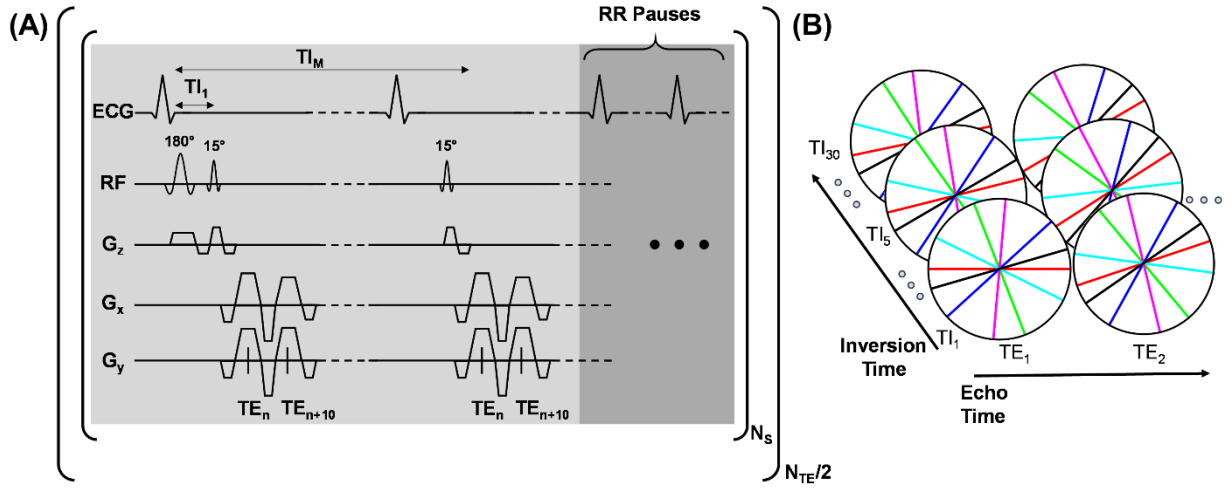

Figure 17 - Pulse sequence diagram. (A) Inversion recovery interleaved multi-echo sequence for ***M*** inversion times (TIs) and ***N*** echo times (TEs), showing the acquisition of a single radial spoke at TE_n and TE_{n+10} across multiple TIs, followed by RR pauses. (B) Example k-space trajectories with golden-angle rotation in-plane and through contrast dimensions, illustrating six spokes acquired at different TEs and TIs. N_s = number of spokes. N_{TE} = number of total echo times.

2.3.2 Image reconstruction and parameter mapping

Image reconstruction and parameter mapping were implemented in MATLAB R2023a (MathWorks, Natick, MA). First, k-space trajectories for each radial spoke at each TE and TI were corrected for gradient delays along all spatial axes using independently acquired calibration data[160,161]. Delays ranged from 2.1 to 2.6 μs, 3.2 to 3.4 μs, and -0.6 to 0.4 μs for the sagittal, coronal, and axial axes, respectively. To enable application of the method to multi-coil arrays, coil sensitivity maps and combination were performed using ESPIRiT with maps computed from the first TE and TI coil images[156]. Image reconstruction was performed using the HD-PROST-based framework as detailed in Section 2.2.4. A patch size of 3×3 and a patch stride of 1 were used. The reconstruction was performed over 5 ADMM iterations. The regularization parameter $\mu = 0.75$ was selected empirically and held constant across datasets.

Multi-TI images at the first TE were used to approximate T_1. Due to heart rate (HR) variability during the scan, the different radial spokes of each TI image were acquired at slightly different TIs, resulting in clusters of TIs for each image. To account for this variation, as previously described, a fuzzy C-means (FCM) clustering algorithm was used to determine the cluster of specific radial spokes corresponding to each TI, and the cluster centers were computed and used as the effective TIs[138]. Then, T_1^*, A_0, and B_{diff} were computed, followed by the determination of T_1 using Equation 2.2.

A conventional whole-image optimization algorithm was employed to estimate the spatially smooth field map, ψ, by minimizing Equation 2.14[162]. The transverse relaxation rate R_2^* was determined through a brute-force search over discretized values from 0 to 500 s^{-1} in 0.5 s^{-1} increments. The initial phase, ϕ, was then calculated using Equation 2.15. The parameter vector, $\boldsymbol{x}$, containing water and fat components, was derived as previously described [28]. Once $\boldsymbol{x}$ was

determined, ndb, $nmidb$, UFA, and PUFA (Equations 2.4-2.7) were computed and used to calculate SFA and MUFA. The proton density fat fraction (PDFF), representing the proportion of total signal from fat protons, was calculated as $F / (F + W)$.

2.3.3 Phantom validation and selection of acceleration rate

Two phantoms were used to validate FAC and T_1 mapping. The FAC phantom consisted of five 1 mL vials containing olive, sesame, and flaxseed oils, along with a 50/50 coconut/avocado oil mixture and a 25/75 coconut/sesame oil mixture, placed in a 5 mL conical tube of water. These oils were selected to span a broad FAC range comparable to in vivo adipose tissue[76]. The T_1 phantom contained 1 mL vials of water with gadolinium (Gd) concentrations ranging from 0.1 to 0.5 mM for T_1 mapping validation.

Joint FAC and T_1 imaging was performed at 9.4T (Biospec 94/20, Bruker Biospin, Germany) using a 600-bpm simulated ECG signal (SA Instruments, Inc., Stony Brook, NY). Approximately fully sampled images (202 spokes) were acquired with the following parameters: slice thickness = 1 mm, field-of-view (FOV) = 35 x 35 mm, flip angle = 15°, acquisition matrix = 128 x 128, resolution = 0.27 x 0.27 mm^2**,** bandwidth (BW) = 100 kHz, 30 TIs (TI_1 = 3.7 ms, ΔTI = 100 ms), and 20 TEs (TE_1 = 1.3 ms, ΔTE = 0.2 ms). Images were retrospectively undersampled such that the number of spokes used were Fibonacci numbers (from 144 to 1), guaranteeing uniform coverage of k-space[9]. A region of interest (ROI) was drawn for each oil sample and the mean SFA fraction, MUFA fraction, PUFA fraction, PDFF, T_1, and R_2^* were calculated. The PUFA fraction calculation assumes that fatty acids have at most two double bonds, which is valid for approximately 98% of adipose tissue fatty acids but not for certain plant oils containing significant triunsaturated fatty acids. To account for this, the PUFA fraction was adjusted using a fixed triunsaturated fatty acid fraction (F_{TRIFA}) measured by NMR for each oil, by applying the formula

$PUFA = \frac{nmidb}{3} - F_{TRIFA}$. Mean absolute error (MAE) was computed between fully sampled and retrospectively undersampled SFA fraction, MUFA fraction, PUFA fraction, PDFF, T_1, and R_2^* maps for all acceleration rates. The structural similarity (SSIM) index[163] was computed between denoised fully sampled and denoised retrospectively undersampled images over the entire oil phantom region, excluding background pixels.

Reference SFA fraction, MUFA fraction, and PUFA fraction were determined by NMR spectroscopy as previously described[28]. Reference T_1 values were determined using a conventional ECG-gated IR T_1 mapping method with the following acquisition parameters: slice thickness = 1 mm, FOV = 35 x 35 mm, flip angle = 1°, acquisition matrix = 128 x 128, resolution = 0.27 x 0.27 mm^2**,** BW = 100 kHz, 30 TIs (TI_1 = 3.7 ms, ΔTI = 100 ms)**.** Agreement between joint FAC and T_1 values and reference methods across acceleration rates was evaluated using linear regression, with Pearson's correlation coefficients (*r*) and *p*-values assessing linearity and significance.

2.3.4 In vivo MRI protocol and image analysis

All animal studies were performed in accordance with protocols that conformed to the Declaration of Helsinki as well as the Guide for Care and Use of Laboratory Animals[164] and were approved by the Animal Care and Use Committee at the University of Virginia. Mice were maintained at the University of Virginia Center for Comparative Medicine pathogen-free vivarium facility. MRI was performed on a 9.4T system using a ^{1}H transmit-receive quadrature volume RF coil (35 mm inner diameter, Bruker BioSpin GmbH, Germany). During imaging, mice were anesthetized with 1.25% isoflurane, and core temperature was maintained at 36 ± 0.5°C using circulating warm air. The ECG, body temperature, and respiration were monitored (SA Instruments, Inc., Stony Brook, NY). Localizer imaging was performed to establish a mid-ventricular axial slice with sufficient EAT. Undersampled IR multi-echo images for joint FAC and

T_1 mapping were acquired using the pulse sequence described in Section 3.1. Acquisition parameters included: slice thickness = 1 mm, FOV = 25 x 25 mm, flip angle = 15°, acquisition matrix = 128 x 128, resolution = 0.2 x 0.2 mm^2, BW = 100 kHz, N_S = 21, 30 TIs (TI_1 = 3.7 ms, ΔTI = RR interval ms), and 20 TEs (TE_1 = 1.3 ms, ΔTE = 0.2 ms), with a total scan time of approximately 17 minutes.

Images and parameter maps were reconstructed as described in Section 3.2. The EAT and SAT were manually segmented using the images of total fat content F, excluding border pixels to avoid partially volumed voxels. ROIs included voxels from artifact free regions with a PDFF > 50% and included at least 30 pixels per depot. The mean parameter values were calculated for each depot, and EAT parameter indexes were computed as the ratio of the mean EAT to SAT values for SFA fraction, MUFA fraction, PUFA fraction, and PDFF. These EAT quality metrics were indexed to their SAT counterparts as SAT is considered a metabolically healthier adipose depot[60,165–167]. Thus, the ratio utilized an intra-subject reference and accounted for inter-subject differences in overall inherent adipose physiology (e.g., lipid metabolism, deposition, and synthesis)[76,166]. Relaxation parameters, T_1 and R_2^*, were not indexed, as they reflect more than differences in physiology, such as local field inhomogeneities.

2.3.5 Application of joint FAC and T_1 mapping to mouse models of metabolic heart disease with differing EAT FAC and inflammatory profiles

This study applied joint FAC and T_1 mapping to investigate relationships between MRI-derived EAT parameters and tissue markers of inflammation, including adipocyte size, macrophage infiltration, and proinflammatory cytokines. To generate a range of adipose tissue compositions, three groups of C57Bl/6J mice (n = 16-20 mice/group, Jackson Laboratories, Bar Harbor, Maine; strain #000664) were studied: (1) mice fed a high-fat high-sucrose diet (HFHSD) (40% kcal fat,

40% kcal sucrose; Diet 123727, Research Diets, Inc., New Brunswick, NJ), (2) mice fed an HFHSD plus the SGLT2i, empagliflozin (EMPA) (40% kcal fat, 40% kcal sucrose, 30 mg/kg/day EMPA; Diet 21011406, Research Diets, Inc), and (3) mice fed a high-fat diet (HFD) (60% kcal fat; Diet 12492, Research Diets, Inc.). Diets began at 6-8 weeks of age and continued for 18 weeks.

These groups were selected to induce varying metabolic conditions, VAT inflammation, EAT development, and distinct FAC profiles across various adipose depots. The HFD consisted of 245 g lard (40% SFA, 45% MUFA, 10% PUFA) and 25 g soybean oil (15% SFA, 23% MUFA, 58% PUFA), resulting in an overall composition of 39% SFA, 45% MUFA, and 16% PUFA. The HFHSD included 135 g coconut oil (94% SFA, 5% MUFA, 1% PUFA) and 45 g soybean oil (15% SFA, 23% MUFA, 58% PUFA), yielding 75% SFA, 10% MUFA, and 15% PUFA. HFD-fed mice were expected to exhibit a lower SFA fraction and a higher MUFA fraction, while HFHSD-fed mice were expected to show a higher SFA fraction and a lower MUFA fraction. Though designed to modulate FAC composition, both HFHSD and HFD mice develop VAT inflammation and metabolic heart disease[168]. EMPA was included due to its known effects on VAT, including reducing inflammation, adipose tissue browning, and altering lipid metabolism via decreased lipogenesis and increased lipolysis[151,169]. The addition of EMPA to HFHSD-fed mice allowed for sufficient weight gain and EAT development while modifying EAT FAC and reducing inflammation.

2.3.6 Histology

EAT was collected after CO_2 induced death and fixed in 4% PFA in PBS for 7-10 days at 4°C. EAT was paraffin embedded and cryosectioned at 5 μm thickness and mounted. Slides were deparaffinized. Briefly, sections were submerged in xylene (3 minutes), 1:1 xylene:ethanol (3 minutes) 100% ethanol (2x3 minutes), 95% ethanol (3 minutes), 70% ethanol (3 minutes), and

50% ethanol (3 minutes). Antigen retrieval was performed using citrate-based solution (Vector Laboratories H-330) where slides were submerged in antigen retrieval solution and heated to boiling for 20 minutes, slides were then cooled for 1 hour at room temperature. Tissue sections were then blocked for 1 hour in antibody blocking buffer (FGS, donkey serum) at room temperature. Antibody blocking buffer was removed and replaced with antibody blocking buffer containing primary antibody overnight at 4°C. Sections were then washed (PBS+FGS+Tween for 5 minutes, 2X PBS 5 minutes) and incubated in antibody blocking buffer containing secondary antibody (1:100) for 1 hour at room temperature protected from light. Sections were washed (3xPBS) and counterstained with DAPI (Thermo Fisher Scientific D3571) before mounting. Sections were imaged on an Olympus Fluoview 1000 and are representative images of composite z-stacks. Analysis (thresholding and manual counting) was performed in ImageJ.

2.3.7 Cytokine assays

Hearts and EAT were snap frozen in liquid nitrogen prior to sample preparation after CO_2 induced death. Hearts and EAT were homogenized in 1:1 PBS and Cell Lysis buffer (R&D Systems 895347) by bead homogenization. 200 μL of tissue lysate was provided for Luminex analysis with the Flow Cytometry Core at the University of Virginia School of Medicine. Mouse 32-plex panel analysis was performed on each sample in triplicate (**Table 2**). Quantification was performed relative to standard curve for each independent cytokine. Each cytokine was normalized to total protein per individual sample.

Table 2 – Cytokines included in the mouse 32-plex Luminex panel.

Cytokine Name	Abbreviation(s)
Granulocyte colony-stimulating factor	G-CSF
Eotaxin	CCL11
Granulocyte-macrophage colony-stimulating factor	GM-CSF/CSF2
Interferon-gamma	IFN-γ
Interleukin-1 alpha	IL-1α
Interleukin-1 beta	IL-1β
Interleukin-2	IL-2
Interleukin-3	IL-3
Interleukin-4	IL-4
Interleukin-5	IL-5
Interleukin-6	IL-6
Interleukin-7	IL-7
Interleukin-9	IL-9
Interleukin-10	IL-10
Interleukin-12 (p40 subunit)	IL-12 (p40)
Interleukin-12 (p70 subunit)	IL-12 (p70)
Interleukin-13	IL-13
Interleukin-15	IL-15
Interleukin-17	IL-17
Leukemia inhibitor factor	LIF
Lipopolysaccharide-induced CXC chemokine	LIX/CXCL5
Interferon-gamma-induced protein 10	IP-10/CXCL10
Keratinocyte chemoattractant	KC/CXCL1
Monocyte chemoattractant protein-1	MCP-1/CCL2
Macrophage inflammatory protein-1 alpha	MIP-1α/CCL3
Macrophage inflammatory protein-1 beta	MIP-1β/CCL4
Macrophage colony-stimulating factor	M-CSF/CSF-1
Monocyte chemoattractant protein-2	MIP-2/CXCL2
Monokine induced by gamma interferon	MIG/CXCL9
Regulated upon activation normal T-cell expressed and secreted	RANTES/CCL5
Vascular endothelial growth factor	VEGF
Tumor necrosis factor alpha	TNF-α

2.3.8 Statistics

All statistical analyses were performed using GraphPad Prism 10.4.0. Group comparisons for EAT and SAT parameters were conducted using one-way analysis of variance with Fisher's least significant difference post-hoc tests to assess differences among groups. Spearman correlation coefficients (r) and associated p-values were calculated to evaluate associations between MRI-derived parameters and tissue markers of inflammation. A significance threshold of $p < 0.05$ was used.

2.4 Results

2.4.1 Phantom validation and selection of acceleration rate

To determine the optimal acceleration rate, an error analysis was performed comparing accelerated acquisitions to fully sampled images and maps. Rate-9.6 acceleration (21 spokes per image) was identified as optimal, achieving a scan time of approximately 17 minutes while maintaining low MAEs of 0.91% for SFA fraction, 0.82% for MUFA fraction, 0.12% for PUFA fraction, 0.40% for PDFF, 22.36 ms for T_1, and 6.26 s^{-1} for R_2^* with an SSIM > 0.80 (**Figure 18**).

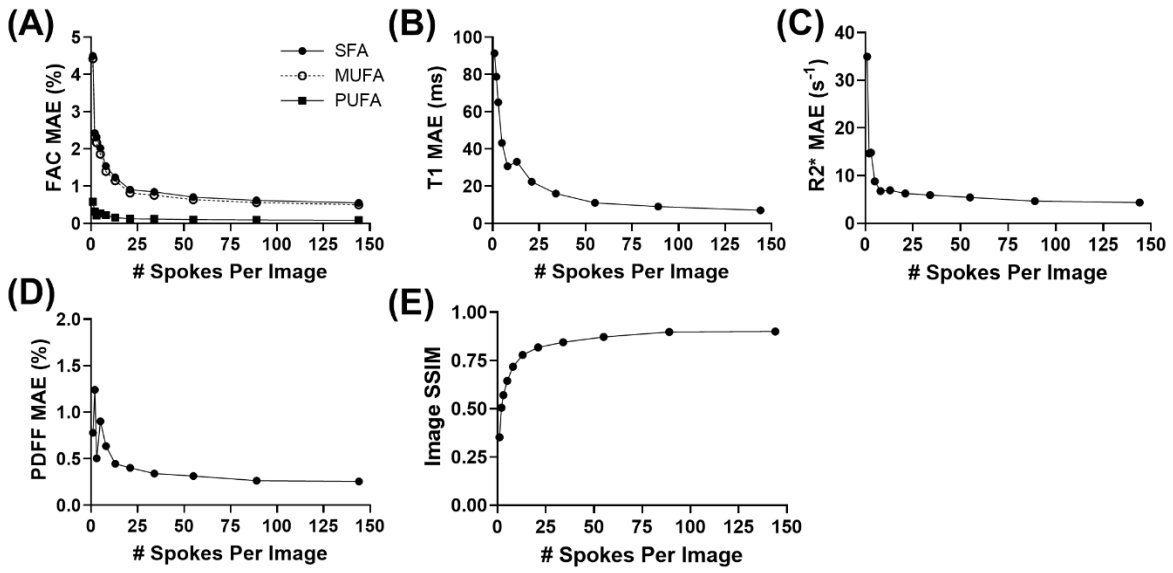

Figure 18 - Error analysis of retrospectively undersampled images. Mean absolute error (MAE) between (A) SFA, MUFA, and PUFA fractions, (B) T_1, (C) R_2^*, and (D) PDFF values computed from retrospectively undersampled phantom images and fully sampled acquisitions. (E) Structural similarity (SSIM) index between denoised retrospectively undersampled and fully sampled images. FAC, fatty acid composition; PDFF, proton density fat fraction; SFA, saturated fatty acid; MUFA, monounsaturated fatty acid; PUFA, polyunsaturated fatty acid.

Next, the accuracy of joint FAC and T_1 estimations were validated against NMR (FAC) and conventional MRI T_1 mapping. **Figure 19B** shows fully sampled and rate-9.6 undersampled parameter maps in the FAC and T_1 phantoms. Phantom validation demonstrated strong correlations ($r > 0.94$, $p < 0.05$) between reference and measured values, confirming the accuracy of the joint method (**Figure 19C**). For fully sampled acquisitions, regression analysis yielded slopes of 0.99, 1.17, and 1.16 with biases of -3.35, -0.55, and -7.42 for SFA, MUFA, and PUFA fractions respectively, and a slope of 1.05 with a bias of 0.03 for T_1. For rate-9.6 accelerated acquisitions, regression slopes remained similar at 1.04, 1.16, and 1.14 with biases of -4.5, -0.53, and -7.66 for SFA, MUFA, and PUFA fractions, and a slope of 1.03 with a bias of -0.02 for T_1.

MAEs between fully sampled joint FAC and T_1 mapping values and reference measurements were 4.02% (SFA), 10.15% (MUFA), and 6.28% (PUFA) compared to NMR, and 8.66 ms for T_1 compared to reference T_1 mapping. For rate-9.6 accelerated acquisitions, MAEs remained similar at 3.57% (SFA), 10.03% (MUFA), 6.49% (PUFA), and 7.71 ms for T_1, demonstrating that acceleration maintains measurement accuracy.

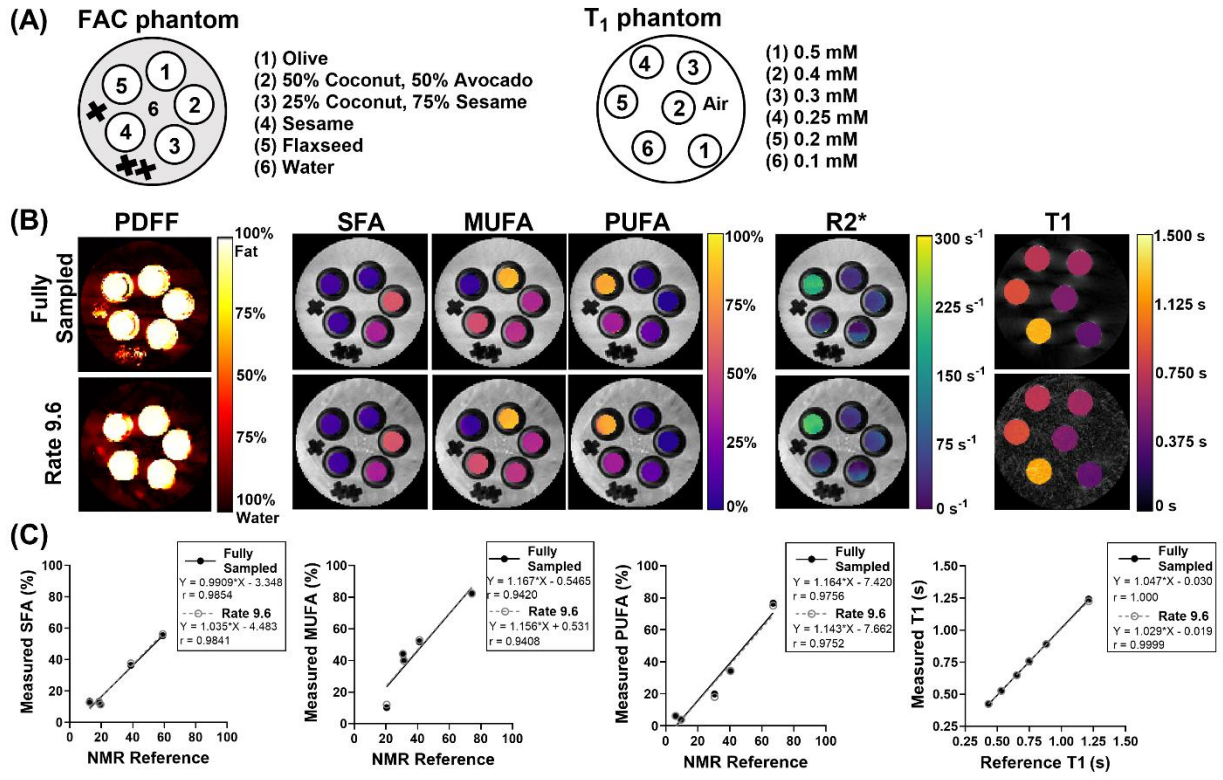

Figure 19 - Phantom layout and parameter maps. (A) Layout of oil and gadolinium (Gd) phantoms used for FAC and T_1 validation, respectively. The FAC phantom consists of five 1 mL oil mixtures submerged in 5 mL of water, while the T_1 phantom contains six 1 mL vials of water with Gd concentrations ranging from 0.1 to 0.5 mM. (B) Parameter maps of PDFF, SFA/MUFA/PUFA fractions, R_2^*, and T_1 for fully sampled and rate-9.6 accelerated acquisitions, overlaid on the phantom images. (C) Linear regression analysis between joint FAC and T_1 measured

values and reference values for fully sampled and rate-9.6 accelerated acquisitions. Pearson *r* values are reported. Abbreviations as in **Figure 18**.

2.4.2 Accelerated in-vivo images and parametric mapping

Example NUFFT- and HD-PROST-reconstructed images at multiple TEs and TIs are shown in **Figure 20** for two different acceleration rates. While phantom imaging allowed for fully sampled reference images, the associated scan time (~2.8 hours) was not feasible for in vivo mouse imaging. Instead, a 55-spoke acquisition (46 min, rate-3.7) followed by a 21-spoke acquisition (17 min, rate-9.6) was performed in the same mouse to compare image quality. This combined scan time represented the longest feasible in vivo imaging duration. The 21-spoke acquisition was chosen based on phantom analysis determining the optimal acceleration rate. Although the undersampled images exhibit substantial noise-like artifacts, the reconstruction effectively reduces these artifacts while preserving image quality. The rate-9.6 acquisition produces images comparable to the highly sampled rate-3.7 acquisition, with an SSIM of 0.91 computed over the mouse body, supporting the choice of rate-9.6 for in vivo imaging.

Example rate-9.6 accelerated in vivo parameter maps are shown in **Figure 21**. Water (W) and fat (F) signal images, and maps of PDFF and off-resonance (ψ) are displayed, along with R_2^*, T_1, SFA fraction, MUFA fraction, and PUFA fraction maps overlaid on EAT and SAT regions.

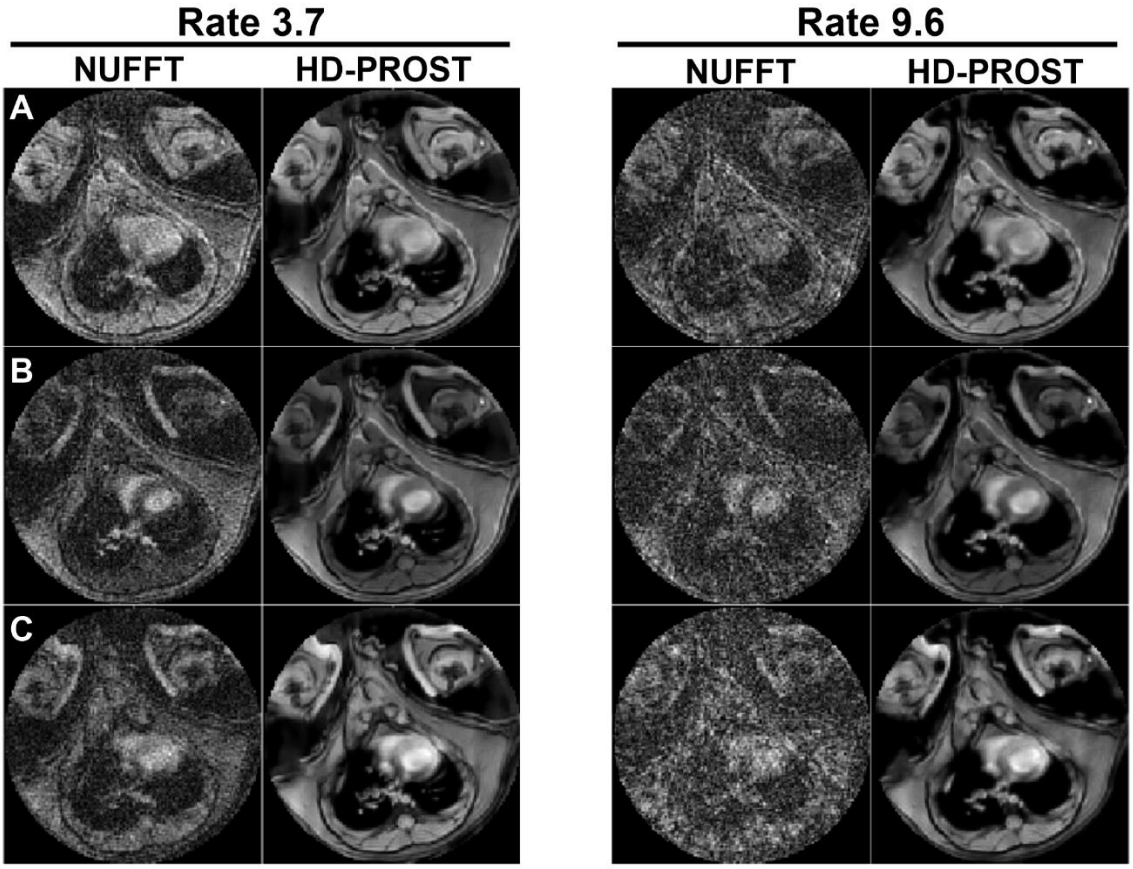

Figure 20 - Comparison of undersampled and HD-PROST reconstructed in vivo images. Non-uniform fast Fourier transform (NUFFT) undersampled and HD-PROST reconstructed images acquired at acceleration rates 3.7 and 9.6 for (A) TE_1, TI_1, (B) TE_1, TI_{15}, and (C) TE_4, TI_{30} in the same mouse with high-fat high-sucrose diet-induced obesity.

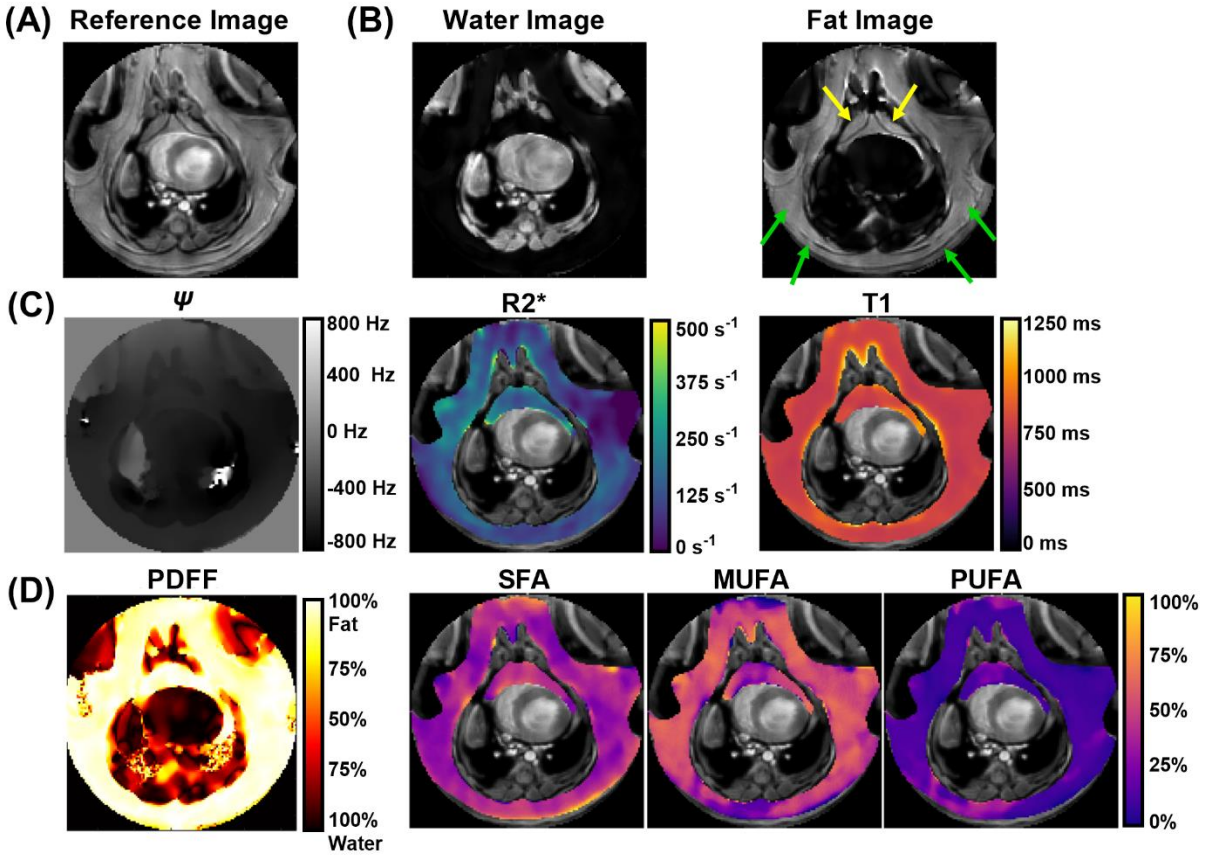

Figure 21 - In vivo parametric maps from a representative HFHSD mouse. Images from a mid-ventricular axial slice showing: (A) T_1-weighted reference image, (B) water (*W*) and fat (*F*) signal images (yellow arrows = epicardial adipose tissue [EAT], green arrows = subcutaneous adipose tissue [SAT]), (C) maps of off-resonance (ψ), R_2^*, and T_1, and (D) fat parameter maps including PDFF, SFA fraction, MUFA fraction, and PUFA fraction. Parameter maps are overlaid on manually contoured EAT and SAT regions. HFHSD, high-fat high-sucrose diet. All other abbreviations as in **Figure 18**.

2.4.3 Joint FAC and T_1 mapping detects diet and SGLT2-inhibitor induced differences in EAT and SAT properties

Absolute EAT SFA, MUFA, PUFA, PDFF, T_1, and R_2^* results for each group of mice are summarized in **Figure 22A**. EAT FAC profiles differed significantly across all groups. HFHSD

mice had the highest EAT SFA faction and lowest EAT MUFA fraction, with significantly higher SFA fraction compared to HFHSD+EMPA ($p < 0.05$) and HFD ($p < 0.0001$) mice, and significantly lower MUFA ($p < 0.0001$) and PUFA ($p < 0.05$) fraction compared to HFD mice. Additionally, HFHSD+EMPA mice exhibited higher EAT SFA fraction ($p < 0.01$) and lower MUFA fraction ($p < 0.01$) than HFD mice. HFHSD+EMPA mice exhibited significantly higher R_2^* ($p < 0.05$) and T_1 ($p < 0.05$) in the EAT compared to HFHSD mice.

SAT parameter results are summarized in **Figure 22B**. HFD mice had the lowest SAT SFA fraction and highest SAT MUFA fraction with significant differences compared to HFHSD ($p < 0.0001$) and HFHSD+EMPA ($p < 0.0001$) mice. HFD mice also exhibited an elevated SAT PUFA fraction compared to HFHSD+EMPA ($p < 0.001$) and HFHSD ($p < 0.05$) mice. SAT PDFF was the lowest in the HFD mice compared to both HFHSD ($p < 0.05$) and HFHSD+EMPA mice ($p < 0.05$). HFD mice also exhibited the longest SAT T_1 compared to HFHSD ($p < 0.01$) and HFHSD+EMPA ($p < 0.05$) mice. HFHSD mice had lower SAT R_2^* compared to HFHSD+EMPA ($p < 0.01$) and HFD ($p < 0.05$) mice.

The EAT parameters indexed to those of SAT were compared between groups. The indexed parameters revealed a distinct profile, with HFHSD+EMPA mice displaying significantly reduced EAT SFA index compared to HFHSD ($p < 0.01$) and HFD ($p < 0.05$) mice (**Figure 22C**). HFHSD+EMPA mice also exhibited a significantly higher MUFA ($p < 0.01$) and PUFA ($p < 0.05$) index than HFHSD mice.

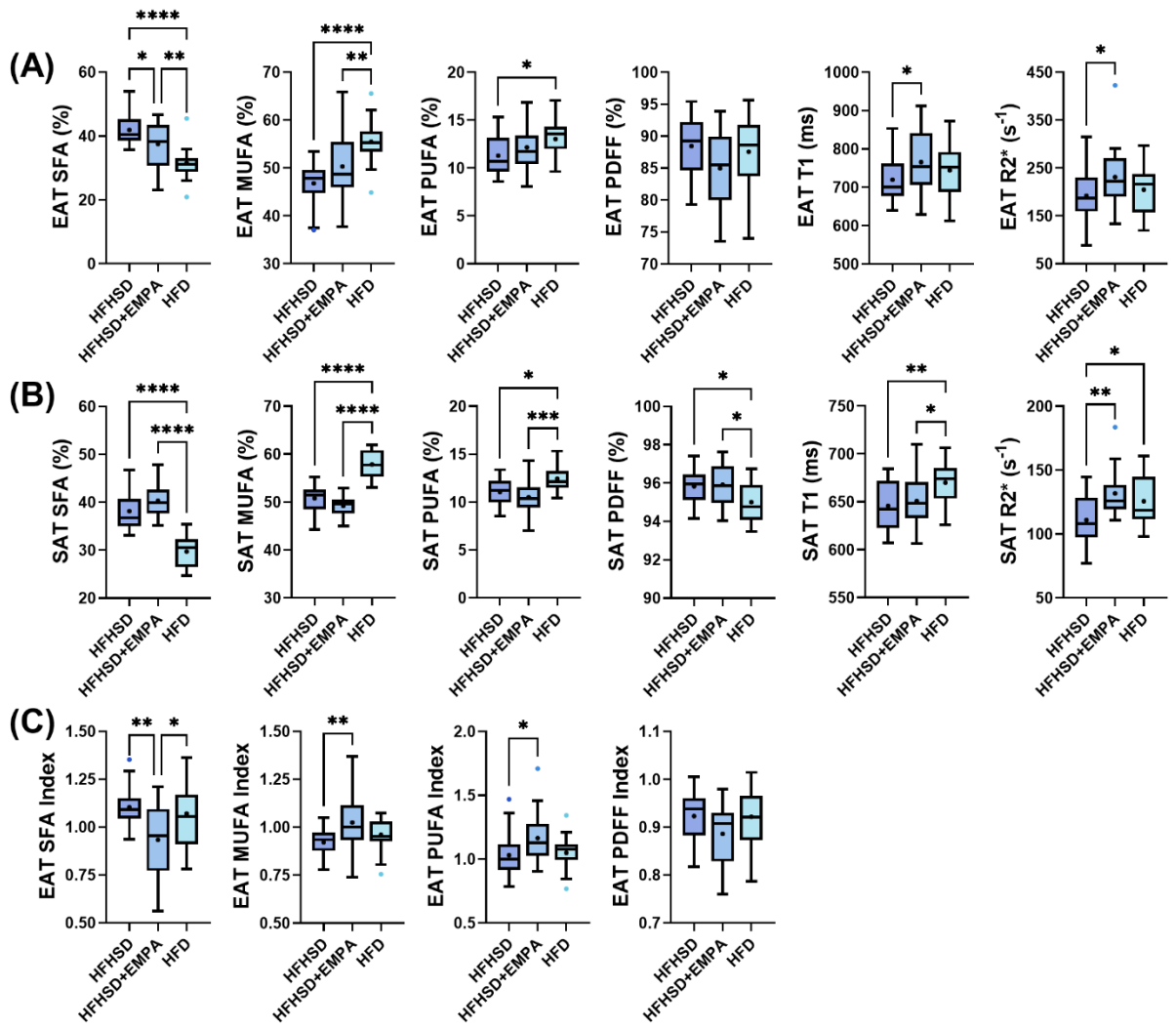

Figure 22 - Diet and SGLT2 inhibitor-induced differences in adipose tissue MRI parameters. Tukey boxplots of absolute SFA fraction, MUFA fraction, PUFA fraction, PDFF, T_1, and R_2^* values for (A) EAT and (B) SAT in mice fed an HFHSD (n=20), HFHSD+EMPA (n=17), or HFD (n=16) for 18 weeks. (C) EAT index values for SFA, MUFA, PUFA, and PDFF in the same groups. *$p < 0.05$, **$p < 0.01$, ***$p < 0.001$, and ****$p < 0.0001$. HFHSD, high-fat high-sucrose diet; EMPA, empagliflozin; HFD, high-fat diet. All other abbreviations as in **Figure 18.**

2.4.4 MRI biomarkers of EAT correlate with histological and cytokine markers of inflammation

To investigate associations between EAT MRI parameters and tissue-level markers of inflammation, we analyzed correlations between MRI-derived EAT indexes and histological and cytokine measures in both EAT and cardiac tissue. **Figure 23** presents representative EAT images depicting varying inflammatory phenotypes from each mouse group stained for F4/80+ macrophages and hematoxylin and eosin (H&E) for adipocyte morphology. Macrophage infiltration is higher in the HFD and HFHSD groups but reduced with EMPA. H&E reveals larger adipocytes in HFD and HFHSD mice**,** while EMPA-treated mice show smaller, more uniform adipocytes.

Significant ($p < 0.05$) relationships between in vivo MRI parameters (SFA, MUFA, PUFA, PDFF indexes, R_2^*, and T_1) and ex vivo tissue measurements are shown in **Figure 24.** EAT SFA index positively correlated with EAT macrophage infiltration, assessed as the ratio of macrophages per adipocyte ($r = 0.440$, $p = 0.022$), and granulocyte-macrophage colony-stimulating factor (GM-CSF) levels in the EAT ($r = 0.764$**,** $p = 0.009$). In contrast, EAT MUFA index negatively correlated with GM-CSF levels in the EAT ($r = -0.709$, $p = 0.018$). EAT PUFA index was positively correlated with interleukin (IL)-10 ($r = 0.487$, $p = 0.021$) in the EAT, and negatively correlated with cytokine expression in the heart, including interferon gamma (IFN-γ) ($r = -0.618$, $p = 0.048$), IL-1α ($r = -0.438$, $p = 0.037$), and IL-2 ($r = -0.468$, $p = 0.021$). EAT PDFF index showed a positive correlation with leukemia inhibitor factor (LIF) ($r = 0.571$, $p = 0.023$) levels in the EAT. Among MRI relaxation parameters, EAT T_1 negatively correlated with EAT adipocyte size ($r = -0.464$, $p = 0.022$) and macrophage inflammatory protein 1-alpha (MIP-1α) levels in the EAT ($r = -0.422$, $p = 0.045$). EAT R_2^* also negatively correlated EAT MIP-1α levels ($r = -0.421$, $p = 0.045$). No other significant associations with inflammatory markers were observed.

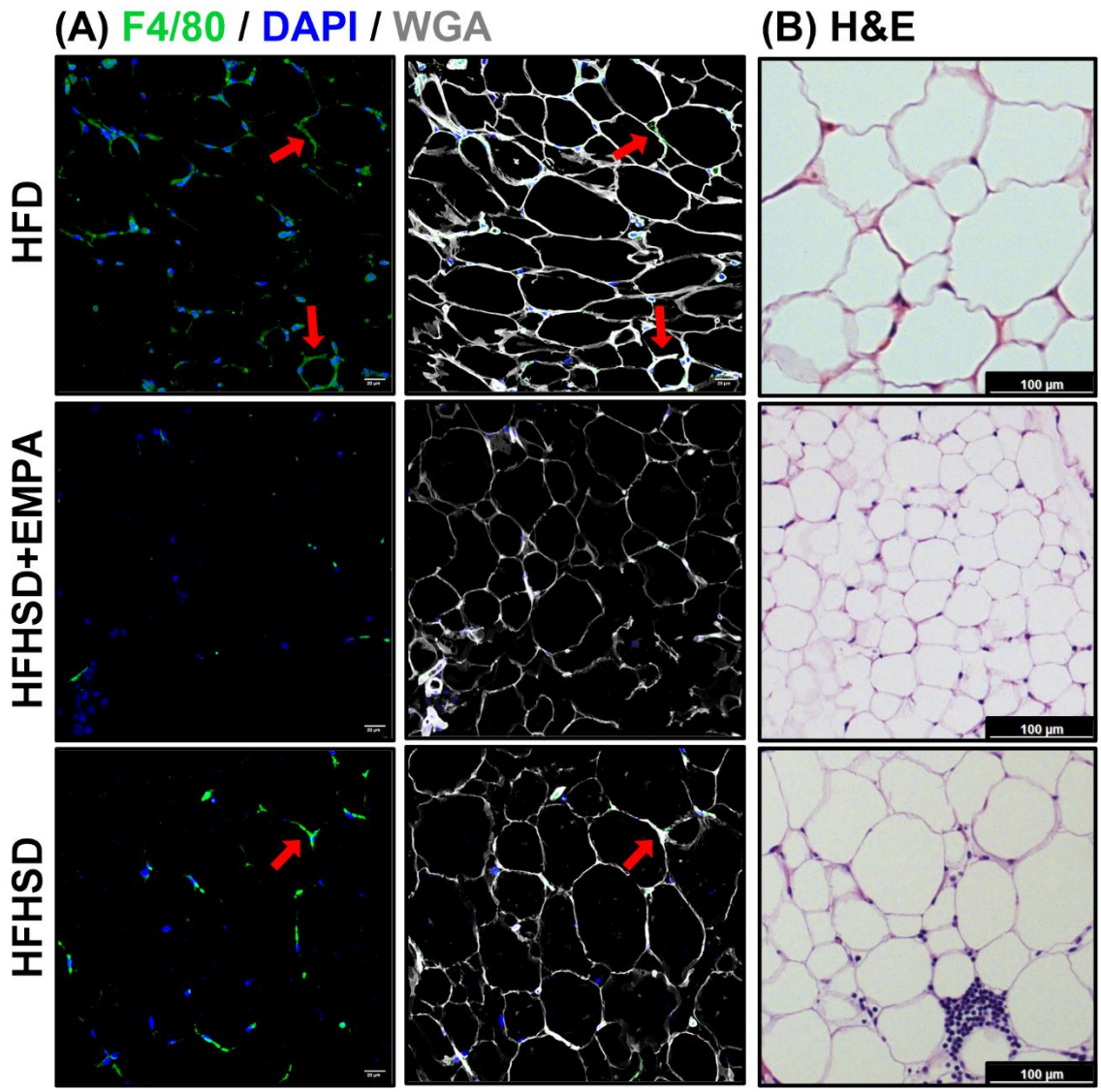

Figure 23 - Epicardial adipose tissue histology. (A) F4/80 (green) and DAPI (blue) staining show increased macrophage infiltration in HFD and HFHSD mice, which is reduced with EMPA treatment (left column). Merged F4/80, DAPI, and WGA (white) images highlight crown-like structures of macrophages surrounding adipocytes (red arrows) in HFD and HFHSD conditions (middle column). Scale bar: 20 µm. (B) Hematoxylin and eosin (H&E) staining reveals larger adipocytes in HFD and HFHSD conditions, while EMPA-treatment displays smaller, more uniform adipocytes. Images in (A) and (B) were obtained from different mice within the same experimental groups. Scale bar: 100 µm. WGA, wheat germ agglutinin. All other abbreviations as in **Figure 22**.

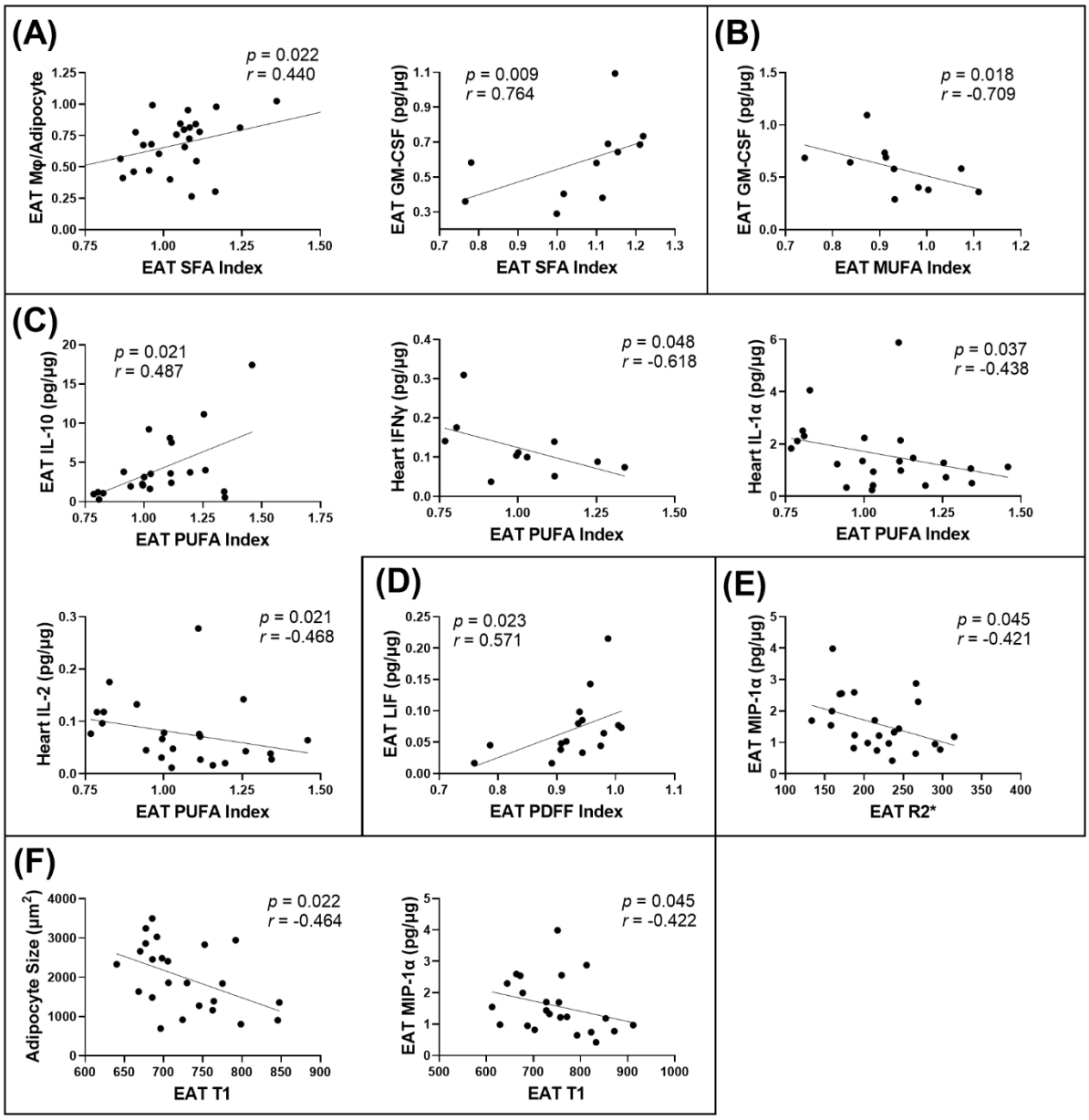

Figure 24 - Relationships between EAT MRI parameters and tissue inflammation markers. Correlations between EAT MRI parameters – (A) SFA index, (B) MUFA index, (C) PUFA index, (D) PDFF index, (E) R_2^*, and (F) T_1 – and tissue measures, including macrophage density (Mφ/adipocyte), adipocyte size (μm²), and cytokine levels (pg/μg total protein). Spearman's *r* and *p*-values are reported for each plot. Abbreviations as in **Figure 18** and **Figure 21**.

2.5 Discussion

This study developed an accelerated method for joint FAC and T_1 mapping of EAT, expanding upon a growing body of research aimed at noninvasively characterizing EAT. By integrating T_1 mapping and FAC, this method provides a more comprehensive assessment of EAT quality, as both adipose tissue FAC and T_1 are altered in chronic metabolic inflammatory states, such as obesity. The approach exploits correlations across multiple contrast dimensions while leveraging golden-angle radial sampling and an HD-PROST-based reconstruction framework to achieve high acceleration rates. To our knowledge, this is the first study to correlate in vivo MRI-derived EAT parameters with ex vivo markers of inflammation, establishing that these MRI parameters are noninvasive biomarkers of proinflammatory EAT.

This method builds upon prior work on MRI parameter mapping of adipose tissues. While several groups have demonstrated in vivo adipose tissue FAC mapping[26,28,29,31,170], joint mapping of longitudinal T_1 relaxation and FAC has yet to be developed for cardiac applications. Preclinical EAT FAC mapping at 7T demonstrated feasibility in mouse models of coronary microvascular disease[31], yet this approach relied on Cartesian sampling, limiting its robustness to motion and requiring longer scan times. The proposed method improves upon these limitations by employing golden-angle radial sampling, which provides increased robustness to motion artifacts and greater incoherence of undersampling artifacts, enabling the application of a high-dimensional low-rank reconstruction to support greater acceleration rates. Joint parameter mapping has been explored for simultaneous quantification of tissue relaxation parameters and fat/water separation in the heart[171–173], though primarily for myocardial T_1 mapping and EAT volume rather than EAT quality characterization[173 171]. Ostenson et al. recently demonstrated the feasibility of joint triglyceride saturation and water T_1 mapping in periclavicular adipose depots at 3T[174], but directly extending

this to preclinical EAT imaging presents challenges due to cardiac and respiratory motion, high heart rates (approximately 600-bpm), and the relatively small size of the EAT depot. Our work addresses these challenges by developing an ECG-gated IR multi-echo sequence with golden-angle rotation through multiple contrast dimensions with a higher-order low rank reconstruction and FCM clustering of TIs.

The accelerated joint FAC and T_1 mapping method reduced scan time from an estimated 2.8 hours (fully sampled, 202 spokes) to approximately 17 minutes (rate-9.6, 21 spokes) while maintaining image quality and parameter mapping accuracy. A fully sampled T_1 map alone would require 17 minutes, and a fully sampled FAC map would require 27 minutes. Even with a rate-2 acceleration, separate acquisitions would still take longer than the simultaneous approach, and at rate-3 acceleration, scan times would be similar but image and parameter map quality would degrade. The joint acquisition leverages redundant structural information across the full set of TE × TI images, enabling more robust denoising during reconstruction. It also improves parameter estimation by incorporating substantially more images into model fitting than would be possible using either TE or TI images alone. Future work could explore alternative acquisition strategies to further improve scan efficiency, such as performing saturation recovery preparation instead of inversion recovery, as saturation recovery eliminates the need for RR pauses.

Phantom validation studies were conducted to assess the accuracy of the method for quantifying FAC and T_1. Due to the long scan times required for fully sampled in vivo acquisitions, direct comparisons between fully sampled and accelerated images were not feasible. Instead, validation was performed in phantoms with simulated ECG signals, allowing fully sampled acquisitions for accurate assessment. Phantom measurements demonstrated strong agreement with reference values obtained from NMR spectroscopy for FAC and standard IR MRI for T_1. Absolute

error between fully sampled maps and rate-9.6 accelerated maps was minimal, demonstrating that high acceleration rates preserved parameter mapping accuracy.

This study identified distinct diet- and EMPA-induced differences in MRI-derived EAT and SAT parameters. Changes in adipose tissue triglyceride composition are influenced by diet, and our method detected expected differences in absolute FAC parameters among mice fed an HFD (high in MUFA) and an HFHSD (high in SFA), validating expected in vivo shifts in adipose tissue composition. Indexing to SAT, which accounts for the propensity to store, mobilize, and endogenously synthesize lipid in different depots under different conditions[76,166], revealed a distinct EMPA-treated phenotype. HFHSD+EMPA mice exhibited a low EAT SFA index and high EAT MUFA and PUFA indexes, consistent with known anti-inflammatory effects of SGLT2i on adipose tissue. In contrast, HFHSD and HFD mice, both prone to developing proinflammatory adipose tissue and metabolic heart disease, had similar indexed values, with high EAT SFA indexes and low EAT MUFA and PUFA indexes. These findings suggest that MRI-derived parameters may serve as modifiable biomarkers for adipose tissue inflammation.

Our findings establish MRI-derived EAT SFA, MUFA, PUFA, and PDFF indexes, along with relaxation parameters T_1 and R_2^*, as noninvasive biomarkers of proinflammatory EAT in metabolic heart disease. The EAT SFA index positively correlated with EAT macrophage infiltration and the proinflammatory cytokine GM-CSF. Macrophages play a central role in adipose tissue inflammation, sustaining chronic inflammation in obesity through alternative polarization, crown-like structure formation, cytokine secretion, and immune cell recruitment [175]. GM-CSF, a potent driver of macrophage differentiation and recruitment, is elevated in inflamed adipose tissue and may contribute to HF, as increased GM-CSF receptor expression has been detected in cardiomyocytes of end-stage HF patients[176,177]. Additionally, the PDFF index was positively

associated with EAT levels of LIF. Although LIF promotes adaptive cardiac remodeling under acute stress, its sustained elevation in chronic conditions is linked to worsening heart failure[178–180]. The correlations between the EAT SFA and PDFF indexes and these markers suggests that a shift toward a greater fatty acid saturation and fat density in the EAT relative to SAT is associated with increased inflammatory signaling and macrophage infiltration, characterizing a proinflammatory EAT phenotype with detrimental cardiovascular effects.

In contrast, higher relative fatty acid unsaturation in the EAT is associated with anti-inflammatory properties. The MUFA index negatively correlated with GM-CSF, while PUFA index positively correlated with the potent anti-inflammatory cytokine IL-10 in the EAT[181,182], and negatively correlated with major proinflammatory cytokines in the heart, including IFN-γ, IL-1α, and IL-2[183–185].

Relaxation parameters, T_1 and R_2^*, serve as additional noninvasive markers of EAT quality. The observed relationship between adipocyte size and T_1 is consistent with previous studies linking T_1 shortening to structural changes in adipose tissue associated with a proinflammatory state[92]. EAT T_1 was also negatively correlated with the proinflammatory cytokine MIP-1α (or CCL3). MIP-1α, a macrophage-secreted chemokine, promotes adipose tissue inflammation, as evidenced by elevated inflammatory markers in obese patients with high MIP-1α and reduced inflammation in MIP-1α-deficient mice. It has also been associated with impaired cardiac function, with higher levels correlating with reduced LV function in HF patients[186,187]. While increased lipid content likely contributes to T_1 shortening, other biological factors such as elevated reactive oxygen species, changes in fatty acid composition, lower temperature, and local hypoxia may also play a role [188]. EAT R_2^* also inversely correlated with MIP-1α. This finding suggests that increases in R_2^* may indicate a healthier EAT phenotype. In fact, higher R_2^* has been identified as a biomarker of

increased iron content in brown adipose tissue, a more metabolically active adipose subtype with beneficial effects on obesity and metabolic inflammation[189].

Taken together, these results indicate that increases in EAT SFA index and PDFF index, coupled with reduced MUFA index, PUFA index, T_1, and R_2^*, characterize a proinflammatory EAT phenotype marked by adipocyte hypertrophy, macrophage infiltration, and local inflammatory signaling in the setting of cardiometabolic dysfunction. These relationships support the use of MRI-based EAT parametric mapping as a tool for identifying modifiable proinflammatory EAT in cardiovascular disease.

2.6 Limitations

Our study has several limitations. First, the imaging protocol was optimized for the measurement of T_1 values for adipose tissue, precluding accurate measurements in other tissues of potential interest such as the myocardium. While not the focus of the study, future work could optimize methods for imaging of both the EAT and myocardium. Another potential limitation is the reliance on assumptions in the signal model. Using a fixed fatty acid chain length for all in vivo measurements may introduce errors if actual chain lengths deviate from this assumption. While accurate for HFHSD-fed mice, it may be less so for others. However, given the small expected physiological variation in chain length, a single model avoids potential bias from different assumptions for each group. Furthermore, while a Look-Locker correction was applied for T_1 estimation, it remains an approximation, and T_1 measurements may be affected by B_1 inhomogeneities, imperfect adiabatic inversion pulses, and deviations in signal relaxation due to repetitive readouts. The proposed method does not differentiate between the T_1 of water and fat. Although this was not a primary focus of the present study, future implementations could work toward enabling independent assessment of fat and water T_1 contributions to EAT inflammation,

with potential to expand this model to include different T_1 values for each fat resonance. Lastly, we used oil phantoms instead of EAT for MRI FAC validation by NMR spectroscopy. As the amount of EAT available from mice for ex vivo studies was limited, we prioritized using this tissue for histology and flow cytometry instead of NMR spectroscopy.

2.7 Conclusions

This study introduces an accelerated MRI approach for joint FAC and T_1 mapping of EAT, offering multiparametric assessment of adipose tissue composition. By integrating golden-angle radial sampling across multiple time dimensions and an iterative higher-order low rank reconstruction, the method achieves substantial scan time reduction while maintaining accuracy, as confirmed by phantom validation and in vivo studies. The studies comparing MRI and tissue properties establish MRI-derived EAT T_1 and R_2^*, and SFA, MUFA, PUFA, and PDFF indexes as noninvasive biomarkers of proinflammatory EAT in metabolic heart disease. These noninvasive biomarkers may be of use in future research seeking to evaluate therapies aimed at treating proinflammatory EAT.

Chapter 3: CMR for the assessment of early and late SGLT2-inhibitor treatment in a mouse model of early stage cardiometabolic HFpEF

3.1 Introduction

Cardiometabolic heart failure with preserved ejection fraction (HFpEF) is the most prevalent form of HFpEF and is marked by significant morbidity and mortality. While highly effective therapies are still lacking, moderately effective treatments such as sodium glucose co-transporter 2 (SGLT2) inhibitors and glucagon-like peptide-1 receptor agonists (GLP-1RAs) have recently emerged[98,190]. Central to its pathogenesis are excess visceral adipose tissue (VAT) and chronic inflammation, with mouse models showing a critical role of inducible nitric oxide synthase (NOS2, formerly known as iNOS) driving oxidative and nitrosative stress[51,58]. Among visceral fat depots, epicardial adipose tissue (EAT) in particular promotes myocardial inflammation due to its anatomical proximity, shared microcirculation, and potential to infiltrate the myocardium[3]. In obesity, EAT undergoes adipocyte hypertrophy and becomes enriched with proinflammatory saturated fatty acids, initiating an inflammatory cascade marked by cytokine secretion, immune cell recruitment, and proinflammatory macrophage polarization[75,146,191]. Cytokines can be transduced to the myocardium via paracrine and vasocrine pathways, leading to coronary microvascular and diastolic dysfunction—key features of HFpEF. Despite advances in understanding EAT and key inflammatory mediators such as NOS2 in HFpEF, critical gaps remain, such as clarifying the effect that SGLT2 inhibitors have on proinflammatory EAT and macrophage expression of NOS2. Also, new noninvasive cardiac magnetic resonance imaging (CMR) biomarkers to characterize proinflammatory EAT could help elucidate mechanisms of disease progression and therapy.

Anti-diabetic SGLT2 inhibitors are now recommended for the treatment of HFpEF as they reduced HFpEF hospitalizations by 29% over a 26 month period in patients regardless of diabetes status; however, they did not reduce cardiovascular death[98]. Although SGLT2 inhibitors have been shown to reduce EAT volume, suppress adipose tissue inflammation, and improve left ventricular

(LV) diastolic function, their mechanisms of action and therapeutic use in HFpEF are not fully understood[117,151,192]. The effect of SGLT2 inhibition on the coronary microvascular response to adenosine receptor agonism and associated myocardial perfusion reserve (MPR) have yet to be definitively investigated. Moreover, it is unclear whether SGLT2 inhibitors can modulate proinflammatory EAT changes induced by a western diet, such as altered fatty acid composition (FAC), adipocyte hypertrophy, or macrophage infiltration and polarization. Lastly, whether SGLT2 inhibitors can reverse established impairments in MPR, diastolic dysfunction, and EAT inflammation remains unknown.

The purpose of the present study was to use multiparametric CMR and other methods applied to a high-fat high-sucrose diet (HFHSD) mouse model to investigate the effects of SGLT2 inhibition on EAT quantity and quality, macrophages, coronary microvascular dysfunction and diastolic dysfunction. The HFHSD mouse model recapitulates features of early stage cardiometabolic HFpEF including obesity, glucose intolerance, VAT accumulation, oxidative stress, coronary microvascular dysfunction, and diastolic dysfunction[31,53,193]. We considered the case of early treatment, where SGLT2 inhibition is initiated concurrently with the start of the HFHSD, and late treatment, where SGLT2 inhibition is initiated later, after the establishment of coronary microvascular and diastolic dysfunction.

3.2 Methods

3.2.1 Experimental Design

All animal studies were performed in accordance with protocols that conformed to the Declaration of Helsinki as well as the Guide for Care and Use of Laboratory Animals[164] and were approved by the Animal Care and Use Committee at the University of Virginia. All mice were maintained at the University of Virginia Center for Comparative Medicine pathogen-free vivarium facility. Male

mice were used in this study because the time course and degree of EAT accumulation and coronary microvascular and diastolic dysfunction due to an HFHSD have been established[31,53]. Experiments were performed to test the following hypotheses: (1) that early treatment with an SGLT2 inhibitor given at the initiation of an HFHSD reduces EAT accumulation, modifies EAT quality, improves MPR, improves diastolic dysfunction, and reduces $NOS2^+$ M1 macrophages in the EAT and heart, and (2) that late treatment with an SGLT2 inhibitor initiated after 15 weeks of an HFHSD can reverse established EAT accumulation, proinflammatory EAT quality, impaired MPR, impaired diastolic dysfunction, and $NOS2^+$ M1 macrophage accumulation in the heart.

3.2.1.1 Effect of Early SGLT2 Inhibition on Cardiometabolic HFpEF

Two groups of mice were studied: (1) wild-type (WT) male C57BL/6J mice (Jackson Laboratories, strain #000664) fed an HFHSD (40% kcal fat, 40% kcal sucrose; Diet 123727, Research Diets Inc) ($HFHS_{early}$), and (2) WT male C57BL/6J mice (Jackson Laboratories, strain #000664) fed an HFHSD with 30 mg/kg/day of the SGLT2 inhibitor, empagliflozin (EMPA), added to the diet (40% kcal fat, 40% kcal sucrose; Diet 21011406, Research Diets Inc) ($HFHS+EMPA_{early}$). Either diet was initiated at 10 weeks of age and was continued for 18 weeks (**Figure 25A**). Glucose tolerance tests (GTT) were performed 17 weeks post-diet (n = 14-15/group). All mice underwent CMR at 18 weeks post-diet (n = 15/group). After 20 weeks on diet, mice were euthanized and used for either coronary arteriolar reactivity experiments (n = 5/group), histology (n = 8-10/group), or macrophage flow cytometry (n = 8/group).

3.2.1.2 Effect of Late SGLT2 Inhibition on Cardiometabolic HFpEF

Two groups of mice were studied: (1) WT male C57BL/6J mice (Jackson Laboratories, strain #000664) fed an HFHSD where the diet was initiated at 10 weeks of age and continued for 23 weeks ($HFHS_{late}$), and (2) WT male C57BL/6J mice (Jackson Laboratories, strain #000664) fed

an HFHSD diet for 23 weeks, where the diet was initiated at 10 weeks of age and 30 mg/kg/day of EMPA was added to the diet 15 weeks after beginning the HFHSD (HFHS+EMPA$_{late}$), providing a treatment duration of 8 weeks (**Figure 25B**). Prior to treatment initiation, mice underwent GTT and CMR (n = 14/group) at 14 and 15 weeks on HFHSD, respectively, to document the establishment of early stage HFpEF features. Post-treatment GTT was performed at 7 weeks after treatment (22 weeks on HFHSD), and post-treatment CMR was performed 8 weeks after treatment (23 weeks on HFHSD). At 34 weeks of age (24 weeks on HFHSD), mice were euthanized and hearts were harvested for flow cytometry (n = 5/group).

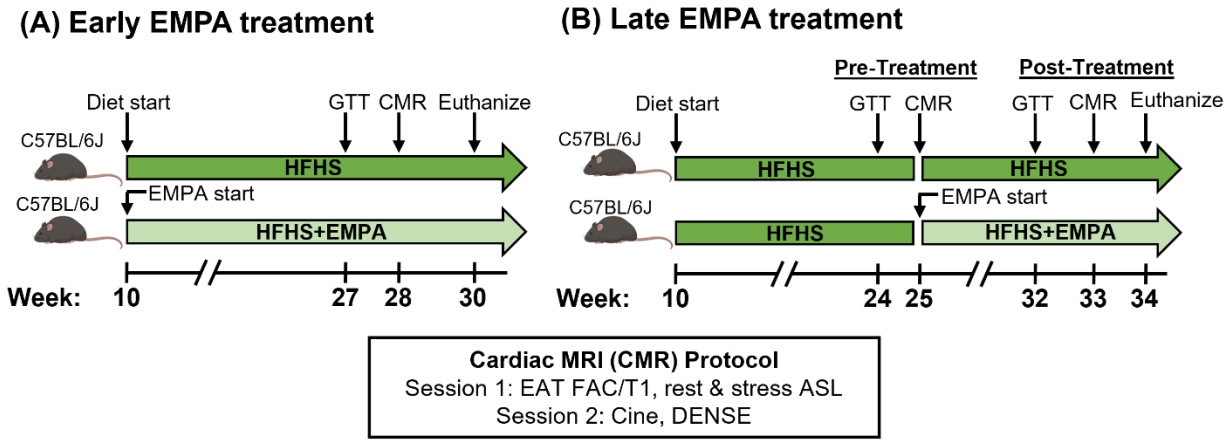

Figure 25 - Experimental design. Timeline for experiments testing (A) early and (B) late SGLT2 inhibition with empagliflozin (EMPA) in mice fed a high-fat high-sucrose (HFHS) diet. GTT, glucose tolerance testing. FAC, fatty acid composition; ASL, arterial spin labeling; DENSE, displacement encoding with stimulated echoes.

3.2.2 CMR Protocol

CMR studies were performed over two sessions separated by 2-3 days. CMR was performed with a 9.4T system (Biospec 94/20, Bruker Biospin, Germany) using a ^{1}H transmit-receive quadrature volume radiofrequency coil with 35 mm inner diameter (Bruker BioSpin GmbH, Germany).

During CMR studies, the electrocardiogram (ECG), body temperature, and respiration were continuously monitored (SA Instruments, Stony Brook, New York, USA). Mice were anesthetized with 1% isoflurane and maintained at a body temperature of 36 ± 0.5°C using circulating warm water.

For all experiments, the CMR protocol included (1) arterial spin labeling (ASL) at rest and with adenosine vasodilation to quantify myocardial blood flow (MBF) and MPR for the assessment of coronary microvascular function[194,195], (2) displacement encoding with stimulated echoes (DENSE) imaging to measure global longitudinal strain and peak diastolic strain rate (PDSR) for the evaluation of LV systolic and diastolic function[140], (3) cine imaging covering the entire LV to measure cardiac structure and function parameters including LV mass, end-diastolic wall thickness (EDWT), end-systolic wall thickness (ESWT), end-diastolic volume (EDV), end-systolic volume (ESV), and ejection fraction (EF), and (4) FAC and T1 mapping to quantify metrics of EAT quality (proton density fat fraction (PDFF), saturated fatty acid fraction (SFA), monounsaturated fatty acid fraction (MUFA), polyunsaturated fatty acid fraction (PUFA), and longitudinal relaxation time, T1) and myocardial PDFF[31,196,197]. Rest and stress ASL, FAC, and T1 mapping were performed at session 1 of CMR, and cine and DENSE imaging were performed at session 2 of CMR. Body weight was recorded for all mice at the beginning of each imaging study.

3.2.2.1 EAT Fatty Acid Composition and T1 Mapping

Joint FAC and T1 mapping was performed on a mid-ventricular short-axis slice using an ECG-triggered inversion recovery radial multi-echo gradient-echo sequence[196]. Imaging parameters included: number of echo times (TEs): 20; TE_1: 1.4 ms; ΔTE = 0.2 ms; number of inversion times (TIs): 30; TI_1: 3.7 ms; ΔTI = RR-interval; flip angle: 15°; slice thickness: 1.0 mm; number of radial

spokes: 21; field of view (FOV): 25 × 25 mm^2; matrix size: 128 × 128; resolution = 0.2 × 0.2 mm^2; total scan time approximately 20 minutes.

3.2.2.2 Cine Imaging

Six to 8 short-axis slices were acquired, covering the LV from base to apex. Imaging parameters included: repetition time (TR): 4.0 ms; TE: 1.35 ms; temporal resolution: 4.0 ms; FOV: 25 × 25 mm^2; matrix size: 128 ×128; flip angle: 15°; number of averages = 3; resolution = 0.2 × 0.2 mm^2; total scan time approximately 2 minutes per slice.

3.2.2.3 Myocardial Perfusion Imaging

At session 1, an intraperitoneal catheter was inserted for delivery of the vasodilator, adenosine (Sigma-Aldrich) (18 μg/min), during imaging. Rest perfusion imaging of a mid-ventricular short-axis slice was then performed using a respiratory-gated ASL method[195]. Thereafter, adenosine was infused intravenously and 10 minutes later ASL was repeated. Imaging parameters for ASL included: TE: 2.5 ms; TR: 10.0 ms; FOV: 25 × 25 mm^2; matrix size: 128 × 128; flip angle: 7°; slice thickness: 1.0 mm; saturation band thickness: 2.5 mm; number of averages: 9; resolution = 0.2 × 0.2 mm^2; total scan time approximately 10 minutes per rest or stress scan.

3.2.2.4 Myocardial Strain Imaging

DENSE strain imaging[140] was performed on a 4-chamber long-axis slice. Imaging parameters included: FOV: 32 x 32 mm^2; matrix size: 128 x 128; slice thickness: 1.0 mm; TR: 7.0 ms; TE: 2.45 ms; number of averages: 4; spatial resolution = 0.25 × 0.25 mm^2; total scan time approximately 14 minutes.

3.2.3 CMR Image analysis

Image analysis was performed using MATLAB 2023a (MathWorks, Natick, MA). CMR data were excluded from analysis if poor-quality ECG and/or respiratory signals led to severe image artifacts.

For MBF quantification, rest and adenosine stress perfusion images were analyzed using methods previously described[195]. MPR was calculated as the ratio of stress perfusion to rest perfusion. Strain analysis of DENSE images was performed using the DENSE analysis tool[141,198]. Global longitudinal strain and peak diastolic strain rate were measured as metrics of systolic and diastolic function, respectively. Cine images were analyzed using Segment version 4.1.0.1 R14284b package. Specifically, the end-diastolic and end-systolic frames were identified, and the endocardial and epicardial contours were manually drawn on these frames for all slices. Using Segment, EDWT, ESWT, EDV, ESV, EF, and LV mass were calculated. Cine images were also used to quantify EAT volume index, defined as EAT volume in microliters divided by the mouse body weight in grams. The EAT was manually segmented at end-diastole for all slices and the combined EAT volume across all slices was calculated as # pixels $\times$ 0.038 mm^3/pixel.

For EAT FAC, PDFF, and T1 quantification, incoherently undersampled images were denoised using a higher-order tensor decomposition method[154]. Parametric mapping was performed using conventional magnetic field mapping and a least-squares fit to a T1-weighted triglyceride multi-resonance signal model for computation of PDFF, SFA, MUFA, PUFA, and T1[29,197,199]. The epicardial and subcutaneous adipose tissue (SAT) depots were manually segmented and the average PDFF, SFA, MUFA, PUFA, and T1 were calculated for each depot. Regions of interest (ROIs) for each depot included pixels with a PDFF > 50%. Additionally, to assess myocardial lipid, the myocardium was manually segmented and the average PDFF was calculated. The mean PDFF, FAC, and T1 values for each depot of each mouse were calculated from ROIs with at least 30 pixels.

3.2.4 Glucose Tolerance Tests

For GTTs, mice were injected intraperitoneally with sterile glucose (8 g/kg body weight) in deionized water after a 16 hour overnight fast. Blood samples were taken from the tail vein before injection to measure the fasting blood glucose, and 10, 30, 60, 90, and 120 minutes after injection of the glucose solution. The area under the curve (AUC) was calculated by trapezoidal approximation to evaluate glucose tolerance[200].

3.2.5 Vascular Reactivity

Mice were euthanized and coronary arterioles were isolated and freed of the surrounding cardiac myocytes. Using an arteriography system (Danish MyoTechnology), the arterioles were cannulated at both ends and pressurized to 40 mm Hg as previously described[201–203]. Arterioles were pre-constricted with 10 μmol/L phenylephrine. Vessel relaxation measurements are reported as a percent dilation of the initial vessel diameter. Cumulative dose responses to endothelial-independent vasodilators – adenosine and the vascular smooth muscle cell (VSMC)-specific dilator sodium nitroprusside (SNP) – were measured as previously described[201–203].

3.2.6 Flow cytometry

Primary infiltrating leukocytes were isolated from cardiac tissue by non-Langendorff perfusion as previously described[204]. Briefly, hearts were sequentially perfused with EDTA buffer, perfusion buffer, and digestion buffer containing collagenase until hearts appeared soft. Hearts were then mechanically dissociated with scissors and pipetted up and down. Cells were washed through a 100 μm cell strainer to create a single cell suspension. Myocytes were isolated by centrifugation at 120 × g for 5 minutes. Supernatants (containing non-myocyte cells) were transferred to clean tubes and pelleted by centrifugation at 300 × g for 5 minutes, then resuspended in 1 mL of FACS buffer (PBS, 2 mM EDTA, and 1% BSA). Splenocytes were isolated by grinding through a 100

μm cell strainer and washing with PBS containing 2 mM EDTA, then treated with ACK Lysis buffer for 5 minutes. EAT was digested with collagenase 2 containing DMEM with gentle shaking at 37°C for 30 minutes. Samples were centrifuged at 700 × g for 5 minutes and stromal vascular fractions (SVF) were collected. All samples were then counted and resuspended at 100 μL per 100,000 cells in PBS. Cells were stained with LIVE/DEAD Yellow (1:1000) (Thermo Scientific L34967) for 30 minutes on ice. Fc-receptors were then blocked for 15 minutes using FcBlock (BioRad – BUF041A). Cells were pelleted by centrifugation (300 × g, 5 minutes) and resuspended in FACS buffer (100 μL per 100,000 cells) and stained with fluorophore-conjugated antibodies (1:100) for 1 hour on ice (**Table 3**).

Table 3 - List of antibodies used for flow cytometry and tissue staining.

Target	Fluorophore	Producer	Catalog Number	Lot Number
CD45 - Flow	eFluor 605	Invitrogen	69-0451-82	2892626
CD68 - Flow	PE	Invitrogen	12-0681-82	2925560
CD163 - Flow	FITC	Invitrogen	11-1631-82	2653045
iNOS (NOS2) - Flow	PerCP-eFluor 710	Invitrogen	46-5920-82	2626673
HMOX1 - Flow	CoraLite 594	Proteintech	CL594-66743	21017731
Live/Dead Yellow - Flow		Invitrogen	L34967A	2775959
Wheat Germ Agglutinin - IHC	Texas Red	Invitrogen	W21405	
F4/80 - IHC		Invitrogen	MF48000	2641995

Cells were washed in FACS (×3) after staining. Intracellular staining was performed after fixation and permeabilization using Fix and Perm Kit (BDBiosciences) per manufacturer instructions. Cells were subsequently stained for intracellular markers using fluorophore-conjugated antibodies

(1:100) for 1 hour on ice. Cells were washed in wash buffer (BDBiosciences) (×3) after staining. Flow cytometry collection and deconvolution was performed on an Aurora Borealis 5 laser Spectral Flow Cytometer. Automatic deconvolution was performed using single stains generated from splenocytes after setting gating on unstained control cells. FMO controls were collected and used to determine gating strategies. Gating was applied identically across all samples. Gating and post-hoc analysis was performed with FCS-Express 7.18. Representative gating for flow cytometry experiments is presented in **Figure 26**.

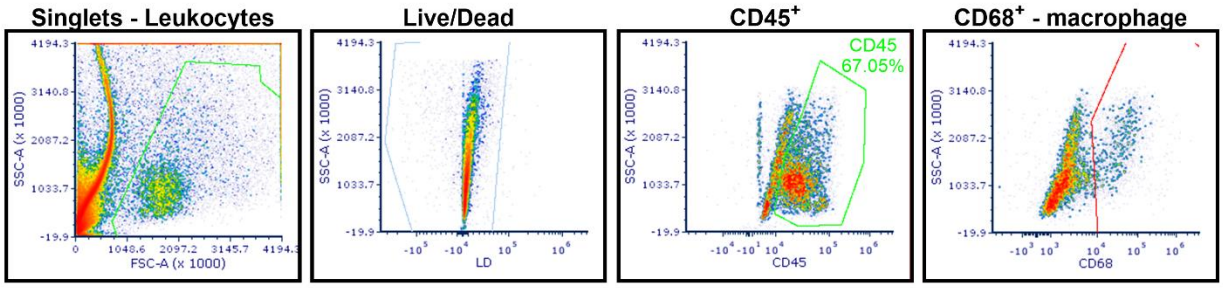

Figure 26 - Gating scheme and representative gates for the identification of $CD68^+$ macrophage cells from primary immune cells isolated from myocardium and epicardial adipose tissue. Cells were gated for live singlet leukocytes and then $CD45^+$ and $CD68^+$ cells were identified.

3.2.7 Histology

Hearts and EAT were collected after CO_2 induced death. Hearts were fixed for 4 hours in NFB prior to being moved to 70% ethanol. Hearts were not arrested prior to harvest. Hearts were paraffin embedded and cryosectioned to 7 μm thickness and mounted. EAT was fixed in 4% PFA in PBS for 7-10 days at 4°C. EAT was paraffin embedded and cryosectioned at 5 μm thickness and mounted. Slides were deparaffinized. Briefly, sections were submerged in xylene (3 minutes), 1:1 xylene:ethanol (3 minutes), 100% ethanol (2×3 minutes), 95% ethanol (3 minutes), 70%

ethanol (3 minutes), and 50% ethanol (3 minutes). Antigen retrieval was performed using citrate-based solution (Vector Laboratories H-330) where slides were submerged in antigen retrieval solution and heated to boiling for 20 minutes, slides were then cooled for 1 hour at room temperature. Tissue sections were then blocked for 1 hour in antibody blocking buffer (FGS, donkey serum) at room temperature. Antibody blocking buffer was removed and replaced with antibody blocking buffer containing primary antibody overnight at 4°C. Sections were then washed (PBS+FGS+Tween for 5 minutes, 2× PBS 5 minutes) and incubated in antibody blocking buffer containing secondary antibody (1:100) for 1 hour at room temperature protected from light. Sections were washed (3× PBS) and counterstained with DAPI (Thermo Fisher Scientific D3571) before mounting. Sections were imaged on an Olympus Fluoview 1000 and are representative images of composite z-stacks. Analysis (thresholding and manual counting) was performed in ImageJ.

3.2.8 Statistics

All data are presented as mean ± standard error of the mean. Statistical analyses were performed using GraphPad Prism version 10.4.0. Variance was assessed using an F-test, and normality was tested with the Shapiro-Wilk test. A p-value < 0.05 was considered statistically significant.

For the study investigating early EMPA treatment, a repeated measures (RM) two-way analysis of variance (ANOVA) with Šidák's multiple comparisons test was used to evaluate differences in blood glucose levels and vascular reactivity between groups ($HFHS_{early}$ vs $HFHS+EMPA_{early}$) at each time point and vasodilator dose, respectively. Flow cytometry data were analyzed using the Mann-Whitney test. For all other comparisons, normality was confirmed, and a two-tailed Student's *t*-test was applied. If significant variance differences were detected, a *t*-test with Welch's correction was used.

An RM two-way ANOVA with Šidák's multiple comparisons test was used to detect differences between groups ($HFHS_{late}$ vs $HFHS+EMPA_{late}$) and between pre- and post-treatment time points.

3.3 Results

3.3.1 Empagliflozin Applied at the Initiation of HFHSD Improves Key Features of Early Stage Cardiometabolic HFpEF

3.3.1.1 Early Empagliflozin Treatment Reduces Obesity and Prevents Glucose Intolerance

To determine the impact of early intervention with EMPA on mice fed an HFHSD, markers of cardiometabolic syndrome were assessed including body weight and glucose tolerance. After 18 weeks on the diet, $HFHS+EMPA_{early}$ mice weighed significantly less than $HFHS_{early}$ controls (41.20 ± 0.88 g vs 44.67 ± 1.07 g, $p = 0.019$) (**Figure 27A**). Glucose tolerance tests and corresponding AUC measurements (**Figure 27B**) demonstrated that EMPA significantly reduced the severity of glucose intolerance after 18 weeks of HFHSD (AUC: $(43.46 \pm 1.69) \times 10^3$ min·mg/dL vs $(55.84 \pm 1.86) \times 10^3$ min·mg/dL, $p < 0.0001$).

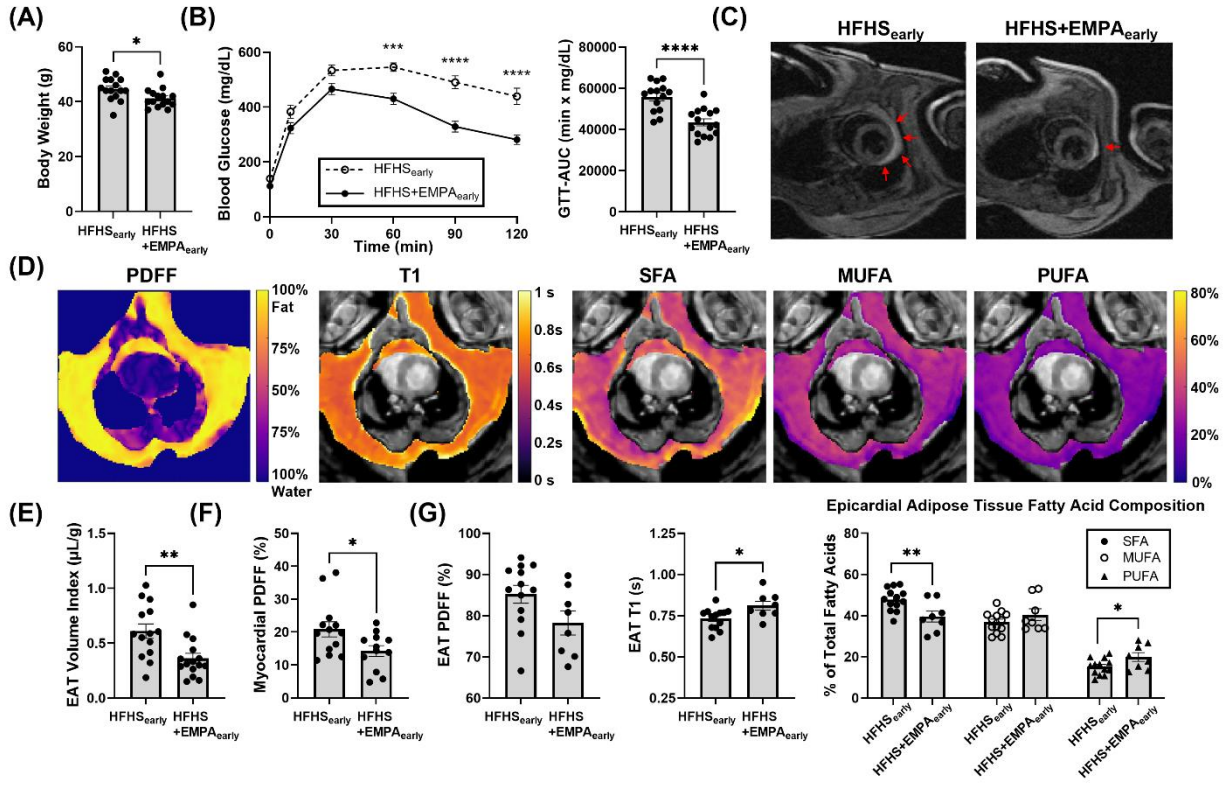

Figure 27 - Effect of early EMPA treatment on body weight, GTT, myocardial PDFF, and EAT quantity and quality measurements. (A) Body weight in grams for $HFHS_{early}$ (n=15) and $HFHS+EMPA_{early}$ (n=15) mice after 18 weeks of diet. (B) Average glucose tolerance curves and corresponding AUC values for $HFHS_{early}$ (n=14) and $HFHS+EMPA_{early}$ (n=15) mice after 17 weeks of diet. (C) Short-axis black-blood cine images at end-diastole of $HFHS_{early}$ and $HFHS+EMPA_{early}$ mice after 18 weeks of diet showing greater EAT volume (red arrows) in $HFHS_{early}$ mice compared to $HFHS+EMPA_{early}$ mice. (D) Example PDFF, T1, SFA, MUFA, and PUFA maps overlayed on SAT and EAT of a mouse after 18 weeks of an $HFHS_{early}$ diet. (E) EAT volume index ($HFHS_{early}$: n = 14, $HFHS+EMPA_{early}$: n = 15), (F) myocardial PDFF ($HFHS_{early}$: n = 13, $HFHS+EMPA_{early}$: n = 12), and (G) EAT PDFF, T1, and FAC (SFA/MUFA/PUFA) ($HFHS_{early}$: n = 13, $HFHS+EMPA_{early}$: n = 8) measurements in $HFHS_{early}$ and $HFHS+EMPA_{early}$ mice after 18 weeks of diet. Data are shown as mean ± SEM and compared using a two-tailed Student's *t*-test.*P<0.05 and **P <0.01 for indicated groups. GTT, glucose tolerance testing; PDFF, proton density fat fraction; SFA, saturated fatty acid fraction; MUFA, monounsaturated fatty acid fraction; PUFA, polyunsaturated fatty acid fraction, EAT, epicardial adipose tissue. All other abbreviations as in **Figure 25**.

3.3.1.2 Early Empagliflozin Treatment Reduces EAT Accumulation

Representative mid-ventricular short-axis end-diastolic images demonstrate lower EAT volume in HFHS+EMPA$_{early}$ mice compared to HFHS$_{early}$ mice (**Figure 27C**). CMR showed a 40.8% reduction in EAT volume index in HFHS+EMPA$_{early}$ mice compared to HFHS$_{early}$ controls (0.36 ± 0.05 µL/g vs 0.61 ± 0.07 µL/g, p = 0.0043) (**Figure 27E**).

3.3.1.3 Early Empagliflozin Treatment Modifies the Myocardial PDFF and the FAC, PDFF, and T1 of EAT but Not SAT

To assess the effect of EMPA treatment on preventing myocardial fat accumulation and on biomarkers of proinflammatory EAT, we used CMR to quantify myocardial PDFF and EAT FAC, T1, and PDFF. Example parametric maps overlayed on the EAT and SAT of a mouse fed an HFHSD for 18 weeks are shown in **Figure 27D**. Myocardial PDFF values were lower in the HFHS+EMPA$_{early}$ mice compared to HFHS$_{early}$ controls (14.26 ± 1.65% vs 20.85 ± 2.31%, p = 0.032) (**Figure 27F**). CMR also demonstrated significant EAT quality changes in HFHS+EMPA$_{early}$ mice compared to HFHS$_{early}$ controls, including a lower EAT SFA (39.59 ± 2.64% vs 47.90 ± 1.50%, p = 0.008) and a higher EAT PUFA (19.95 ± 2.14% vs 15.23 ± 1.07%, p = 0.041) (**Figure 27G**). There was a trend towards a lower EAT PDFF (78.24 ± 2.92% vs 85.23 ± 2.17%, p = 0.066) and EAT T1 was significantly longer (0.812 ± 0.028 s vs 0.733 ± 0.017 s, p = 0.020) in HFHS+EMPA$_{early}$ mice compared to controls. For comparison, we quantified the FAC, PDFF, and T1 of SAT from the HFHS+EMPA$_{early}$ and HFHS$_{early}$ mice. SAT metrics (SFA/MUFA/PUFA, PDFF, and T1) showed no differences between groups (**Figure 28**). These findings show the potential of early EMPA treatment to improve EAT quality by reducing proinflammatory SFA, increasing anti-inflammatory PUFA, prolonging T1, and preventing myocardial lipid accumulation.

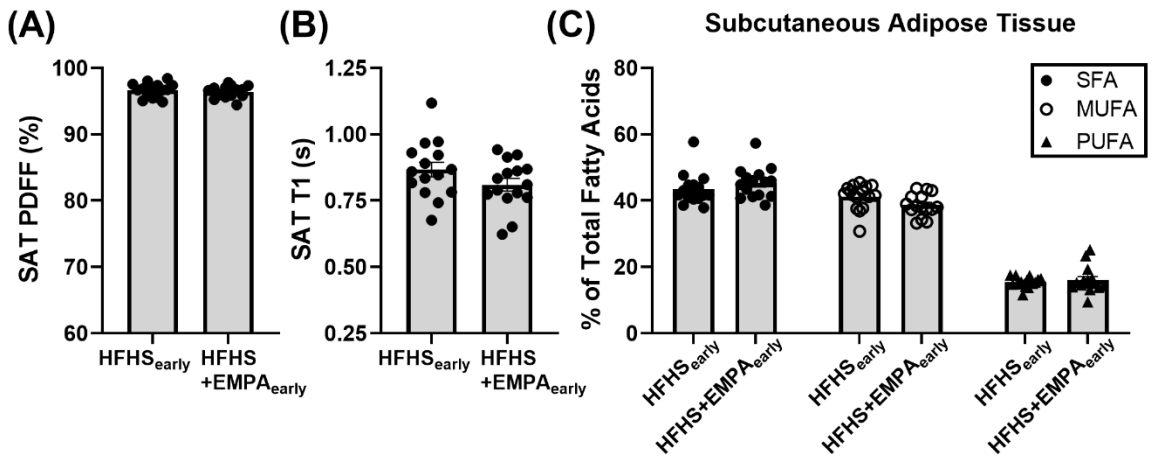

Figure 28 - SAT (A) PDFF, (B) T1, and (C) fatty acid composition (SFA/MUFA/PUFA) in mice (n=15/group) fed an HFHS or HFHS+EMPA for 18 weeks. Data are shown as mean ± SEM. All other abbreviations as in **Figure 25** and **Figure 27**.

3.3.1.4 Early Empagliflozin Treatment Prevents HFHSD-Induced Coronary Microvascular Dysfunction

To evaluate coronary microvascular function, we conducted rest and adenosine-induced ASL myocardial perfusion imaging in HFHS+EMPA$_{early}$ and HFHS$_{early}$ control mice. Example rest and adenosine-stress myocardial perfusion maps are shown in **Figure 29A**. Rest MBF was similar between groups (**Figure 29B**). HFHS+EMPA$_{early}$ mice had significantly higher adenosine-induced stress MBF compared to controls (9.91 ± 0.60 mL/g/min vs 7.72 ± 0.76 mL/g/min, p = 0.031), resulting in a higher MPR (2.00 ± 0.14 vs 1.37 ± 0.12, p = 0.0039) (Figure 29C-D).

To confirm the in vivo CMR perfusion results, we performed ex vivo vasoreactivity testing of isolated coronary arterioles in response to adenosine and SNP. The cumulative dose-response

curves to adenosine ($p < 0.0001$) and SNP ($p < 0.05$) show significant impairment in dilatory capacity for $HFHS_{early}$ mice that is prevented with early EMPA treatment **Figure 29E-F**).

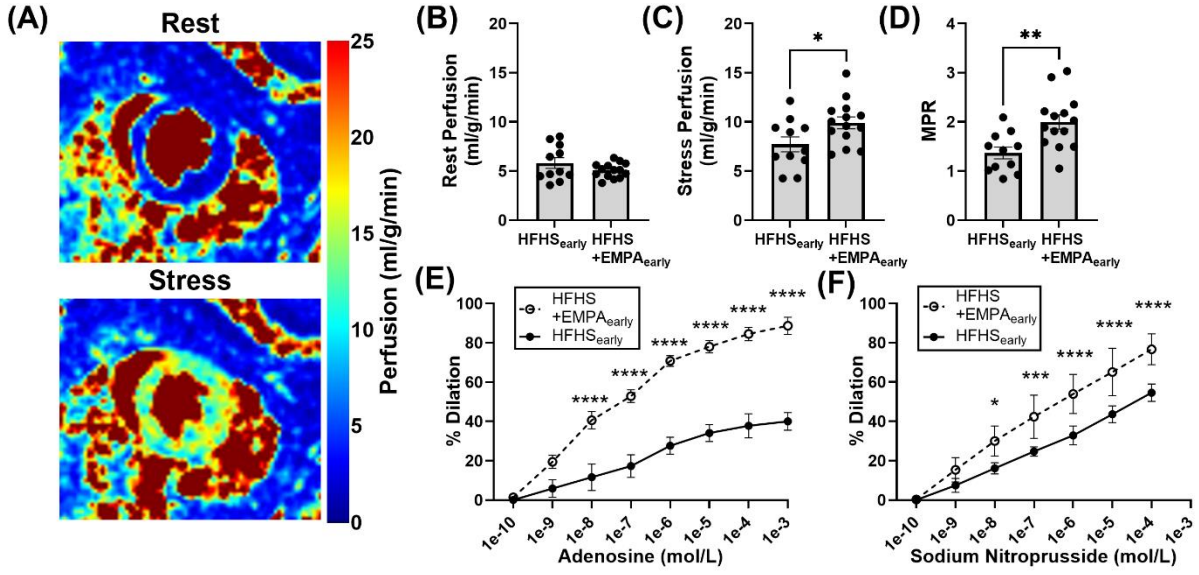

Figure 29 - Effect of early EMPA treatment on myocardial perfusion, MPR, and coronary arteriole vasoreactivity. (A) Example myocardial perfusion maps acquired at rest and during adenosine-induced stress in a mid-ventricular short-axis slice of an $HFHS+EMPA_{early}$ mouse. (B) Rest perfusion, (C) stress perfusion, and (D) MPR measurements for $HFHS_{early}$ (n=11) and $HFHS+EMPA_{early}$ (n=14) mice after 18 weeks of diet. Cumulative arteriolar dose-response curves to (E) adenosine and (F) sodium nitroprusside in $HFHS_{early}$ (n=5) and $HFHS+EMPA_{early}$ mice (n=5) after 20 weeks of diet. Dose-response curves are shown as mean ± SD and compared using an RM two-way ANOVA with Šidák's multiple comparisons test. All other data are shown as mean ± SEM and compared using a two-tailed Student's t-test.*P<0.05, **P <0.01, ***P<0.001, ****P<0.0001 for indicated groups. MPR, myocardial perfusion reserve. All other abbreviations as in **Figure 25**.

3.3.1.5 Early Empagliflozin Treatment Prevents HFHSD-Induced Diastolic Dysfunction, and Provides Lower LV Mass and Diastolic Wall Thickness and Higher EF

We evaluated the effect of EMPA treatment on systolic and diastolic cardiac function using DENSE CMR. There was a trend toward improved peak global longitudinal end-systolic strain in the HFHS+EMPA$_{early}$ mice compared to controls, though it was not significant (**Figure 30B**, representative curves **Figure 30A**). The diastolic strain rate was higher in the HFHS+EMPA$_{early}$ mice compared to controls (3.25 ± 0.23 s^{-1} vs 1.96 ± 0.34 s^{-1}, $p = 0.0038$) (**Figure 30C**), indicating better diastolic function.

Cine imaging showed that HFHS+EMPA$_{early}$ and HFHS$_{early}$ mice had similar EDV, ESV, and ESWT (**Figure 30D**). LV mass was lower in HFHS+EMPA$_{early}$ mice compared to HFHS$_{early}$ mice (82.84 ± 2.39 mg vs 88.64 ± 1.25 mg, $p = 0.043$) (**Figure 30D**). EDWT was lower in HFHS+EMPA$_{early}$ mice compared to controls (0.88 ± 0.02 mm vs 0.95 ± 0.02 mm, $p = 0.026$) (**Figure 30D**). HFHS+EMPA$_{early}$ mice had a higher EF compared to HFHS$_{early}$ mice (72.42 ± 1.85 % vs 64.90 ± 2.07 %, $p = 0.011$), although both groups maintained a preserved EF (>50%) (**Figure 30D**).

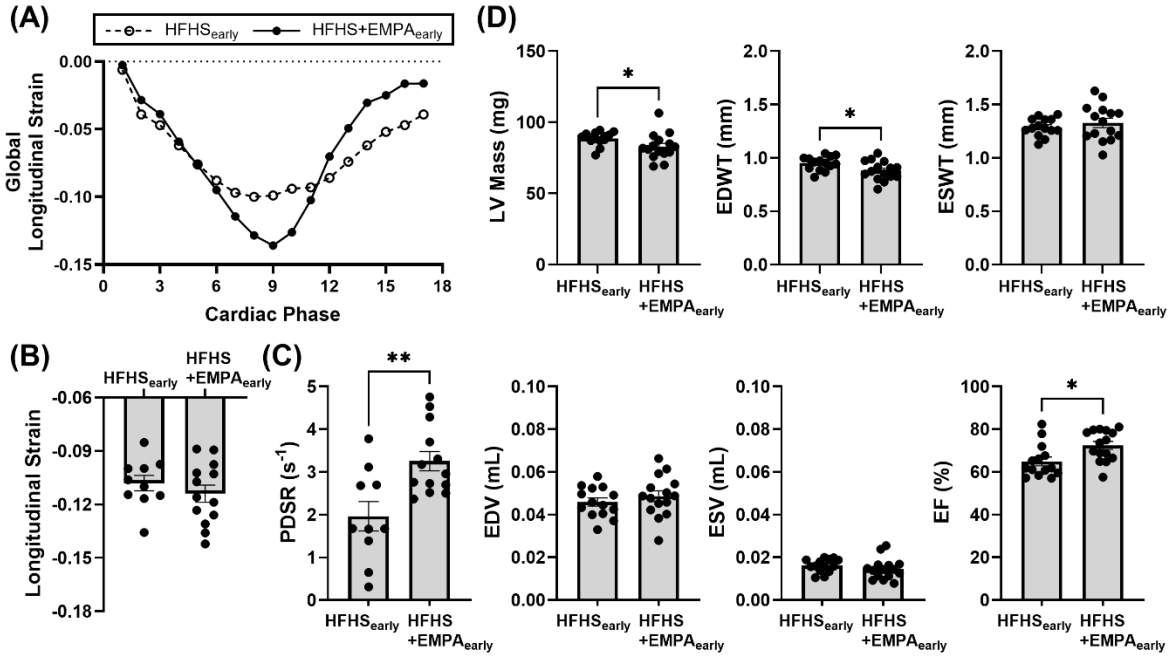

Figure 30 - Effect of early EMPA treatment on systolic strain, diastolic strain rate, and LV structure and function. (A) Example global longitudinal strain curves in an HFHS$_{early}$ and HFHS+EMPA$_{early}$ mouse after 18 weeks of diet showing improvements in diastolic function with EMPA. (B) Global longitudinal strain and (C) PDSR measurements in HFHS$_{early}$ (n=10) and HFHS+EMPA$_{early}$ (n=13) mice after 18 weeks of diet. (D) Cine-derived cardiac structure and function parameters including LV mass, EDWT, ESWT, EDV, ESV, and EF in HFHS$_{early}$ (n=14) and HFHS+EMPA$_{early}$ (n=15) mice after 18 weeks of diet. Data are shown as mean ± SEM and compared using a two-tailed Student's t-test.*P<0.05 and **P <0.01 for indicated groups. PDSR, peak diastolic strain rate; LV, left ventricular; EDWT, end-diastolic wall thickness; ESWT, end-systolic wall thickness; EDV, end-diastolic volume; ESV, end-systolic volume; EF, ejection fraction. All other abbreviations as in **Figure 25**.

3.3.1.6 Early Empagliflozin Treatment Reduces Myocyte and Adipocyte Hypertrophy

To evaluate the impact of early EMPA treatment on cardiomyocyte size and adipocyte hypertrophy as indicators of cardiac hypertrophy and proinflammatory EAT quality in HFpEF, respectively, we analyzed WGA-stained sections of heart tissue and H&E-stained sections of EAT from HFHS+EMPA$_{early}$ and HFHS$_{early}$ mice. Representative histological sections of myocardial tissue

(**Figure 31A**) showed that HFHS+EMPA$_{early}$ mice exhibited reduced cardiomyocyte hypertrophy compared to HFHS$_{early}$ controls, as indicated by smaller mean cardiomyocyte cross-sectional area (263.1 ± 17.77 μm^2 vs 314.1 ± 15.46 μm^2, p = 0.044) (**Figure 31B**). Representative histological sections of EAT (Figure 31E) showed that HFHS+EMPA$_{early}$ mice exhibited reduced adipocyte hypertrophy compared to HFHS$_{early}$ controls, as indicated by smaller mean adipocyte area (1,031.6 ± 123.7 μm^2 vs 2,529.9 ± 160.8 μm^2, p < 0.0001) (**Figure 31F**). These findings align with CMR data showing reduced proinflammatory EAT and cine-derived LV mass and wall thickness, further highlighting the ability of early EMPA treatment to mitigate pathological changes in both EAT and myocardial tissue.

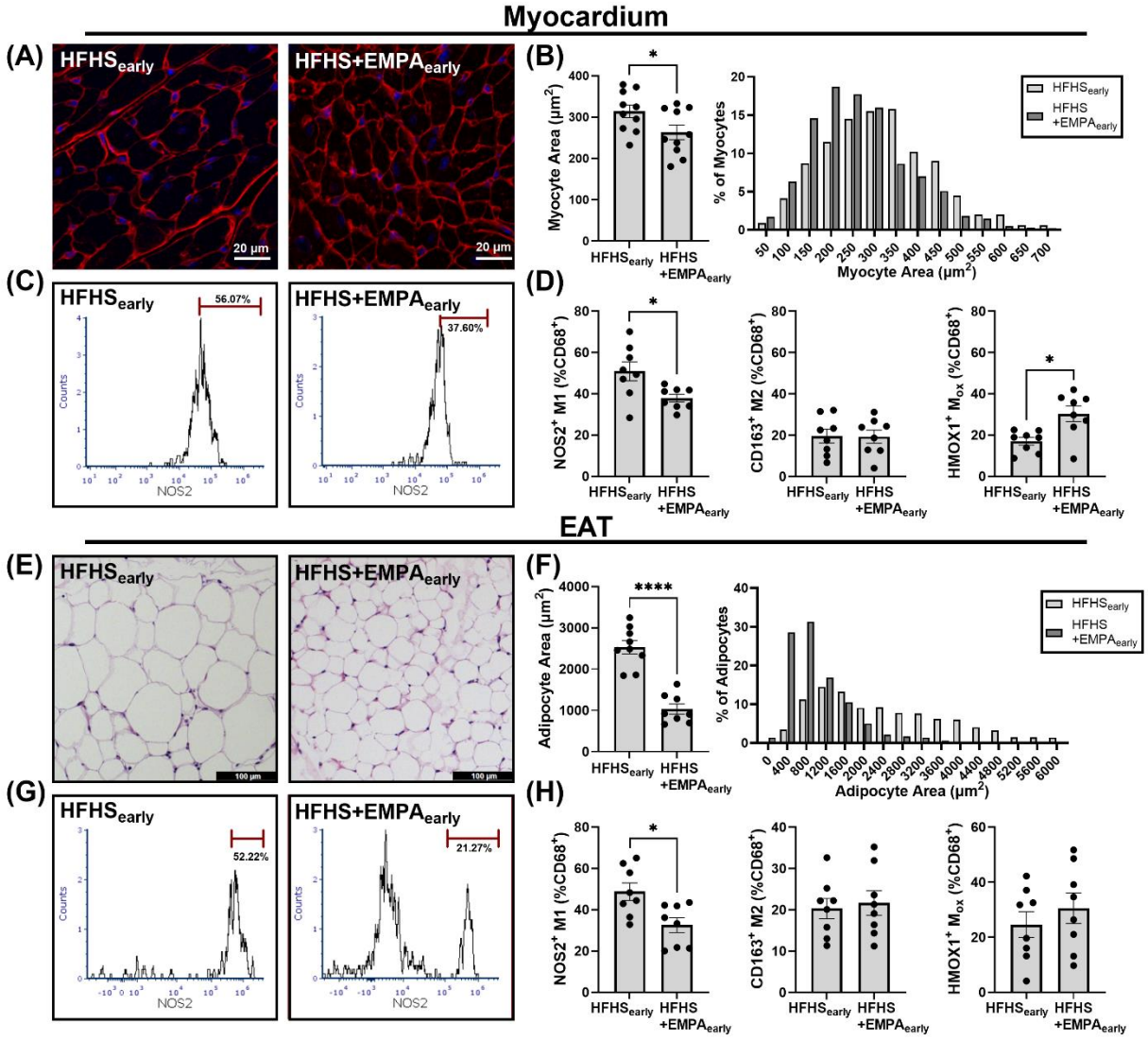

Figure 31 - Effect of early EMPA treatment on cardiomyocyte and EAT adipocyte hypertrophy and macrophage polarization. (A) WGA (red) staining of cardiac myocytes and (B) quantification and distribution of myocyte size in HFHS$_{early}$ (n=10) and HFHS+EMPA$_{early}$ (n=10) mice after 20 weeks of diet. (C) Flow cytometry histograms depicting higher levels of NOS2$^+$ macrophages isolated from the hearts of mice fed an HFHS$_{early}$ or HFHS+EMPA$_{early}$ for 20 weeks. (D) Flow cytometry analysis of NOS2$^+$ cells, CD163$^+$ cells, and HMOX1$^+$ cells as a percentage of CD68$^+$ cells isolated from the hearts of mice fed an HFHS (n=8) or HFHS+EMPA (n=8) for 20 weeks. (E) H&E staining of EAT and (F) quantification and distribution of adipocyte size in HFHS$_{early}$ (n=9) and HFHS+EMPA$_{early}$ mice (n=8) after 20 weeks of diet. (G) Flow cytometry histograms depicting higher levels of NOS2$^+$

macrophages isolated from the EAT of mice fed an HFHS or HFHS+EMPA for 20 weeks. (H) Flow cytometry analysis of $NOS2^+$ cells, $CD163^+$ cells, and $HMOX1^+$ cells as a percentage of $CD68^+$ cells isolated from the EAT of mice fed an HFHS (n=8) or HFHS+EMPA (n=8) for 20 weeks. Data are shown as mean ± SEM. Flow cytometry data are compared using Mann-Whitney test and histological data are compared using a Student's t-test. $P<0.05$ and ****$P<0.0001$ for indicated groups. NOS2, inducible nitric oxide synthase. All other abbreviations as in **Figure 25**.

3.3.1.7 Early Empagliflozin Treatment Reduces EAT Macrophage Infiltration, and Shifts Heart and EAT Macrophage Polarization Toward a Less Proinflammatory State

To investigate the relationship between CMR findings, early EMPA treatment, and shifts in macrophage infiltration and polarization, we performed histopathological analysis of $F4/80^+$ macrophages, a pan macrophage marker, in the EAT. Histopathological analysis revealed a significantly lower number of macrophages ($F4/80^+$ positive puncta) in the EAT of $HFHS+EMPA_{early}$ mice compared to $HFHS_{early}$ mice (**Figure 32**).

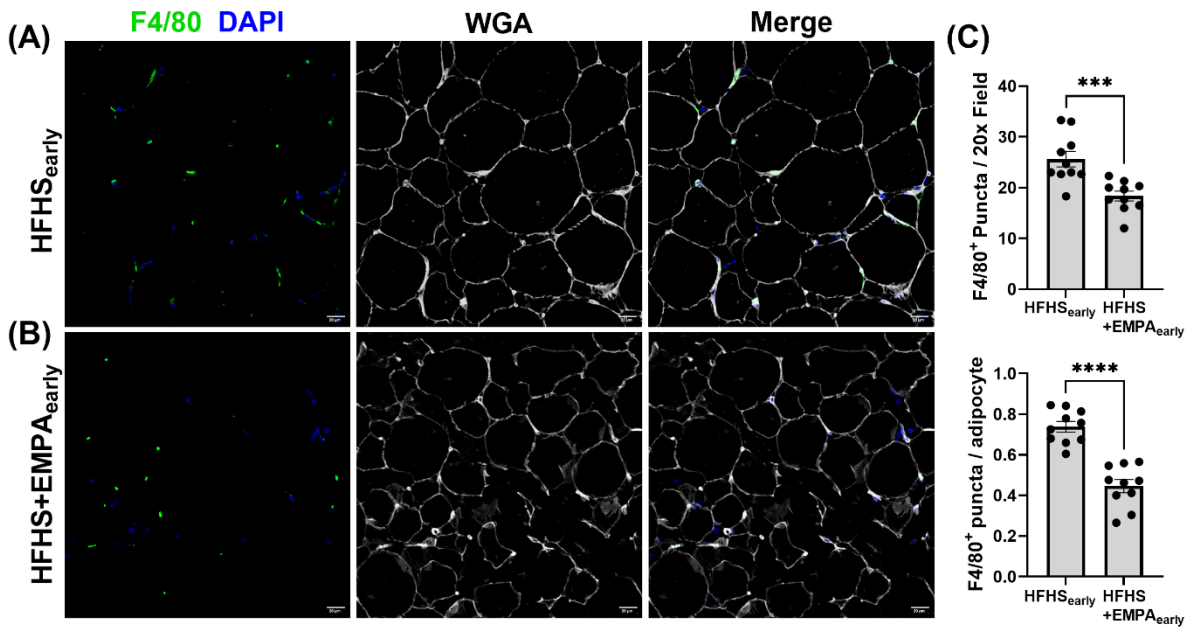

Figure 32 - Effect of early EMPA treatment on EAT macrophage infiltration. Images of EAT from a mouse fed an (A) $HFHS_{early}$ or (B) $HFHS+EMPA_{early}$ for 18 weeks stained with DAPI (blue), F4/80 (green) for macrophage identification, and WGA (white) for adipocyte cell membrane identification. (C) Quantified $F4/80^+$ puncta per 20X field and per adipocyte show reduced macrophage infiltration with EMPA (n=10/group). Data are shown as mean ± SEM and compared using a Student's t-test. WGA, wheat germ agglutinin. All other abbreviations as in **Figure 25**.

To quantify inflammatory infiltrates, flow cytometry of select macrophage populations ($CD68^+$) in the hearts and EAT of $HFHS+EMPA_{early}$ and $HFHS_{early}$ mice was performed. Analysis revealed a significantly lower percentage of $NOS2^+$ (M1 – proinflammatory) macrophages in $HFHS+EMPA_{early}$ mice in both the heart (37.87 ± 1.85 % vs 50.81 ± 4.57 %, p = 0.038) (Figure 31C-D) and EAT (32.50 ± 3.57 % vs 48.79 ± 4.21 %, p = 0.015) (Figure 31G-H) compared to $HFHS_{early}$ controls. Meanwhile, no significant differences were observed in $CD163^+$ (M2 – proresolving/anti-inflammatory) macrophage levels in the hearts (**Figure 31D**) or EAT (Figure 31H) between the two groups. Interestingly, in the hearts of $HFHS+EMPA_{early}$ mice we identified

a higher population of $HMOX1^+$ (Mox) macrophage levels compared to $HFHS_{early}$ mice (30.29 ± 3.79 % vs 16.94 ± 1.84 %, p = 0.010) (**Figure 31D**). Overall, lower macrophage levels combined with a shift to a less inflammatory and more antioxidant macrophage population in the heart and EAT highlights the anti-inflammatory benefits of early EMPA treatment.

3.3.2 Empagliflozin Applied After 15 weeks of HFHSD Halts Weight Gain, Worsening Glucose Intolerance, and EAT Accumulation, but Does Not Improve Biomarkers of EAT Quality, M1 Macrophage Polarization, Impaired Adenosine MPR, or Worsening Diastolic Dysfunction

3.3.2.1 Late Empagliflozin Treatment Halts Weight Gain and Worsening Glucose Intolerance

Given that early EMPA treatment was effective for preventing HFHSD induced cardiac dysfunction measures, we next investigated whether EMPA treatment could reverse impaired MPR and diastolic dysfunction after they have been established by a prolonged HFHSD applied without treatment. Before treatment, after 15 weeks on an HFHSD, both groups had similar weight gain and comparable levels of glucose intolerance (**Figure 33A-B**). After treatment, at 23 weeks on an HFHSD, $HFHS_{late}$ mice exhibited significantly greater weight gain compared to $HFHS+EMPA_{late}$ mice (48.00 ± 0.87 g vs 43.25 ± 1.60 g, p = 0.023) and greater glucose intolerance (AUC: (53.52 ± 2.85) × 10^3 min·mg/dL vs (42.57 ± 1.78) × 10^3 min·mg/dL, p = 0.0007).

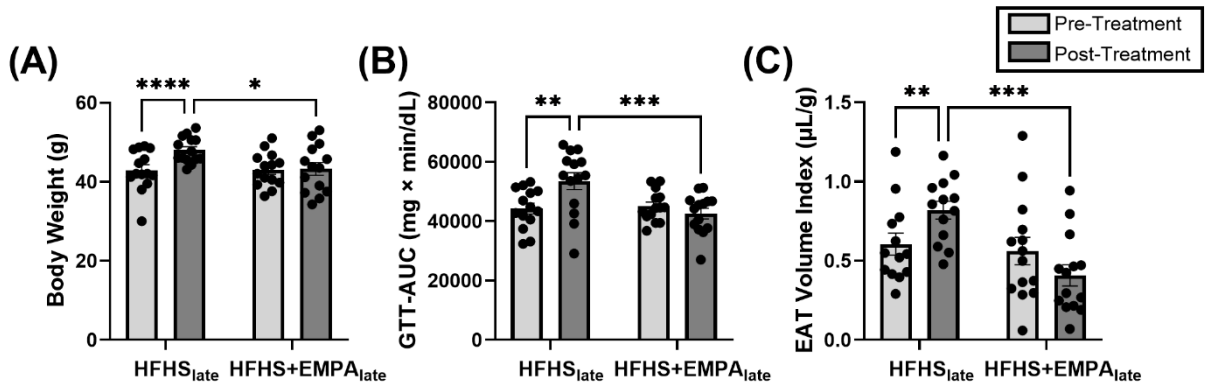

Figure 33- Effect of late EMPA treatment on body weight, GTT, and EAT quantity. (A) Body weight in grams for $HFHS_{late}$ or $HFHS+EMPA_{late}$ mice (n=14/group) after 15 weeks on HFHS diet (pre-treatment) followed by an additional 8 weeks of HFHS or HFHS+EMPA diet (post-treatment). (B) AUC values derived from GTT curves for $HFHS_{late}$ and $HFHS+EMPA_{late}$ mice (n=14/group) pre- and post-treatment. (C) EAT volume index ($HFHS_{late}$: n=13, $HFHS+EMPA_{late}$: n=14) for $HFHS_{late}$ and $HFHS+EMPA_{late}$ mice pre- and post-treatment. Data are shown as mean ± SEM and compared using an RM two-way ANOVA with Šidák's multiple comparisons test.*P<0.05,**P <0.01, ***P <0.001, and ****P <0.0001 for indicated groups. All other abbreviations as in **Figure 25** and **Figure 27**.

3.3.2.2 Late Empagliflozin Treatment Reverses EAT Accumulation

Both groups had similar EAT volume index before treatment at 15 weeks on HFHSD (**Figure 33C**). After treatment, at 23 weeks on an HFHSD, EAT volume index was lower in the $HFHS+EMPA_{late}$ mice compared to $HFHS_{late}$ control mice (0.41 ± 0.07 µL/g vs 0.82 ± 0.06 µL/g, p = 0.0003). In $HFHS+EMPA_{late}$ mice, post-treatment EAT volume index trended lower than pre-treatment, while EAT volume index in $HFHS_{late}$ mice significantly increased from 15 to 23 weeks on the HFHSD (0.61 ± 0.07 µL/g vs 0.82 ± 0.06 µL/g, p = 0.009).

3.3.2.3 Late Empagliflozin Treatment Does Not Improve Myocardial PDFF, or the FAC, PDFF, and T1 of EAT

EAT CMR biomarkers (PDFF, T1, SFA, MUFA, PUFA) were similar between HFHS+EMPA$_{late}$ and HFHS$_{late}$ mice both before and after treatment (**Figure 34A-C**). Similarly, myocardial PDFF was similar between HFHS+EMPA$_{late}$ and HFHS$_{late}$ mice at 15 and 23 weeks on HFHSD (**Figure 34D**). Both groups showed an increase in EAT SFA and a decrease in MUFA from 15 to 23 weeks on HFHSD. These results indicate that EMPA reduced EAT volume but did not improve EAT quality or myocardial fat.

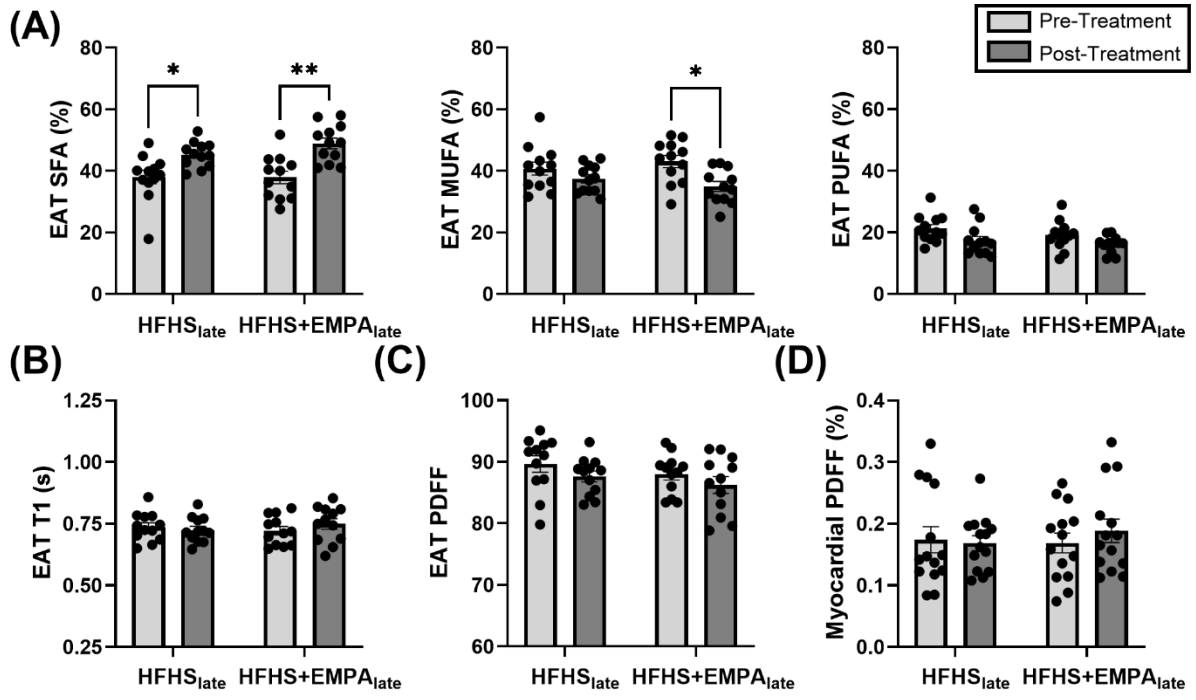

Figure 34 - Effect of late EMPA treatment EAT quality and myocardial PDFF. EAT (A) SFA, MUFA, and PUFA, (B) T1, and (C) PDFF for HFHS$_{late}$ and HFHS+EMPA$_{late}$ mice (n=12/group) after 15 weeks on HFHS diet (pre-treatment) followed by an additional 8 weeks of HFHS or HFHS+EMPA diet (post-treatment). (D) Myocardial PDFF for HFHS$_{late}$ and HFHS+EMPA$_{late}$ mice (n=14/group) pre- and post-treatment. Data are shown as mean ± SEM

and compared using an RM two-way ANOVA with Šidák's multiple comparisons test.*P<0.05 and **P <0.01 for indicated groups. All other abbreviations as in **Figure 25** and **Figure 27**.

3.3.2.4 Late Empagliflozin Treatment Does Not Reverse Impaired Coronary Microvascular Dysfunction

MPR at 15 weeks of HFHSD for HFHS+EMPA$_{late}$ and HFHS$_{late}$ mice was 1.53 and 1.49, respectively, indicating impaired myocardial perfusion as our group has previously shown that healthy SCD-fed mice display MPR values greater than 2[53]. MPR was comparable between the groups at 15 and 23 weeks of HFHSD and remained unchanged for both groups from 15 to 23 weeks on HFHSD (**Figure 35A**).

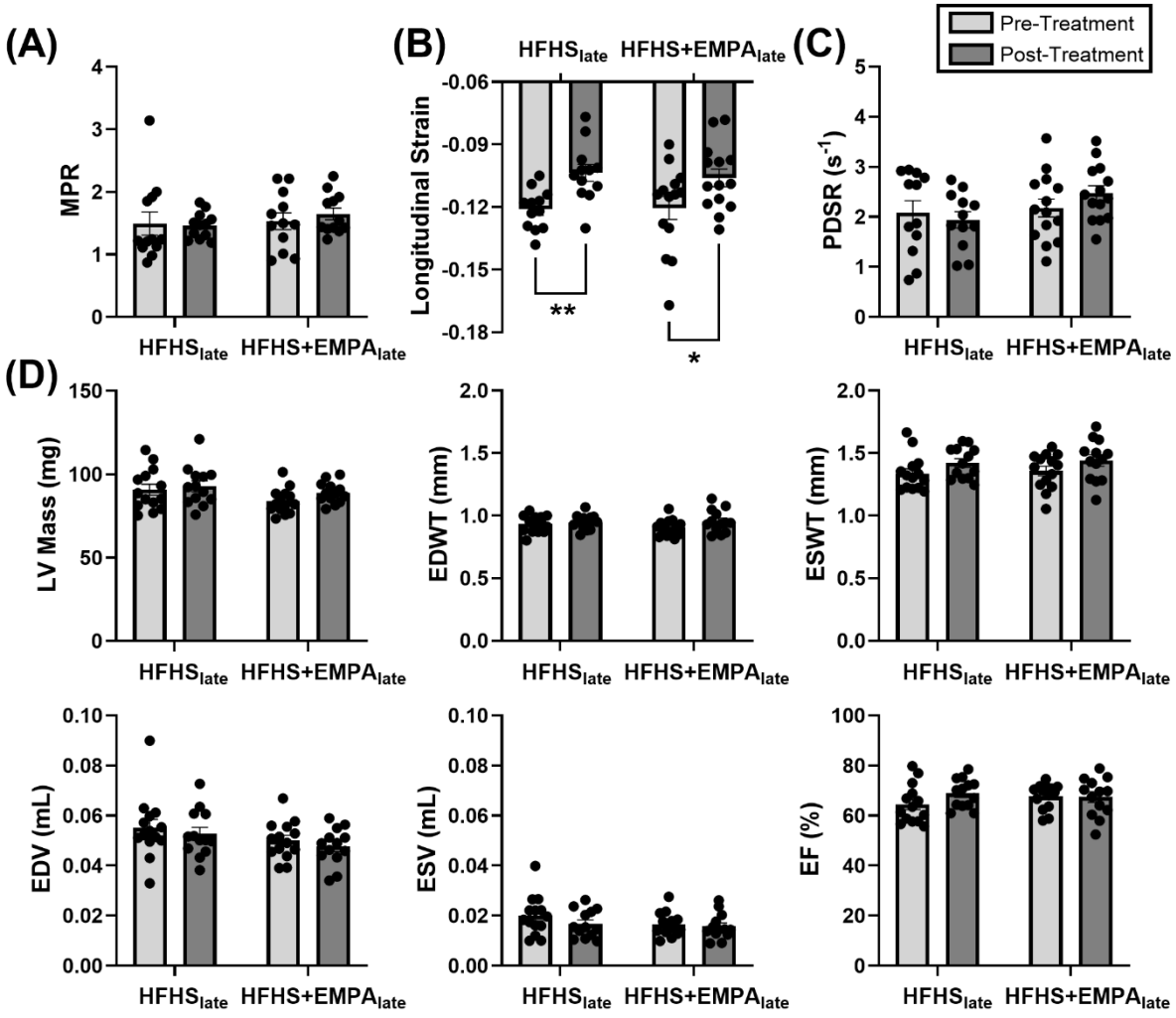

Figure 35 - Effect of late EMPA treatment on MPR, systolic strain, diastolic strain rate, and LV structure and function. (A) MPR (n=12/group), (B) global longitudinal strain ($HFHS_{late}$: n=12, $HFHS+EMPA_{late}$: n=14), and (C) PDSR ($HFHS_{late}$: n=12, $HFHS+EMPA_{late}$: n=14) for $HFHS_{late}$ and $HFHS+EMPA_{late}$ mice pre- and post-treatment. (D) Cine-derived cardiac structure and function parameters including LV mass, EDWT, ESWT, EDV, ESV, and EF in $HFHS_{late}$ and $HFHS+EMPA_{late}$ mice (n=13/group) pre- and post-treatment. Data are shown as mean ± SEM and compared using an RM two-way ANOVA with Šidák's multiple comparisons test.*P<0.05 and **P <0.01 for indicated groups. All other abbreviations as in **Figure 25**, **Figure 29**, and **Figure 30**.

3.3.2.5 Late Empagliflozin Treatment Does Not Reverse Worsening Diastolic Dysfunction

Peak global longitudinal end-systolic strain was similar between HFHS+EMPA$_{late}$ and HFHS$_{late}$ mice at 15 and 23 weeks on HFHSD (**Figure 35B**). Both groups showed a worsening of peak global longitudinal end-systolic strain from 15 to 23 weeks on HFHSD. PDSR was similar between the groups at 15 and 23 weeks on HFHSD and remained unchanged for both HFHS+EMPA$_{late}$ and HFHS$_{late}$ groups from 15 to 23 weeks on HFHSD (**Figure 35C**). These findings indicate that EMPA did not reverse established coronary microvascular and diastolic dysfunction. Similarly, no differences in cine-derived cardiac structure or function metrics were observed between groups or across time points (**Figure 35D**).

3.3.2.6 Late Empagliflozin Treatment Does Not Shift Macrophage Polarization in the Heart

Flow cytometry analysis revealed no significant differences in the percentage of NOS2^{+} (M1) or CD163^{+} (M2) macrophages in the heart between HFHS+EMPA$_{late}$ and HFHS$_{late}$ mice (**Figure 36**).

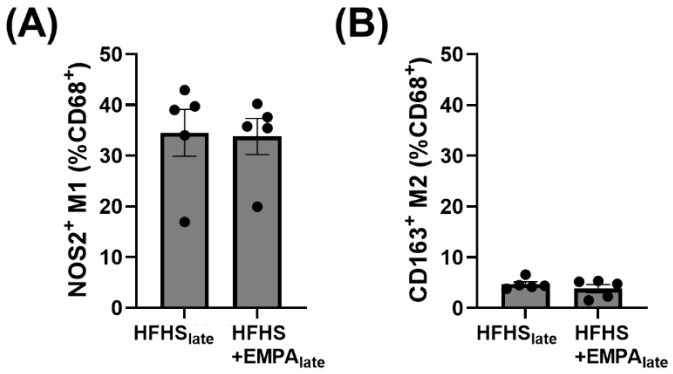

Figure 36 - Effect of late EMPA treatment on macrophage polarization in the heart. (A) NOS2^{+} M1 cells and (B) CD163^{+} M2 cells isolated from the hearts of mice fed an HFHS for 23 weeks or an HFHS for 15 weeks followed by HFHS+EMPA for an additional 8 weeks (n=5/group). All other abbreviations as in **Figure 25**.

3.4 Discussion

The major findings of these studies utilizing an HFHSD-induced mouse model of early stage cardiometabolic HFpEF are that: (a) SGLT2 inhibition initiated concurrently with the start of an 18 week HFHSD improved MPR and diastolic dysfunction, and reduced EAT volume, CMR proinflammatory EAT biomarkers, and $NOS2^+$ macrophage M1 polarization, and (b) SGLT2 inhibition initiated after the establishment of impaired MPR and diastolic dysfunction due to 15 weeks of an HFHSD failed to reverse these HFpEF features and failed to reverse CMR proinflammatory EAT biomarkers and $NOS2^+$ macrophage M1 polarization.

These results are consistent with a disease mechanism model where obesity drives the accumulation of proinflammatory EAT and myocardial lipid, which promote myocardial and vascular dysfunction. Saturated fatty acid overload in hypertrophic adipocytes leads to TLR4 pathway activation causing proinflammatory cytokine secretion by adipocytes and macrophage recruitment and M1 polarization in the EAT[75]. Inflammatory cytokines are secreted into the shared microcirculation and transmitted to the myocardium via vasocrine and paracrine signaling[86]. This leads to an increase in $NOS2^+$ M1-polarized macrophages in the myocardium where they exacerbate oxidative and nitrosative stress. These processes collectively contribute to myocardial and vascular dysfunction, linking EAT inflammation to the pathophysiology of cardiometabolic HFpEF.

This study shows the potential of new CMR adipose tissue imaging methods, recently developed for mice[31] and humans[28], that quantify biomarkers of proinflammatory EAT and myocardial lipid, including EAT FAC (SFA, MUFA, PUFA), PDFF, and T1, as well as myocardial PDFF. Our findings suggest that high SFA, low PUFA, and short T1 values reflect a proinflammatory state in EAT. Early EMPA treatment reduced EAT SFA, increased PUFA, and

prolonged T1, while leaving the FAC and T1 of SAT unchanged, underscoring the specific effects of EMPA on VAT, particularly EAT. The FAC changes are consistent with known effects of SGLT2 inhibitors on lipid metabolism, including reduced lipogenesis and increased lipolysis[169]. The T1 changes, which are consistent with findings of higher VAT T1 in healthy individuals compared to those with obesity[92] and after bariatric surgery[205], may reflect reduced reactive oxygen species, altered FAC, adipose tissue browning, or morphological changes such as smaller adipocytes and fewer crown-like structures. These findings align with our observation of decreased macrophage infiltration and reduced adipocyte size following early EMPA treatment. Furthermore, early EMPA treatment significantly reduced myocardial PDFF, indicating less myocardial fat accumulation. In contrast, late EMPA treatment failed to improve myocardial PDFF, consistent with findings from another group who reported that EMPA treatment, initiated after established myocardial fat accumulation, did not attenuate myocardial fat in an HFHSD mouse model[206]. While previous studies consistently show that SGLT2 inhibitors reduce EAT volume[207–209] and adipose tissue inflammation[151,210–212], our results provide further insight into EAT-specific FAC changes, including reduced SFA and increased PUFA, as well as prolonged T1 relaxation times detectable through non-invasive CMR.

This study highlights the importance of earlier vs later intervention with SGLT2 inhibitors. While early treatment with EMPA reduced EAT volume, CMR proinflammatory EAT biomarkers, and $NOS2^+$ macrophage M1 polarization leading to improved MPR and diastolic function, late treatment with EMPA also reduced EAT volume, but did not impact CMR proinflammatory EAT biomarkers, decrease $NOS2^+$ macrophage M1 polarization, or reverse impaired MPR or diastolic dysfunction. These results suggest that metrics of EAT quality (FAC, PDFF, and T1) may be more relevant biomarkers of proinflammatory EAT in the context of HFpEF than EAT volume, and that

initiation of SGLT2 inhibitor treatment early in disease progression may offer improved therapeutic efficacy.

Our study adds to the growing evidence that SGLT2 inhibitors promote a shift in macrophage polarization toward an anti-inflammatory state. To our knowledge, the present data are the first to show a decrease in macrophage M1 polarization in the EAT with EMPA treatment. We observed a similar anti-inflammatory shift in the heart after early EMPA treatment, with fewer M1 macrophages and more Mox macrophages. These findings align with prior research showing that EMPA reduces M1 macrophages in the epididymal adipose tissue[151], and other research showing that the SGLT2 inhibitor, dapagliflozin, increases M2 macrophage infiltration in infarcted rat hearts[213]. Interestingly, the increase in myocardial antioxidant Mox macrophages with early EMPA treatment is a novel finding that may reflect enhanced antioxidant capacity, helping to counteract the elevated oxidative stress induced by an HFHSD[214]. Failure of late EMPA treatment to reduce proinflammatory M1 macrophages in the heart underscores the importance of early intervention for the anti-inflammatory and cardiovascular benefits of SGLT2 inhibitors.

These experiments firmly established that early treatment with EMPA improves the coronary microvascular response to adenosine receptor agonism. While previous studies have presented results related to this effect, our results unambiguously show that EMPA improves the response of the coronary microvessels to adenosine receptor agonism without complication from obstructive coronary artery disease (CAD)[215]. In a study of patients with stable CAD, Leccisotti et al.[215] reported improved myocardial flow reserve with dapagliflozin treatment using adenosine-induced hyperemia and PET/CT imaging. Adingupu et al.[216] demonstrated that EMPA improved coronary flow velocity reserve based on isoflurane-induced hyperemia and ultrasound imaging in an ob/ob$^{-/-}$ mouse model of obesity. Unlike these studies, we used adenosine—a clinically relevant

vasodilator—in a model of coronary microvascular disease without atherosclerosis. This allowed us to directly measure the improved coronary microvascular response to adenosine receptor agonism, as reflected in the increased MPR. This finding was supported by ex vivo coronary microvascular reactivity experiments, which are the first to directly quantify enhanced adenosine-induced dilation of small coronary vessels with EMPA treatment.

We observed improvements in diastolic function with early, but not late, EMPA treatment. Quantitative assessments of myocardial strain-time curves showed a significant increase in peak diastolic strain rate with early EMPA treatment. These findings are in line with prior preclinical and clinical studies investigating SGLT2 inhibitor treatment and cardiac diastolic function. Habibi et al.[192] found that EMPA improved diastolic function using Doppler echocardiography in female diabetic mice, and Verma et al.[117] identified a similar improvement in tissue Doppler-derived diastolic function in diabetic patients treated with EMPA. Additionally, a randomized, controlled trial in patients with diabetes found that dapagliflozin treatment was associated with a significant improvement in LV diastolic dysfunction assessed with diastolic stress echocardiography compared with placebo[118]. Given that diastolic dysfunction is central to HFpEF, and diastolic function metrics are independent predictors of heart failure incidence[217,218], our findings highlight the potential of early EMPA treatment to improve outcomes in individuals at risk for HFpEF.

3.5 Limitations

Despite its insights, this study has limitations. The specific molecular mechanisms by which EMPA improves EAT quality, myocardial perfusion, and diastolic function were not the focus of this study, emphasizing the need to further investigate the interplay between adipose tissue quantity and composition, macrophage-driven inflammation, and cardiovascular dysfunction. The duration of late EMPA treatment may have been insufficient to fully assess its potential to reverse

HFHSD-induced cardiovascular impairments. Lastly, blood pressure measurements were not included in the protocol, precluding the ability to consider its role in the findings.

3.6 Conclusion

Multiparametric CMR and other experimental methods were used to show the efficacy of early EMPA administration in improving EAT proinflammatory biomarkers, shifting macrophage polarization toward a less proinflammatory state, reducing myocardial lipid, and preventing impaired MPR and diastolic dysfunction in an HFHSD mouse model. Similar studies evaluating the use of EMPA to reverse established MPR impairments and diastolic dysfunction resulted in negative findings, as this therapy did not improve MPR and diastolic function in this context. In these contexts, novel CMR biomarkers such as EAT FAC and T1 and myocardial PDFF show utility for detecting key and modifiable adipose-related features of cardiometabolic HFpEF.

Chapter 4: Macrophage-specific inducible nitric oxide synthase (NOS2) as a mediator of coronary microvascular dysfunction in a mouse model of early stage cardiometabolic HFpEF

4.1 Introduction

Nitric oxide (NO) is synthesized by nitric oxide synthase (NOS) enzymes and is produced by nearly all cell types[49]. The inducible member of the NOS family, NOS2 (formerly iNOS), is activated in response to bacterial endotoxins, inflammatory cytokines, and nutrient overload[219]. Unlike the constitutively expressed endothelial NOS (eNOS) and neuronal NOS (nNOS), which generate small amounts of NO under physiological conditions, NOS2 is absent in healthy tissues but, when induced, produces large quantities of NO over prolonged periods[48,220]. While this sustained NO production is essential for host defense, excessive NOS2 activity contributes to oxidative and nitrosative stress, promoting tissue damage[220]. NOS2 has been implicated in a range of inflammatory and cardiometabolic diseases, including diabetes, myocardial infarction, coronary microvascular disease (CMD), and heart failure with preserved ejection fraction (HFpEF)[49,51,221].

Cardiometabolic HFpEF is driven by obesity and metabolic stress, which promote a chronic, low-grade inflammatory state and dysregulated immune responses[222]. CMD, present in up to 75% of patients with HFpEF, is a major contributor to HFpEF disease progression[1]. Increased NOS2 expression has been observed in both human HFpEF hearts and preclinical models, and is upregulated in response to high-fat diets[51,220]. While the importance of NOS2 in obesity-induced HFpEF and CMD is increasingly recognized, the specific cellular source of NOS2 in CMD and HFpEF remains unclear.

Macrophages are key regulators of inflammation in obesity and cardiovascular disease, contributing to coronary artery disease, myocarditis, cardiomyopathy, heart failure, and atherosclerosis, among other diseases[223]. They also play a central role in adipose tissue inflammation, shifting from an anti-inflammatory M2 phenotype to a pro-inflammatory, NOS2-expressing M1 phenotype, where they produce cytokines that amplify local and systemic

inflammation[175]. Notably, NOS2 is induced in multiple metabolic tissues during obesity, with macrophages serving as a predominant source in adipose tissue[220,224]. Macrophages also infiltrate the myocardium in HFpEF, where they drive myocardial fibrosis and dysfunction[225]. Since visceral adipose tissue is a hallmark feature of HFpEF[61] and macrophages are a major source of NOS2 within adipose depots[226], it is plausible that macrophage-derived NOS2 contribute to disease progression. Epicardial adipose tissue (EAT) is particularly relevant as it shares a microcirculation with the underlying myocardium and serves as a reservoir for inflammatory macrophages and cytokines that can influence myocardial function through vasocrine and paracrine signaling[3]. Additionally, studies in Chapter 3 demonstrated that sodium-glucose cotransporter-2 (SGLT2) inhibition reduced NOS2+ macrophages in both the EAT and myocardium, while improving coronary microvascular and diastolic function in a mouse model of cardiometabolic HFpEF. These factors suggest that macrophage-derived NOS2 may be a key mediator of coronary microvascular and diastolic dysfunction in HFpEF.

In this study, we use a myeloid-specific NOS2 knockout mouse model (*Nos2*$^{\text{LysM-KO}}$) to investigate the role of macrophage-derived NOS2 in HFHSD-induced CMD and diastolic dysfunction. Using multiparametric cardiac magnetic resonance (CMR), including rest and adenosine stress arterial spin labeling (ASL) to quantify myocardial blood flow and myocardial perfusion reserve, and displacement encoding with stimulated echoes (DENSE) to assess myocardial strain and diastolic function, we test the hypothesis that NOS2 produced by macrophages is a contributor to coronary microvascular and diastolic dysfunction. Understanding the cell-specific contributions of NOS2 to CMD and HFpEF pathophysiology may provide insights into new therapeutic strategies targeting inflammation and microvascular dysfunction in HFpEF.

4.2 Methods

4.2.1 Experimental Design

All animal studies were performed in accordance with protocols that conformed to the Declaration of Helsinki as well as the Guide for Care and Use of Laboratory Animals[164] and were approved by the Animal Care and Use Committee at the University of Virginia. All mice were maintained at the University of Virginia Center for Comparative Medicine pathogen-free vivarium facility. Experiments were performed to test the hypothesis that macrophages are the NOS2-expressing cell type responsible for the development of coronary microvascular and diastolic dysfunction resulting from 18 weeks of an HFHSD.

Male *Nos2* LysM-Cre ($Nos2^{LysM\text{-}KO}$) mice and homozygous *Nos2* floxed ($Nos2^{fl/fl}$) control mice were studied. $Nos2^{LysM\text{-}KO}$ mice were generated using the Cre-lox system by breeding $Nos2^{fl/fl}$ mice with LysM-Cre mice. Genotyping was performed by Transnetyx (Cordova, TN) to confirm the presence of the LysM-Cre transgene and *Nos2* floxed alleles. Four groups of mice were studied: (1) $Nos2^{fl/fl}$ mice fed a standard chow diet (SCD) (SCD-$Nos2^{fl/fl}$), (2) $Nos2^{fl/fl}$ mice fed an HFHSD (HFHSD-$Nos2^{fl/fl}$), (3) $Nos2^{LysM\text{-}KO}$ mice fed an SCD (SCD-$Nos2^{LysM\text{-}KO}$), and (4) $Nos2^{LysM\text{-}KO}$ mice fed an HFHSD (HFHSD-$Nos2^{LysM\text{-}KO}$). A timeline for the experiment is shown in **Figure 37**. Diets were initiated at 10 weeks of age and were continued for 18 weeks. GTT was performed at 17 weeks post-diet (n = 9-13/group). All mice underwent CMR at 18 weeks post-diet (n = 15/group). After 20 weeks on diet, mice fed a HFHSD were euthanized and used for coronary arteriolar reactivity (n = 5/group).

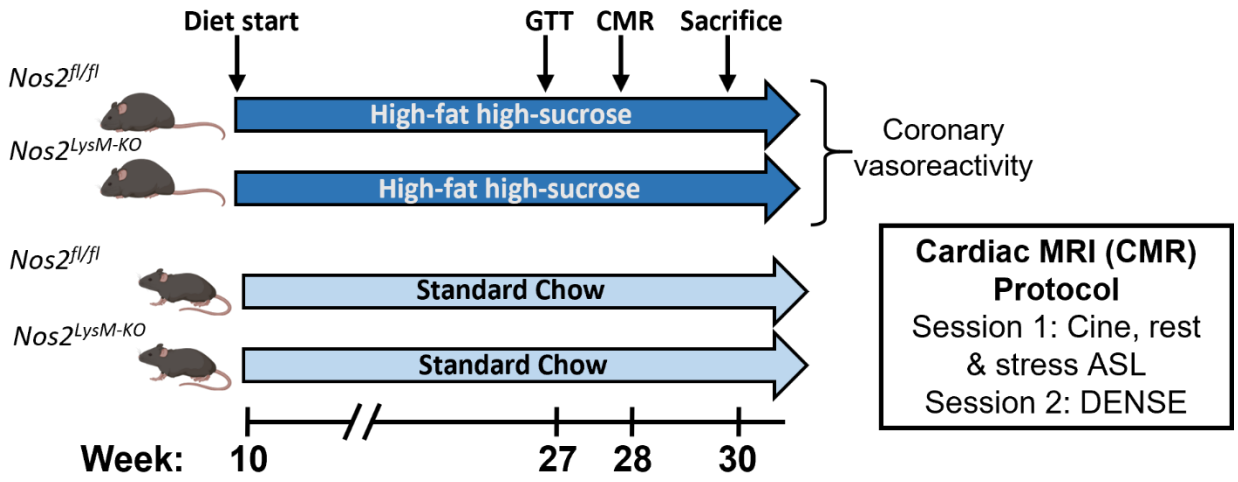

Figure 37 - Experimental design. Timeline for assessing the role of macrophage NOS2 in HFHSD-induced cardiac dysfunction using *Nos2*$^{LysM\text{-}KO}$ and *Nos2*$^{fl/fl}$ control mice fed either a high-fat high-sucrose diet or standard chow for 18 weeks.

4.2.2 CMR Protocol

CMR studies were performed over two sessions separated by 2-3 days. CMR was performed on both a 9.4T system (Biospec 94/20, Bruker Biospin, Germany) and a 7T system (Clinscan, Bruker/Siemens) using a ^{1}H transmit-receive quadrature volume radiofrequency coil with 35 mm inner diameter (Bruker BioSpin GmbH, Germany). During CMR studies, the electrocardiogram (ECG), body temperature, and respiration were continuously monitored (SA Instruments, Stony Brook, New York, USA). Mice were anesthetized with 1% isoflurane and maintained at a body temperature of 36 ± 0.5°C using circulating warm water.

For all experiments, the CMR protocol included (1) arterial spin labeling (ASL) at rest and with adenosine vasodilation to quantify myocardial blood flow (MBF) and MPR for the assessment of coronary microvascular function[194,195], (2) displacement encoding with stimulated echoes (DENSE) imaging to measure global longitudinal strain and peak diastolic strain rate (PDSR) for

the evaluation of LV systolic and diastolic function[140], and (3) cine imaging covering the entire LV to measure cardiac structure and function parameters including LV mass, end-diastolic wall thickness (EDWT), end-systolic wall thickness (ESWT), end-diastolic volume (EDV), end-systolic volume (ESV), and ejection fraction (EF). Rest and stress ASL and cine imaging were performed at session 1 of CMR at 9.4T, and DENSE imaging was performed at session 2 of CMR at 7T. Body weight was recorded for all mice at the beginning of each imaging study.

4.2.2.1 Cine Imaging

Six to 8 short-axis slices were acquired, covering the LV from base to apex. Imaging parameters included: repetition time (TR): 4.0 ms; TE: 1.35 ms; temporal resolution: 4.0 ms; FOV: 25 × 25 mm^2; matrix size: 128 ×128; flip angle: 15°; number of averages = 3; resolution = 0.2 × 0.2 mm^2; total scan time approximately 2 minutes per slice.

4.2.2.2 Myocardial Perfusion Imaging

At session 1, an intraperitoneal catheter was inserted for delivery of the vasodilator, adenosine (Sigma-Aldrich) (18 μg/min), during imaging. Rest perfusion imaging of a mid-ventricular short-axis slice was then performed using a respiratory-gated ASL method[195]. Thereafter, adenosine was infused intravenously and 10 minutes later ASL was repeated. Imaging parameters for ASL included: TE: 2.5 ms; TR: 10.0 ms; FOV: 25 × 25 mm^2; matrix size: 128 × 128; flip angle: 7°; slice thickness: 1.0 mm; saturation band thickness: 2.5 mm; number of averages: 9; resolution = 0.2 × 0.2 mm^2; total scan time approximately 10 minutes per rest or stress scan.

4.2.2.3 Myocardial Strain Imaging

DENSE strain imaging[140] was performed on a 4-chamber long-axis slice. Imaging parameters included: FOV: 32 x 32 mm^2; matrix size: 128 x 128; slice thickness: 1.0 mm; TR: 7.0 ms; TE:

2.45 ms; number of averages: 4; spatial resolution = 0.25 × 0.25 mm^2; total scan time approximately 14 minutes.

4.2.3 CMR Image analysis

Image analysis was performed using MATLAB 2023a (MathWorks, Natick, MA). CMR data were excluded from analysis if poor-quality ECG and/or respiratory signals led to severe image artifacts. For MBF quantification, rest and adenosine stress perfusion images were analyzed using methods previously described[195]. MPR was calculated as the ratio of stress perfusion to rest perfusion. Strain analysis of DENSE images was performed using the DENSE analysis tool[141,198]. Global longitudinal strain and peak diastolic strain rate were measured as metrics of systolic and diastolic function, respectively. Cine images were analyzed using Segment version 4.1.0.1 R14284b package. Specifically, the end-diastolic and end-systolic frames were identified, and the endocardial and epicardial contours were manually drawn on these frames for all slices. Using Segment, EDWT, ESWT, EDV, ESV, EF, and LV mass were calculated.

4.2.4 Glucose Tolerance Tests

For GTTs, mice were injected intraperitoneally with sterile glucose (8 g/kg body weight) in deionized water after a 16 hour overnight fast. Blood samples were taken from the tail vein before injection to measure the fasting blood glucose, and 10, 30, 60, 90, and 120 minutes after injection of the glucose solution. The area under the curve (AUC) was calculated by trapezoidal approximation to evaluate glucose tolerance[200].

4.2.5 Vascular Reactivity

Mice were euthanized and coronary arterioles were isolated and freed of the surrounding cardiac myocytes. Using an arteriography system (Danish MyoTechnology), the arterioles were

cannulated at both ends and pressurized to 40 mm Hg as previously described[201–203]. Arterioles were pre-constricted with 10 µmol/L phenylephrine. Vessel relaxation measurements are reported as a percent dilation of the initial vessel diameter. Cumulative dose responses to endothelial-independent vasodilators – adenosine and the vascular smooth muscle cell (VSMC)-specific dilator sodium nitroprusside (SNP) – were measured as previously described[201–203].

4.2.6 Statistics

All data are presented as mean ± standard error of the mean. Statistical analyses were performed using GraphPad Prism version 10.4.0. Variance was assessed using an F-test, and normality was tested with the Shapiro-Wilk test. A p-value < 0.05 was considered statistically significant.

Vascular reactivity curves were analyzed using an RM two-way ANOVA with Šidák's multiple comparisons test to compare responses between groups (HFHSD-*Nos2*$^{LysM\text{-}KO}$ vs HFHSD-*Nos2*$^{fl/fl}$) at each vasodilator dose. Blood glucose curves were analyzed with an RM three-way ANOVA. Following a significant three-way interaction, an RM two-way ANOVA with Šidák's multiple comparisons test was used to assess differences at individual time points (0-120 minutes). For all other comparisons, an ordinary two-way ANOVA with Šidák's multiple comparisons test was performed. When significant variance differences were detected, a *t*-test with Welch's correction was used.

4.3 Results

4.3.1 Genetic Suppression of Macrophage NOS2 Does Not Affect HFHSD-Induced Weight Gain or Glucose Intolerance

After 18 weeks, both HFHSD groups showed similar weight gain and glucose intolerance, with significantly greater weight gain (*Nos2*$^{LysM\text{-}KO}$ HFHSD vs *Nos2*$^{LysM\text{-}KO}$ SCD: 40.05 ± 1.71 g vs 29.57 ± 0.77 g, p = <0.0001; *Nos2*$^{fl/fl}$ HFHSD vs *Nos2*$^{fl/fl}$ SCD: 42.95 ± 1.66 g vs 30.71 ± 0.49 g,

p = <0.0001) and elevated glucose intolerance (*Nos2*$^{LysM\text{-}KO}$ HFHSD AUC vs *Nos2*$^{LysM\text{-}KO}$ SCD AUC: (48.84 ± 3.72) × 10^3 min·mg/dL vs (32.67 ± 2.45) × 10^3 min·mg/dL, p = 0.0034; *Nos2*$^{fl/fl}$ HFHSD AUC vs *Nos2*$^{fl/fl}$ SCD AUC: (51.13 ± 5.01) × 10^3 min·mg/dL vs (32.58 ± 1.18) × 10^3 min·mg/dL, p = 0.0005) compared to their respective SCD groups (**Figure 38**).

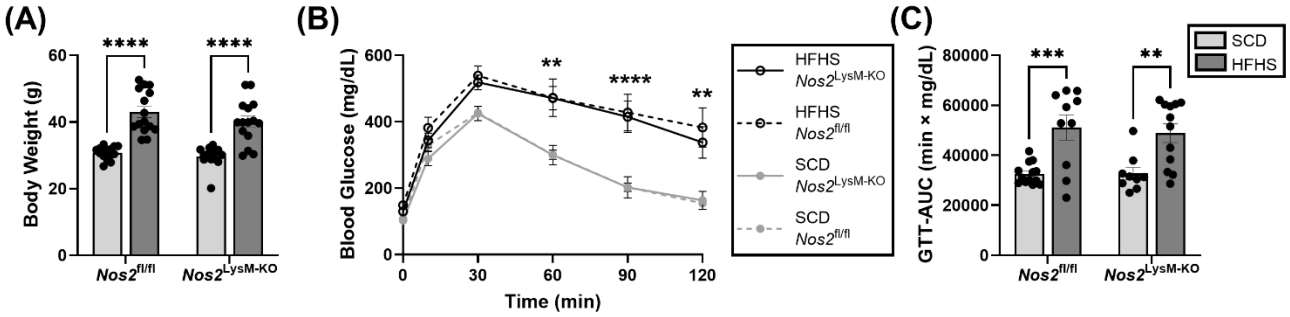

Figure 38 - Effect of macrophage NOS2 on body weight and GTT. (A) Body weight in grams for Nos2$^{fl/fl}$ and Nos2$^{LysM\text{-}KO}$ mice (n=15/group) fed an HFHS diet or SCD for 18 weeks. (B) Average glucose tolerance curves and (C) corresponding AUC values for Nos2$^{fl/fl}$ (SCD: n=13, HFHS: n=10) and Nos2$^{LysM\text{-}KO}$ (SCD: n=9, HFHS: n=12) mice fed an HFHS diet or SCD for 17 weeks. Data are shown as mean ± SEM. Blood glucose curves were analyzed with an RM three-way ANOVA followed by an RM two-way ANOVA with Šidák's multiple comparisons test to assess differences at individual time points (0-120 min). All other comparisons are made using an ordinary two-way ANOVA with Šidák's multiple comparisons test .**P <0.01, ***P <0.001, and ****P <0.0001 for either HFHS group vs SCD group. GTT, glucose tolerance test; AUC, area under the curve. HFHS, high-fat high-sucrose; SCD, standard chow diet. Other abbreviations as in **Figure 37**.

4.3.2 Genetic Suppression of Macrophage NOS2 Prevents HFHSD-Induced Coronary Microvascular Dysfunction

Rest myocardial blood flow was similar across all groups (**Figure 39A**). However, after 18 weeks of an HFHSD, while stress perfusion was significantly reduced in *Nos2*$^{fl/fl}$ mice compared to SCD controls (7.07 ± 0.60 mL/g/min vs 10.89 ± 0.61 mL/g/min, p = 0.0003), it was preserved in the *Nos2*$^{LysM\text{-}KO}$ mice compared to SCD controls mice (9.77 ± 0.63 mL/g/min vs 9.43 ± 0.76 mL/g/min) (**Figure 39B**). Accordingly, MPR was reduced in *Nos2*$^{fl/fl}$ mice on an HFHSD compared to SCD controls (1.39 ± 0.10 vs 2.21 ± 0.08, p < 0.0001), but maintained in *Nos2*$^{LysM\text{-}KO}$ mice compared to SCD controls (1.90 ± 0.12 vs 2.07 ± 0.15) (**Figure 39C**). These results indicate that suppressing NOS2 specifically in myeloid cells prevents the impaired MPR under HFHSD conditions.

Ex vivo vasoreactivity tests showed preservation of coronary arteriolar dilation in *Nos2*$^{LysM\text{-}KO}$ mice compared to *Nos2*$^{fl/fl}$ control mice on a HFHSD, as reflected in cumulative dose-response curves to adenosine (p < 0.05) and SNP (p < 0.05) (**Figure 39D-E**). These ex vivo findings support the in vivo CMR results, demonstrating that macrophage-specific NOS2 suppression improves coronary arteriolar dilation under HFHSD conditions.

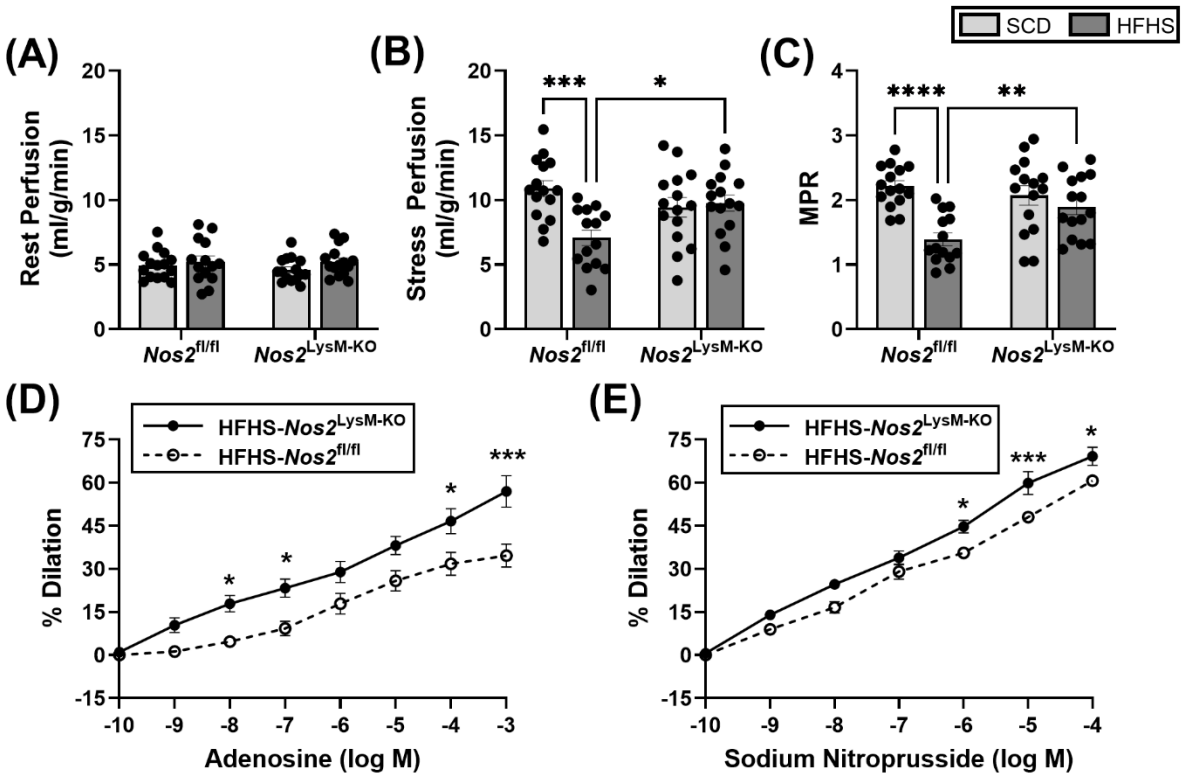

Figure 39 - Effect of macrophage NOS2 on myocardial perfusion, MPR, and coronary arteriole vasoreactivity. (A) Rest perfusion, (B) adenosine-induced stress perfusion, and (C) MPR for $Nos2^{fl/fl}$ (SCD: n=15, HFHS: n=14) and $Nos2^{LysM\text{-}KO}$ (n=15/group) mice fed an HFHS diet or SCD for 18 weeks. Cumulative arteriolar dose-response curves to (D) adenosine and (E) sodium nitroprusside in $Nos2^{fl/fl}$ and $Nos2^{LysM\text{-}KO}$ mice (n=5/group) after 20 weeks of HFHS diet. Data are shown as mean ± SEM. Dose-response curves are compared using an RM two-way ANOVA with Šidák's multiple comparisons test. All other data is compared using an ordinary two-way ANOVA with Šidák's multiple comparisons test. *P <0.05, **P <0.01, ***P <0.001, and ****P <0.0001 for indicated groups. MPR, myocardial perfusion reserve. All other abbreviations as in **Figure 37**.

4.3.3 Genetic Suppression of Macrophage NOS2 Does Not Prevent HFHSD-Induced Diastolic Dysfunction

Trends of reduced peak global end-systolic strain were seen in HFHSD groups compared to SCD groups (**Figure 40A**), but peak global end-systolic strain was similar between HFHSD-*Nos2*$^{LysM\text{-}KO}$ and HFHSD-*Nos2*$^{fl/fl}$ mice. After 18 weeks of HFHSD, there was a trend toward a decrease in PDSR in HFHSD mice compared to SCD controls (**Figure 40B**). No differences in PDSR were observed between HFHSD-*Nos2*$^{LysM\text{-}KO}$ and HFHSD-*Nos2*$^{fl/fl}$ mice. These results suggest that myeloid-specific NOS2 does not significantly impact diastolic or systolic dysfunction under HFHSD conditions. Trends of small increases in LV mass, EDWT, and ESWT were seen in both HFHSD groups compared to SCD groups, however no significant differences in cine-derived metrics of cardiac structure or function were observed between groups after 18 weeks on either diet (**Figure 40C**).

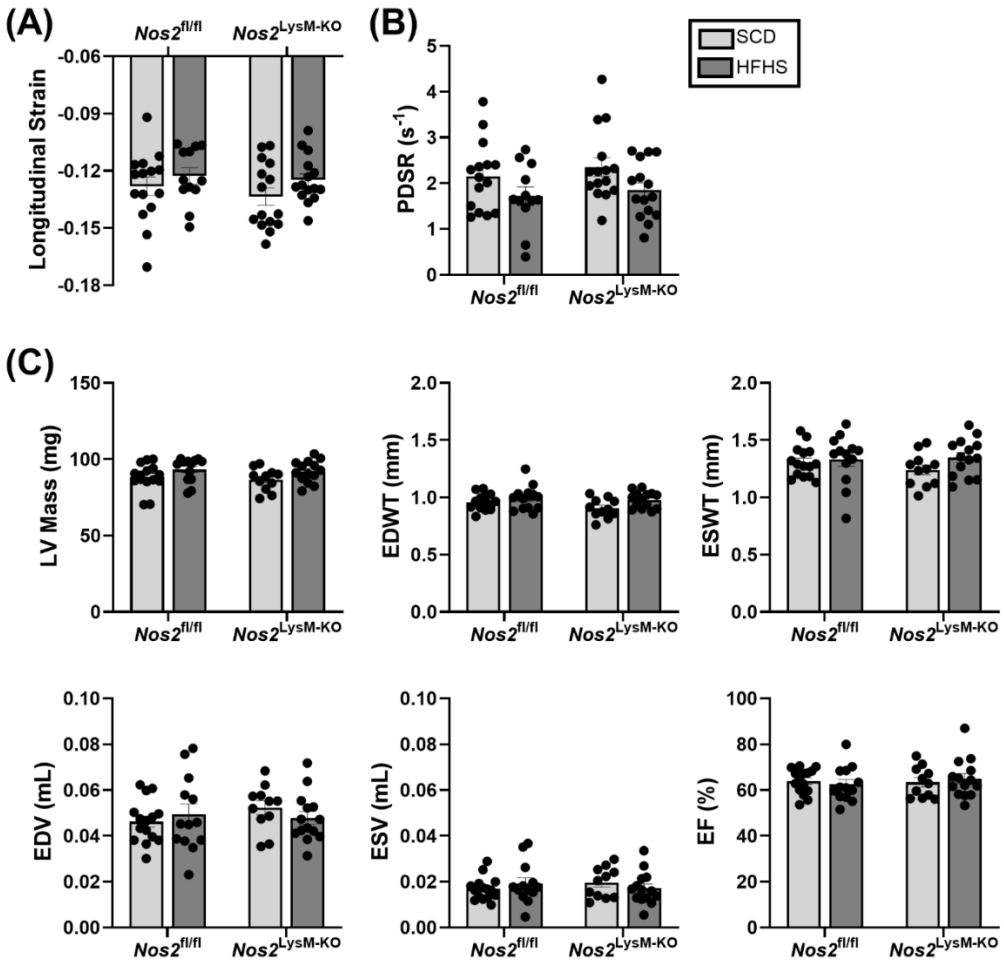

Figure 40 - Effect of macrophage NOS2 on systolic strain, diastolic strain rate, and LV structure and function parameters. (A) Global longitudinal strain and (B) PDSR for $Nos2^{fl/fl}$ (SCD: n=15, HFHS: n=12) and $Nos2^{LysM\text{-}KO}$ (SCD: n=15, HFHS: n=15) mice fed an HFHS diet or SCD for 18 weeks. (C) Cine-derived cardiac structure and function parameters including LV mass, EDWT, ESWT, EDV, ESV, and EF for $Nos2^{fl/fl}$ (SCD: n=15, HFHS: n=13) and $Nos2^{LysM\text{-}KO}$ (SCD: n=11, HFHS: n=14) mice fed an HFHS diet or SCD for 18 weeks. Data are shown as mean ± standard error and compared using an ordinary two-way ANOVA with Šidák's multiple comparisons test.*P<0.05 for indicated groups. PDSR, peak diastolic strain rate; LV, left ventricular; EDWT, end-diastolic wall thickness; ESWT, end-systolic wall thickness; EDV, end-diastolic volume; ESV, end-systolic volume; EF, ejection fraction. All other abbreviations as in **Figure 37**.

4.4 Discussion

This study investigated the role of macrophage-derived NOS2 in CMD and diastolic dysfunction using a myeloid-specific *Nos2* knockout in an HFHSD model of early stage cardiometabolic HFpEF. The major findings of this study are that knockout of *Nos2* from macrophages had no effect on glucose tolerance or weight gain, yet led to preserved adenosine MPR but not to preserved diastolic function after 18 weeks of an HFHSD.

Our results contribute to a deeper understanding of the critical roles of NOS2 in CMD and HFpEF. Prior work from our group showed that global *Nos2* deletion completely preserved myocardial perfusion reserve and diastolic function by CMR, which are otherwise impaired by an HFHSD[53]. Additionally, treatment with 1400W, an in vivo inhibitor of NOS2, applied after the establishment of impaired MPR and diastolic function, partially reversed CMD and prevented worsening diastolic dysfunction caused by an HFHSD[53]. These findings were consistent with those of Schiattarella et al., where pharmacological or genetic suppression of NOS2 ameliorated LV diastolic dysfunction and exercise intolerance in a high-fat diet + L-NAME mouse model of HFpEF[51]. In the present study, macrophage-specific NOS2 knockout restored MPR but failed to alleviate diastolic dysfunction caused by an HFHSD. These findings show the role of macrophage NOS2 in obesity-driven coronary microvascular dysfunction, while suggesting that other NOS2 sources may play a role in diastolic dysfunction.

These findings add to the growing body of research defining the specific roles of inflammatory cell-derived NOS2. Our findings are in agreement with those of Lu et al., identifying that disruption of NOS2 in myeloid cells did not protect against high-fat diet-induced obesity and insulin resistance[227]. While myeloid-derived NOS2 does not play a role in insulin resistance, it has been implicated in a range of cardiovascular diseases. Myeloid NOS2 plays a critical role in

vascular inflammation, particularly in atherosclerosis, where it is abundantly expressed by macrophages and smooth muscle cells in advanced lesions[228]. Specifically, myeloid NOS2 deficiency reduces advanced but not early atherosclerosis[228]. In ischemic heart failure, leukocyte-derived NOS2 drives chronic inflammation and adverse remodeling, with NOS2 deficiency reducing fibrosis, oxidative stress, and myocyte hypertrophy while shifting macrophages toward an anti-inflammatory M2 phenotype[229]. Additionally, myeloid NOS2 plays a distinct role in pulmonary hypertension, where its deletion prevents smoke-induced pulmonary hypertension yet does not protect against emphysema, highlighting vasculature-specific effects[230]. Overall, our findings are consistent with prior studies demonstrating that myeloid NOS2 contributes to vascular dysfunction across multiple disease states, further supporting its role as a mediator of inflammation-driven microvascular impairment.

The failure of macrophage NOS2 deletion to improve diastolic dysfunction suggests that other NOS2-expressing cells contribute to cardiac function in HFpEF. NOS2 is produced by various cell types, including cardiomyocytes, vascular smooth muscle cells, and adipocytes, making it likely that other sources contribute to HFpEF pathology. In diet-induced obesity, NOS2 is induced in adipose tissue, and given its ability to diffuse across tissues and modulate metabolic and inflammatory signaling, adipocyte-derived NOS2 may influence cardiac dysfunction through paracrine effects[220,224]. Additionally, NOS2 is upregulated in the failing heart, raising the possibility that myocardial NOS2 contributes to HFpEF[51]. However, cardiomyocyte-derived NOS2 has not been consistently linked to adverse cardiac effects, and some studies suggest it may even have protective roles in ischemic heart failure. Notably, mice with constitutive cardiac-specific NOS2 overexpression and a substantial increase in NOS2 activity do not develop cardiac dysfunction[231], in the setting of chronic ischemic heart failure, intramyocardial NOS2 has been

shown to improve regional fibrosis and contractility[232]. Future work should continue to investigate cell-specific sources of NOS2 in the context of obesity-induced HFpEF.

4.5 Limitations

Despite its insights, this study has limitations. Studies were performed in male mice, thus potential sex differences were not investigated. This study used a LysM-Cre mouse strain to selectively knockout NOS2, and while this strain is an effective tool to target macrophages, other myeloid cells (e.g., neutrophils, granulocytes, dendritic cells) may also be affected, leaving open the possibility that non-macrophage myeloid cells contribute to NOS2-driven microvascular dysfunction. However, macrophages remain the primary contributors to inflammation in both adipose tissue and the myocardium[233,234]. The roles of non-myeloid NOS2 sources such as vascular smooth muscle cells and cardiomyocytes in diastolic dysfunction were not explored. Future studies should address other cell types to provide a more comprehensive understanding of NOS2 in HFpEF pathophysiology.

4.6 Conclusion

Using multiparametric CMR and a myeloid-specific NOS2 knockout model, this study demonstrated a key and novel role of macrophage NOS2 in coronary microvascular dysfunction in the setting of HFHSD-induced obesity and microvascular dysfunction, contributing to our overall understanding of NOS2 in HFpEF.

Chapter 5: Conclusions and future directions

5.1 Summary of Findings

Aim 1 (Chapter 2) developed and validated an accelerated MRI method for simultaneous in vivo mapping of epicardial adipose tissue (EAT) fatty acid composition (FAC) and T_1 relaxation time at 9.4T, enabling comprehensive assessment of EAT quality. The technique employed an inversion recovery multi-echo gradient echo acquisition with golden-angle radial sampling and interleaved echoes, achieving rate 9.6 acceleration. Images were reconstructed using higher-order singular value decomposition (HOSVD) denoising. Quantitative estimation of saturated (SFA), monounsaturated (MUFA), and polyunsaturated fatty acids (PUFA), as well as number of double bonds (*ndb*) and number of methylene-interrupted double bonds (*nmidb*), and T_1 relaxation times, was validated across acceleration rates in phantoms. Application of the method to drug- and diet-induced mouse models of various metabolic phenotypes revealed that a higher SFA index (EAT/SAT ratio), PDFF index, and lower T_1 index, *ndb* index, and R_2^* in EAT were associated with histologic and molecular markers of inflammation, including increased $F4/80^+$ macrophage infiltration, elevated proinflammatory cytokines, and adipocyte hypertrophy. These findings support the use of multi-parametric FAC and relaxation mapping as noninvasive biomarkers of proinflammatory adipose tissue.

Aim 2 (Chapter 3) applied cardiac magnetic resonance imaging (CMR) to evaluate the effects of early versus late empagliflozin (EMPA) treatment in a high-fat high-sucrose diet (HFHSD) mouse model of early-stage cardiometabolic heart failure with preserved ejection fraction (HFpEF). Early EMPA treatment, initiated concurrently with the HFHSD, prevented EAT accumulation, shifted EAT toward a less proinflammatory profile – characterized by reduced SFA content, increased PUFA content, and elevated T_1 – preserved myocardial perfusion reserve

(MPR), maintained diastolic function, and reduced $NOS2^+$ M1 macrophage infiltration in both EAT and myocardium. In contrast, EMPA treatment initiated after 15 weeks of HFHSD mitigated further weight gain and EAT expansion but did not reverse impairments in MPR or diastolic function and failed to prevent continued deterioration of the EAT inflammatory profile. These findings underscore the importance of early treatment with EMPA and suggest that the cardioprotective effects of EMPA in HFpEF may be mediated, in part, through modulation of EAT quality, thus improving microvascular and myocardial function.

Aim 3 (Chapter 4) tested the hypothesis that macrophage-derived inducible nitric oxide synthase (NOS2) contributes to coronary microvascular and diastolic dysfunction in cardiometabolic HFpEF. In an HFHSD mouse model, myeloid cell-specific knockout of the *Nos2* gene preserved coronary vasodilation in response to adenosine and maintained myocardial perfusion despite the presence of obesity and glucose intolerance. However, macrophage NOS2 suppression did not protect against diastolic dysfunction, indicating that macrophage NOS2 contributes to microvascular, but not myocardial, impairments. These findings enhance mechanistic understanding of the cellular sources of oxidative and nitrosative stress in HFpEF.

5.2 Future Directions

5.2.1 Joint MRI FAC and T_1 mapping of EAT

The method established in Chapter 2 provides a foundation for noninvasive characterization of EAT quality in vivo. However, several opportunities exist to further refine the pulse sequence, reduce sources of modeling bias, and expand the biological insight gained from these measurements.

Modifications to the pulse sequence and k-space trajectory could improve temporal efficiency and reduce redundancy in sampling. Implementation of a bipolar readout could shorten

echo spacing such that a third echo could be added to the echo train, thus reducing the total scan time. Replacing the inversion recovery preparation with a saturation recovery preparation could eliminate the need for multiple RR interval pauses. Additionally, redesigning the golden-angle sampling scheme to avoid repeating trajectories along either the echo time or inversion time dimensions would allow for more variable k-space coverage and potentially improve reconstruction by increasing sampling incoherence. These approaches, in combination with an iterative reconstruction method such as HD-PROST, may reduce noise, improve parameter estimation, and allow for higher acceleration rates[154].

The current signal model assumes a single T_1 and R_2^* for all spectral species, introducing potential bias due to known differences in the relaxation properties of water and individual fat resonances. A more accurate model could include separate T_1 and R_2^* values for fat and water. While previous studies suggest that T_1 differences between water and fat may minimally affect fatty acid composition estimates[235], the water and fat-specific T_1 values may still provide relevant biological information. One potential approach would involve separating fat and water signals at each TI and performing independent T_1 mapping of each component. Although preliminary implementation of this strategy was explored, further work is needed to assess its biological relevance, validity in fat/water/T_1 emulsion phantoms, and robustness in vivo.

To strengthen biomarker validation, future studies should increase the sample size for cytokine profiling, particularly in EAT, where limited tissue availability can limit the number of analyzable samples. Investigating additional, larger fat depots may enable more robust detection of inflammatory markers and help clarify relationships with MRI-derived metrics such as FAC and relaxation parameters. It would also be valuable to correlate EAT imaging parameters with flow cytometry-based quantification of macrophage subpopulations to determine how these

markers reflect the balance of proinflammatory (M1) and anti-inflammatory (M2) macrophages. Performing flow cytometry in the same animals used for imaging would allow for direct correlation between immune cell phenotypes and MRI biomarkers.

5.2.2 SGLT2-inhibition in the treatment of cardiometabolic HFpEF

The current study evaluated an 8-week EMPA treatment window following 15 weeks of HFHSD to model disease reversal. Future studies should explore whether longer treatment durations can elicit therapeutic effects. A longer reversal timeline may be necessary to observe improvements once disease is more established.

Additional studies should examine the effects of other pharmacologic agents shown to benefit patients with HFpEF, including glucagon-like peptide-1 receptor agonists (GLP-1RAs), which have been associated with weight loss and reduced inflammation[190,236]. Investigating how these agents compare to or synergize with SGLT2 inhibitors in modulating EAT quality and cardiac function could inform therapeutic approaches to HFpEF.

In the reversal arm, EAT saturation increased in both EMPA-treated and untreated groups from week 25 to week 33, despite divergent trends in EAT volume. This suggests that changes in EAT quality may occur independently of changes in EAT quantity and could be dynamic over time. Future work should perform longitudinal imaging of EAT FAC and link these changes to evolving microvascular and cardiac function. Identifying whether alterations in EAT composition precede the development of coronary microvascular dysfunction or diastolic impairment would provide insight into the role of EAT as a transducer of metabolic inflammation.

This study was limited to male mice, but future work should include female cohorts to assess sex-specific responses to EMPA. Clinical data suggest that the cardioprotective effects of SGLT2 inhibitors are less pronounced in women, with smaller reductions in major adverse

cardiovascular events (MACE) in women with diabetes[237] and a diminished benefit on cardiovascular death and heart failure (HF) hospitalizations in women with HF compared to men[238]. These differences may reflect true biological sex-based variability or may stem from the underrepresentation of women in clinical trials[238]. Given that women typically have greater total body fat percentage and distinct fat distribution, including females is crucial in future studies and may uncover sex-specific EAT quantity and quality changes and provide insight into differential therapeutic responsiveness[238,239].

5.2.3 Role of macrophage-NOS2 in cardiometabolic HFpEF

Chapter 4 identified macrophage-derived NOS2 as a key contributor to coronary microvascular dysfunction in cardiometabolic HFpEF. However, several questions remain. First, although this work demonstrated preserved vasodilation in macrophage-specific NOS2 knockout mice, the downstream mechanisms by which NOS2 impairs microvascular function remain unclear. Further investigation is needed to determine how NOS2-derived reactive nitrogen species affect microvascular structure, signaling, and inflammatory pathways in the context of metabolic disease. Second, NOS2 is also expressed in other cell types, including adipocytes, vascular smooth muscle cells, and cardiomyocytes. Future studies using cell type–specific knockout models could clarify the relative contributions of these sources to nitrosative stress and to both vascular and myocardial dysfunction in HFpEF.

5.3 Conclusions

In conclusion, the studies presented in this dissertation highlight the potential of CMR to noninvasively assess EAT quality in the context of cardiometabolic disease. By integrating imaging with cellular and molecular analyses, this work aimed to understand how changes in the physical properties of adipose tissue relate to underlying tissue structure, biology, and function.

Additionally, these findings offer insight into how SGLT2 inhibition may modulate the inflammatory phenotype of EAT and improve microvascular function, and identify macrophage-derived NOS2 as a contributor to coronary microvascular dysfunction, suggesting new directions for mechanistic and therapeutic investigation in cardiometabolic HFpEF.

Acknowledgements

The work presented in this dissertation would not have been possible without the support and contributions of many individuals. First, I am grateful to my advisor, Dr. Frederick Epstein, for his mentorship, guidance, and support throughout my PhD. I also thank my committee members–Drs. Craig Meyer (chair), Amit Patel, Matthew Wolf, and Shayn Peirce-Cottler–for their time, feedback, and support.

I appreciate the contributions and insight of our collaborators Drs. Matthew Wolf, Amit Patel, Brent French, and Brant Isakson. In the Wolf lab, I would especially like to thank Dr. Caitlin Pavelec for her dedication and expertise in histology, flow cytometry, and cytokine assays. I am also grateful to Dr. Frank Kober for generously providing his ASL sequence and assisting with its adaptation to our system. Additionally, I would like to thank Jack Roy for his expertise in mouse MRI as well as the UVA Molecular Imaging Core.

I am thankful to the UVA Medical Scientist Training Program for fostering a collaborative environment and supporting my dual training in research and medicine.

To the members of the Epstein lab, especially Dr. Soham Shah, Dr. Sona Ghadimi, Thomas Skacel, and Jack Echols – thank you! This work would not have been possible without their contributions and support. Importantly, their encouragement, expertise, and insights made completing this dissertation all the more enjoyable and meaningful.

Finally, I'd like to thank my friends, parents, and siblings for their unwavering support–not just over the past four years, but always.

References

1. Shah SJ, Lam CSP, Svedlund S, et al. Prevalence and correlates of coronary microvascular dysfunction in heart failure with preserved ejection fraction: PROMIS-HFpEF. *Eur Heart J*. 2018;39(37):3439-3450. doi:10.1093/eurheartj/ehy531

2. Schiattarella GG, Hill JA. Cardiometabolic HFpEF: Mechanisms and Therapies. *Cardiometab Syndr J*. 2021;1(2):117. doi:10.51789/cmsj.2021.1.e18

3. Packer M. Epicardial Adipose Tissue May Mediate Deleterious Effects of Obesity and Inflammation on the Myocardium. *J Am Coll Cardiol*. 2018;71(20):2360-2372. doi:10.1016/j.jacc.2018.03.509

4. Nishimura D. *Principles of Magnetic Resonance Imaging*.; 2010.

5. Bloembergen N, Purcell E, Pound R. Relaxation Effects in Nuclear Magnetic Resonance Absorption. *Pysical Review*. 1948;73(7).

6. Bloch F. Nuclear Induction. *Phys Rev*. 1946;70(7-8):460-474. doi:10.1103/PhysRev.70.460

7. Chavhan GB, Babyn PS, Thomas B, Shroff MM, Haacke EM. Principles, Techniques, and Applications of T2*-based MR Imaging and Its Special Applications. *RadioGraphics*. 2009;29(5):1433-1449. doi:10.1148/rg.295095034

8. Mezrich R. A perspective on K-space. *Radiology*. 1995;195(2):297-315. doi:10.1148/radiology.195.2.7724743

9. Feng L. Golden-Angle Radial MRI: Basics, Advances, and Applications. *J Magn Reson Imaging*. 2022;56(1):45-62. doi:10.1002/jmri.28187

10. Zhou Z, Han F, Yan L, Wang DJJ, Hu P. Golden-ratio rotated stack-of-stars acquisition for improved volumetric MRI. *Magnetic Resonance in Medicine*. 2017;78(6):2290-2298. doi:10.1002/mrm.26625

11. Markl M, Leupold J. Gradient echo imaging. *Magnetic Resonance Imaging*. 2012;35(6):1274-1289. doi:10.1002/jmri.23638

12. Bydder GM, Hajnal JV, Young IR. MRI: Use of the inversion recovery pulse sequence. *Clinical Radiology*. 1998;53(3):159-176. doi:10.1016/S0009-9260(98)80096-2

13. Look DC, Locker DR. Time Saving in Measurement of NMR and EPR Relaxation Times. *Review of Scientific Instruments*. 1970;41(2):250-251. doi:10.1063/1.1684482

14. Deichmann R, Haase A. Quantification of Tl Valuesby SNAPSHOT-FLASH NMR Imaging.

15. Messroghli DR, Radjenovic A, Kozerke S, Higgins DM, Sivananthan MU, Ridgway JP. Modified Look-Locker inversion recovery (MOLLI) for high-resolutionT1 mapping of the heart. *Magn Reson Med*. 2004;52(1):141-146. doi:10.1002/mrm.20110

16. Reiter G, Reiter C, Kräuter C, Fuchsjäger M, Reiter U. Cardiac magnetic resonance T1 mapping. Part 1: Aspects of acquisition and evaluation. *European Journal of Radiology*. 2018;109:223-234. doi:10.1016/j.ejrad.2018.10.011

17. Bley TA, Wieben O, François CJ, Brittain JH, Reeder SB. Fat and water magnetic resonance imaging. *Magnetic Resonance Imaging*. 2010;31(1):4-18. doi:10.1002/jmri.21895

18. Dixon WT. Simple proton spectroscopic imaging. *Radiology*. 1984;153(1):189-194. doi:10.1148/radiology.153.1.6089263

19. Glover GH, Schneider E. Three-point dixon technique for true water/fat decomposition with B_0 inhomogeneity correction. *Magnetic Resonance in Med*. 1991;18(2):371-383. doi:10.1002/mrm.1910180211

20. Reeder SB, Hu HH, Sirlin CB. Proton density fat-fraction: A standardized mr-based biomarker of tissue fat concentration. *Magnetic Resonance Imaging*. 2012;36(5):1011-1014. doi:10.1002/jmri.23741

21. Wang X, Hernando D, Reeder SB. Sensitivity of chemical shift-encoded fat quantification to calibration of fat MR spectrum. *Magnetic Resonance in Med*. 2016;75(2):845-851. doi:10.1002/mrm.25681

22. Hamilton G, Yokoo T, Bydder M, et al. In vivo characterization of the liver fat 1H MR spectrum. *NMR Biomed*. 2011;24(7):10.1002/nbm.1622. doi:10.1002/nbm.1622

23. Reeder SB, Robson PM, Yu H, et al. Quantification of hepatic steatosis with MRI: The effects of accurate fat spectral modeling. *Magnetic Resonance Imaging*. 2009;29(6):1332-1339. doi:10.1002/jmri.21751

24. Leporq B, Lambert SA, Ronot M, Vilgrain V, Van Beers BE. Quantification of the triglyceride fatty acid composition with 3.0 T MRI. *NMR in Biomedicine*. 2014;27(10):1211-1221. doi:10.1002/nbm.3175

25. Leporq B, Lambert SA, Ronot M, Vilgrain V, Van Beers BE. Simultaneous MR quantification of hepatic fat content, fatty acid composition, transverse relaxation time and magnetic susceptibility for the diagnosis of non-alcoholic steatohepatitis. *NMR in Biomedicine*. 2017;30(10):e3766. doi:10.1002/nbm.3766

26. Martel D, Leporq B, Saxena A, et al. 3T chemical shift-encoded MRI: Detection of altered proximal femur marrow adipose tissue composition in glucocorticoid users and validation with magnetic resonance spectroscopy. *J Magn Reson Imaging*. 2019;50(2):490-496. doi:10.1002/jmri.26586

27. Martel D, Leporq B, Bruno M, Regatte RR, Honig S, Chang G. Chemical shift-encoded MRI for assessment of bone marrow adipose tissue fat composition: Pilot study in premenopausal versus postmenopausal women. *Magnetic Resonance Imaging*. 2018;53:148-155. doi:10.1016/j.mri.2018.07.001

28. Echols JT, Wang S, Patel AR, Hogwood AC, Abbate A, Epstein FH. Fatty acid composition MRI of epicardial adipose tissue: Methods and detection of proinflammatory biomarkers in ST-segment elevation myocardial infarction patients. *Magn Reson Med*. 2024;93(2):513-535. doi:10.1002/mrm.30285

29. Schneider M, Janas G, Lugauer F, et al. Accurate fatty acid composition estimation of adipose tissue in the abdomen based on bipolar multi-echo MRI. *Magn Reson Med*. 2019;81(4):2330-2346. doi:10.1002/mrm.27557

30. Leporq B, Lambert SA, Ronot M, et al. Hepatic fat fraction and visceral adipose tissue fatty acid composition in mice: Quantification with 7.0T MRI: Quantification of Fat and Fatty Acid Composition in Mice with 7.0T MRI. *Magn Reson Med*. 2016;76(2):510-518. doi:10.1002/mrm.25895

31. Shah SA, Echols JT, Sun C, Wolf MJ, Epstein FH. Accelerated fatty acid composition MRI of epicardial adipose tissue: Development and application to eplerenone treatment in a mouse model of obesity-induced coronary microvascular disease. *Magn Reson Med*. 2022;88(4):1734-1747. doi:10.1002/mrm.29348

32. Tsao CW, Aday AW, Almarzooq ZI, et al. Heart Disease and Stroke Statistics—2023 Update: A Report From the American Heart Association. *Circulation*. 2023;147(8). doi:10.1161/CIR.0000000000001123

33. Vasan RS, Xanthakis V, Lyass A, et al. Epidemiology of Left Ventricular Systolic Dysfunction and Heart Failure in the Framingham Study. *JACC: Cardiovascular Imaging*. 2018;11(1):1-11. doi:10.1016/j.jcmg.2017.08.007

34. Redfield MM, Borlaug BA. Heart Failure With Preserved Ejection Fraction: A Review. *JAMA*. 2023;329(10):827. doi:10.1001/jama.2023.2020

35. Borlaug BA, Lam CSP, Roger VL, Rodeheffer RJ, Redfield MM. Contractility and Ventricular Systolic Stiffening in Hypertensive Heart Disease. *Journal of the American College of Cardiology*. 2009;54(5):410-418. doi:10.1016/j.jacc.2009.05.013

36. Paulus WJ, Zile MR. From Systemic Inflammation to Myocardial Fibrosis: The Heart Failure With Preserved Ejection Fraction Paradigm Revisited. *Circulation Research*. 2021;128(10):1451-1467. doi:10.1161/CIRCRESAHA.121.318159

37. Taqueti VR, Di Carli MF. Coronary Microvascular Disease Pathogenic Mechanisms and Therapeutic Options. *Journal of the American College of Cardiology*. 2018;72(21):2625-2641. doi:10.1016/j.jacc.2018.09.042

38. Sinha A, Rahman H, Perera D. Coronary microvascular dysfunction and heart failure with preserved ejection fraction: what are the mechanistic links? *Curr Opin Cardiol*. 2023;38(6):521-526. doi:10.1097/HCO.0000000000001082

39. Ayub MT, Kalra D. Coronary Microvascular Dysfunction and the Role of Noninvasive Cardiovascular Imaging. *Diagnostics*. 2020;10(9):679. doi:10.3390/diagnostics10090679

40. Sinha A, Rahman H, Webb A, Shah AM, Perera D. Untangling the pathophysiologic link between coronary microvascular dysfunction and heart failure with preserved ejection fraction. *European Heart Journal*. 2021;42(43):4431-4441. doi:10.1093/eurheartj/ehab653

41. Taqueti VR, Solomon SD, Shah AM, et al. Coronary microvascular dysfunction and future risk of heart failure with preserved ejection fraction. *European Heart Journal*. 2018;39(10):840-849. doi:10.1093/eurheartj/ehx721

42. Arnold JR, Kanagala P, Budgeon CA, et al. Prevalence and Prognostic Significance of Microvascular Dysfunction in Heart Failure With Preserved Ejection Fraction. *JACC: Cardiovascular Imaging*. 2022;15(6):1001-1011. doi:10.1016/j.jcmg.2021.11.022

43. Paulus WJ, Tschöpe C. A Novel Paradigm for Heart Failure With Preserved Ejection Fraction. *Journal of the American College of Cardiology*. 2013;62(4):263-271. doi:10.1016/j.jacc.2013.02.092

44. Mohammed SF, Hussain S, Mirzoyev SA, Edwards WD, Maleszewski JJ, Redfield MM. Coronary Microvascular Rarefaction and Myocardial Fibrosis in Heart Failure With Preserved Ejection Fraction. *Circulation*. 2015;131(6):550-559. doi:10.1161/CIRCULATIONAHA.114.009625

45. Pérez-Torres I, Manzano-Pech L, Rubio-Ruíz ME, Soto ME, Guarner-Lans V. Nitrosative Stress and Its Association with Cardiometabolic Disorders. *Molecules*. 2020;25(11):2555. doi:10.3390/molecules25112555

46. Lee S, Kwak C, Lee S, et al. Anti-Inflammatory Effect of Ascochlorin in LPS-Stimulated RAW 264.7 Macrophage Cells Is Accompanied With the Down-Regulation of iNOS, COX-2 and Proinflammatory Cytokines Through NF-κB, ERK1/2, and p38 Signaling Pathway. *J of Cellular Biochemistry*. 2016;117(4):978-987. doi:10.1002/jcb.25383

47. Yasukawa T, Tokunaga E, Ota H, Sugita H, Martyn JAJ, Kaneki M. S-Nitrosylation-dependent Inactivation of Akt/Protein Kinase B in Insulin Resistance. *Journal of Biological Chemistry*. 2005;280(9):7511-7518. doi:10.1074/jbc.M411871200

48. Lind M, Hayes A, Caprnda M, et al. Inducible nitric oxide synthase: Good or bad? *Biomedicine & Pharmacotherapy*. 2017;93:370-375. doi:10.1016/j.biopha.2017.06.036

49. Soskic SS. Regulation of Inducible Nitric Oxide Synthase (iNOS) and its Potential Role in Insulin Resistance, Diabetes and Heart Failure. *TOCMJ*. 2011;5(1):153-163. doi:10.2174/1874192401105010153

50. Ozbayer C, Kebapci MN, Kurt H, Colak E, Gunes HV, Degirmenci I. Potential associations between variants of genes encoding regulators of inflammation, and mediators of inflammation in type 2 diabetes and insulin resistance. *J Clin Pharm Ther*. 2021;46(5):1395-1403. doi:10.1111/jcpt.13471

51. Schiattarella GG, Altamirano F, Tong D, et al. Nitrosative stress drives heart failure with preserved ejection fraction. *Nature*. 2019;568(7752):351-356. doi:10.1038/s41586-019-1100-z

52. Yang L, Calay ES, Fan J, et al. S-Nitrosylation links obesity-associated inflammation to endoplasmic reticulum dysfunction. *Science*. 2015;349(6247):500-506. doi:10.1126/science.aaa0079

53. Shah SA, Reagan CE, Bresticker JE, et al. Obesity-Induced Coronary Microvascular Disease Is Prevented by iNOS Deletion and Reversed by iNOS Inhibition. *JACC: Basic to Translational Science*. 2023;8(5):501-514. doi:10.1016/j.jacbts.2022.11.005

54. Oeser C. Nitrates reduce activity levels in HFpEF. *Nat Rev Cardiol*. 2016;13(1):2-3. doi:10.1038/nrcardio.2015.176

55. Redfield MM, Anstrom KJ, Levine JA, et al. Isosorbide Mononitrate in Heart Failure with Preserved Ejection Fraction. *N Engl J Med*. 2015;373(24):2314-2324. doi:10.1056/NEJMoa1510774

56. Ward ZJ, Bleich SN, Cradock AL, et al. Projected U.S. State-Level Prevalence of Adult Obesity and Severe Obesity. *N Engl J Med*. 2019;381(25):2440-2450. doi:10.1056/NEJMsa1909301

57. Cohen JB, Schrauben SJ, Zhao L, et al. Clinical Phenogroups in Heart Failure With Preserved Ejection Fraction. *JACC: Heart Failure*. 2020;8(3):172-184. doi:10.1016/j.jchf.2019.09.009

58. Capone F, Vettor R, Schiattarella GG. Cardiometabolic HFpEF: NASH of the Heart. *Circulation*. 2023;147(6):451-453. doi:10.1161/CIRCULATIONAHA.122.062874

59. Ibrahim MM. Subcutaneous and visceral adipose tissue: structural and functional differences. *Obesity Reviews*. 2010;11(1):11-18. doi:10.1111/j.1467-789X.2009.00623.x

60. Fox CS, Massaro JM, Hoffmann U, et al. Abdominal Visceral and Subcutaneous Adipose Tissue Compartments: Association With Metabolic Risk Factors in the Framingham Heart Study. *Circulation*. 2007;116(1):39-48. doi:10.1161/CIRCULATIONAHA.106.675355

61. Peikert A, Vaduganathan M, Claggett BL, et al. Near-universal prevalence of central adiposity in heart failure with preserved ejection fraction: the PARAGON-HF trial. *Eur Heart J*. January 2025:ehaf057. doi:10.1093/eurheartj/ehaf057

62. Blüher M. Adipose Tissue Dysfunction in Obesity. *Exp Clin Endocrinol Diabetes*. 2009;117(06):241-250. doi:10.1055/s-0029-1192044

63. Cinti S, Mitchell G, Barbatelli G, et al. Adipocyte death defines macrophage localization and function in adipose tissue of obese mice and humans. *Journal of Lipid Research*. 2005;46(11):2347-2355. doi:10.1194/jlr.M500294-JLR200

64. Nance SA, Muir L, Lumeng C. Adipose tissue macrophages: Regulators of adipose tissue immunometabolism during obesity. *Molecular Metabolism*. 2022;66:101642. doi:10.1016/j.molmet.2022.101642

65. Morgan PK, Huynh K, Pernes G, et al. Macrophage polarization state affects lipid composition and the channeling of exogenous fatty acids into endogenous lipid pools. *Journal of Biological Chemistry*. 2021;297(6):101341. doi:10.1016/j.jbc.2021.101341

66. van Woerden G, van Veldhuisen DJ, Westenbrink BD, de Boer RA, Rienstra M, Gorter TM. Connecting epicardial adipose tissue and heart failure with preserved ejection fraction: mechanisms, management and modern perspectives. *European J of Heart Fail*. November 2022:ejhf.2741. doi:10.1002/ejhf.2741

67. Iacobellis G. Epicardial adipose tissue in contemporary cardiology. *Nat Rev Cardiol*. March 2022. doi:10.1038/s41569-022-00679-9

68. Fitzgibbons TP, Kogan S, Aouadi M, Hendricks GM, Straubhaar J, Czech MP. Similarity of mouse perivascular and brown adipose tissues and their resistance to diet-induced inflammation. *American Journal of Physiology-Heart and Circulatory Physiology*. 2011;301(4):H1425-H1437. doi:10.1152/ajpheart.00376.2011

69. Gaborit B, Sengenes C, Ancel P, Jacquier A, Dutour A. Role of Epicardial Adipose Tissue in Health and Disease: A Matter of Fat? In: Terjung R, ed. *Comprehensive Physiology*. 1st ed. Wiley; 2017:1051-1082. doi:10.1002/cphy.c160034

70. Skurk T, Alberti-Huber C, Herder C, Hauner H. Relationship between Adipocyte Size and Adipokine Expression and Secretion. *The Journal of Clinical Endocrinology & Metabolism*. 2007;92(3):1023-1033. doi:10.1210/jc.2006-1055

71. Walker ME, Matthan NR, Goldbaum A, et al. Dietary patterns influence epicardial adipose tissue fatty acid composition and inflammatory gene expression in the Ossabaw pig. *J Nutr Biochem*. 2019;70:138-146. doi:10.1016/j.jnutbio.2019.04.013

72. McKernan K, Varghese M, Patel R, Singer K. Role of TLR4 in the induction of inflammatory changes in adipocytes and macrophages. *Adipocyte*. 2020;9(1):212-222. doi:10.1080/21623945.2020.1760674

73. Lee JY, Sohn KH, Rhee SH, Hwang D. Saturated Fatty Acids, but Not Unsaturated Fatty Acids, Induce the Expression of Cyclooxygenase-2 Mediated through Toll-like Receptor 4. *Journal of Biological Chemistry*. 2001;276(20):16683-16689. doi:10.1074/jbc.M011695200

74. Gruzdeva OV, Akbasheva OE, Dyleva YuA, et al. Adipokine and Cytokine Profiles of Epicardial and Subcutaneous Adipose Tissue in Patients with Coronary Heart Disease. *Bull Exp Biol Med*. 2017;163(5):608-611. doi:10.1007/s10517-017-3860-5

75. Ravaut G, Légiot A, Bergeron KF, Mounier C. Monounsaturated Fatty Acids in Obesity-Related Inflammation. *Int J Mol Sci*. 2020;22(1):330. doi:10.3390/ijms22010330

76. Pezeshkian M, Noori M, Najjarpour-Jabbari H, et al. Fatty Acid Composition of Epicardial and Subcutaneous Human Adipose Tissue. *Metabolic Syndrome and Related Disorders*. 2009;7(2):125-132. doi:10.1089/met.2008.0056

77. Ravaut G, Légiot A, Bergeron KF, Mounier C. Monounsaturated Fatty Acids in Obesity-Related Inflammation. *IJMS*. 2020;22(1):330. doi:10.3390/ijms22010330

78. Van Woerden G, Van Veldhuisen DJ, Gorter TM, et al. Importance of epicardial adipose tissue localization using cardiac magnetic resonance imaging in patients with heart failure with mid-range and preserved ejection fraction. *Clinical Cardiology*. 2021;44(7):987-993. doi:10.1002/clc.23644

79. Van Woerden G, Gorter TM, Westenbrink BD, Willems TP, Van Veldhuisen DJ, Rienstra M. Epicardial fat in heart failure patients with mid-range and preserved ejection fraction. *European J of Heart Fail*. 2018;20(11):1559-1566. doi:10.1002/ejhf.1283

80. Obokata M, Kagami K. Epicardial Adipose Tissue in Obese Heart Failure With Preserved Ejection Fraction. *JACC: Advances*. 2023;2(10):100731. doi:10.1016/j.jacadv.2023.100731

81. Kenchaiah S, Ding J, Carr JJ, et al. Pericardial Fat and the Risk of Heart Failure. *Journal of the American College of Cardiology*. 2021;77(21):2638-2652. doi:10.1016/j.jacc.2021.04.003

82. van Woerden G, van Veldhuisen DJ, Manintveld OC, et al. Epicardial Adipose Tissue and Outcome in Heart Failure With Mid-Range and Preserved Ejection Fraction. *Circ: Heart Failure*. 2022;15(3):e009238. doi:10.1161/CIRCHEARTFAILURE.121.009238

83. Nakamori S, Kucukseymen S, Rodriguez J, et al. Obesity-Related Differences in Pathomechanism and Outcomes in Patients With HFpEF. *JACC: Advances*. 2023;2(10):100730. doi:10.1016/j.jacadv.2023.100730

84. Abusnina W, Merdler I, Cellamare M, et al. Epicardial Fat Tissue: A Potential Marker for Coronary Microvascular Dysfunction. *JAHA*. 2025;14(3):e038484. doi:10.1161/JAHA.124.038484

85. Wu C, Lee J, Hsu J, et al. Myocardial adipose deposition and the development of heart failure with preserved ejection fraction. *European J of Heart Fail*. 2020;22(3):445-454. doi:10.1002/ejhf.1617

86. Goldman SA, Requena -Ibanez Juan Antonio, Devesa A, Santos -Gallego Carlos G., Badimon JJ, Fuster V. Uncovering the Role of Epicardial Adipose Tissue in Heart Failure With Preserved Ejection Fraction. *JACC: Advances*. 2023;2(9):100657. doi:10.1016/j.jacadv.2023.100657

87. Bucerius J, Mani V, Wong S, et al. Arterial and fat tissue inflammation are highly correlated : a prospective 18F-FDG PET/CT study. *Eur J Nucl Med Mol Imaging*. 2014;41(5):934-945. doi:10.1007/s00259-013-2653-y

88. Spearman JV, Renker M, Schoepf UJ, et al. Prognostic value of epicardial fat volume measurements by computed tomography: a systematic review of the literature. *Eur Radiol*. 2015;25(11):3372-3381. doi:10.1007/s00330-015-3765-5

89. Franssens BT, Nathoe HM, Leiner T, Van Der Graaf Y, Visseren FL. Relation between cardiovascular disease risk factors and epicardial adipose tissue density on cardiac computed tomography in patients at high risk of cardiovascular events. *Eur J Prev Cardiolog*. 2017;24(6):660-670. doi:10.1177/2047487316679524

90. Antonopoulos AS, Sanna F, Sabharwal N, et al. Detecting human coronary inflammation by imaging perivascular fat. *Sci Transl Med*. 2017;9(398):eaal2658. doi:10.1126/scitranslmed.aal2658

91. Nogajski Ł, Mazuruk M, Kacperska M, et al. Epicardial fat density obtained with computed tomography imaging - more important than volume? *Cardiovasc Diabetol*. 2024;23(1):389. doi:10.1186/s12933-024-02474-x

92. Garnov N, Linder N, Schaudinn A, et al. Comparison of T1 relaxation times in adipose tissue of severely obese patients and healthy lean subjects measured by 1.5 T MRI: T1 relaxation times in adipose tissue. *NMR Biomed*. 2014;27(9):1123-1128. doi:10.1002/nbm.3166

93. Cowie MR, Fisher M. SGLT2 inhibitors: mechanisms of cardiovascular benefit beyond glycaemic control. *Nat Rev Cardiol*. 2020;17(12):761-772. doi:10.1038/s41569-020-0406-8

94. Wright EM, Loo DDF, Hirayama BA. Biology of Human Sodium Glucose Transporters. *Physiological Reviews*. 2011;91(2):733-794. doi:10.1152/physrev.00055.2009

95. Rieg T, Masuda T, Gerasimova M, et al. Increase in SGLT1-mediated transport explains renal glucose reabsorption during genetic and pharmacological SGLT2 inhibition in euglycemia. *American Journal of Physiology-Renal Physiology*. 2014;306(2):F188-F193. doi:10.1152/ajprenal.00518.2013

96. Zinman B, Wanner C, Lachin JM, et al. Empagliflozin, Cardiovascular Outcomes, and Mortality in Type 2 Diabetes. *N Engl J Med*. 2015;373(22):2117-2128. doi:10.1056/NEJMoa1504720

97. Solomon SD, McMurray JJV, Claggett B, et al. Dapagliflozin in Heart Failure with Mildly Reduced or Preserved Ejection Fraction. *N Engl J Med*. 2022;387(12):1089-1098. doi:10.1056/NEJMoa2206286

98. Anker SD, Butler J, Filippatos G, et al. Empagliflozin in Heart Failure with a Preserved Ejection Fraction. *N Engl J Med*. 2021;385(16):1451-1461. doi:10.1056/NEJMoa2107038

99. Pandey AK, Bhatt DL, Pandey A, et al. Mechanisms of benefits of sodium-glucose cotransporter 2 inhibitors in heart failure with preserved ejection fraction. *European Heart Journal*. 2023;44(37):3640-3651. doi:10.1093/eurheartj/ehad389

100. Bonora BM, Avogaro A, Fadini GP. Extraglycemic Effects of SGLT2 Inhibitors: A Review of the Evidence. *DMSO*. 2020;Volume 13:161-174. doi:10.2147/DMSO.S233538

101. Packer M. Heart Failure: The Most Important, Preventable, and Treatable Cardiovascular Complication of Type 2 Diabetes. *Diabetes Care*. 2018;41(1):11-13. doi:10.2337/dci17-0052

102. Packer M. Critical examination of mechanisms underlying the reduction in heart failure events with SGLT2 inhibitors: identification of a molecular link between their actions to stimulate erythrocytosis and to alleviate cellular stress. *Cardiovascular Research*. 2021;117(1):74-84. doi:10.1093/cvr/cvaa064

103. Packer M, Anker SD, Butler J, et al. Empagliflozin in Patients With Heart Failure, Reduced Ejection Fraction, and Volume Overload. *Journal of the American College of Cardiology*. 2021;77(11):1381-1392. doi:10.1016/j.jacc.2021.01.033

104. Masson W, Lavalle-Cobo A, Nogueira JP. Effect of SGLT2-Inhibitors on Epicardial Adipose Tissue: A Meta-Analysis. *Cells*. 2021;10(8):2150. doi:10.3390/cells10082150

105. Hoong CWS, Chua MWJ. SGLT2 Inhibitors as Calorie Restriction Mimetics: Insights on Longevity Pathways and Age-Related Diseases. *Endocrinology*. 2021;162(8):bqab079. doi:10.1210/endocr/bqab079

106. Packer M. Autophagy stimulation and intracellular sodium reduction as mediators of the cardioprotective effect of sodium–glucose cotransporter 2 inhibitors. *European J of Heart Fail*. 2020;22(4):618-628. doi:10.1002/ejhf.1732

107. Packer M. How can sodium–glucose cotransporter 2 inhibitors stimulate erythrocytosis in patients who are iron-deficient? Implications for understanding iron homeostasis in heart failure. *European J of Heart Fail*. 2022;24(12):2287-2296. doi:10.1002/ejhf.2731

108. Anand IS, Gupta P. Anemia and Iron Deficiency in Heart Failure: Current Concepts and Emerging Therapies. *Circulation*. 2018;138(1):80-98. doi:10.1161/CIRCULATIONAHA.118.030099

109. Nickel A, Loffler J, Maack C. Myocardial energetics in heart failure. *Basic Res Cardiol*. 2013.

110. Wu P, Wen W, Li J, et al. Systematic Review and Meta-Analysis of Randomized Controlled Trials on the Effect of SGLT2 Inhibitor on Blood Leptin and Adiponectin Level in Patients with Type 2 Diabetes. *Horm Metab Res*. 2019;51(08):487-494. doi:10.1055/a-0958-2441

111. Takano M, Kondo H, Harada T, et al. Empagliflozin Suppresses the Differentiation/Maturation of Human Epicardial Preadipocytes and Improves Paracrine Secretome Profile. *JACC Basic Transl Sci*. 2023;8(9):1081-1097. doi:10.1016/j.jacbts.2023.05.007

112. Miyachi Y, Tsuchiya K, Shiba K, et al. A reduced M1-like/M2-like ratio of macrophages in healthy adipose tissue expansion during SGLT2 inhibition. *Sci Rep*. 2018;8(1):16113. doi:10.1038/s41598-018-34305-x

113. Chen S, Coronel R, Hollmann MW, Weber NC, Zuurbier CJ. Direct cardiac effects of SGLT2 inhibitors. *Cardiovascular Diabetology*. 2022;21(1):45. doi:10.1186/s12933-022-01480-1

114. Tong Y, Wang Z, Cai L, Lin L, Liu J, Cheng J. NLRP3 Inflammasome and Its Central Role in the Cardiovascular Diseases. *Oxidative Medicine and Cellular Longevity*. 2020;2020:1-8. doi:10.1155/2020/4293206

115. Byrne NJ, Matsumura N, Maayah ZH, et al. Empagliflozin Blunts Worsening Cardiac Dysfunction Associated With Reduced NLRP3 (Nucleotide-Binding Domain-Like Receptor Protein 3) Inflammasome Activation in Heart Failure. *Circ: Heart Failure*. 2020;13(1):e006277. doi:10.1161/CIRCHEARTFAILURE.119.006277

116. Di Franco A, Cantini G, Tani A, et al. Sodium-dependent glucose transporters (SGLT) in human ischemic heart: A new potential pharmacological target. *International Journal of Cardiology*. 2017;243:86-90. doi:10.1016/j.ijcard.2017.05.032

117. Verma S, Garg A, Yan AT, et al. Effect of Empagliflozin on Left Ventricular Mass and Diastolic Function in Individuals With Diabetes: An Important Clue to the EMPA-REG OUTCOME Trial? *Diabetes Care*. 2016;39(12):e212-e213. doi:10.2337/dc16-1312

118. Shim CY, Seo J, Cho I, et al. Randomized, Controlled Trial to Evaluate the Effect of Dapagliflozin on Left Ventricular Diastolic Function in Patients With Type 2 Diabetes Mellitus. *Circulation*. 2021;143(5):510-512. doi:10.1161/CIRCULATIONAHA.120.051992

119. Zile MR, Baicu CF, S. Ikonomidis J, et al. Myocardial Stiffness in Patients With Heart Failure and a Preserved Ejection Fraction: Contributions of Collagen and Titin. *Circulation*. 2015;131(14):1247-1259. doi:10.1161/CIRCULATIONAHA.114.013215

120. LeWinter MM, Granzier H. Cardiac Titin: A Multifunctional Giant. *Circulation*. 2010;121(19):2137-2145. doi:10.1161/CIRCULATIONAHA.109.860171

121. Withaar C, Lam CSP, Schiattarella GG, De Boer RA, Meems LMG. Heart failure with preserved ejection fraction in humans and mice: embracing clinical complexity in mouse models. *European Heart Journal*. 2021;42(43):4420-4430. doi:10.1093/eurheartj/ehab389

122. Valero-Muñoz M, Backman W, Sam F. Murine Models of Heart Failure With Preserved Ejection Fraction. *JACC: Basic to Translational Science*. 2017;2(6):770-789. doi:10.1016/j.jacbts.2017.07.013

123. Ichihara S, Senbonmatsu T, Price E, Ichiki T, Gaffney FA, Inagami T. Angiotensin II Type 2 Receptor Is Essential for Left Ventricular Hypertrophy and Cardiac Fibrosis in Chronic Angiotensin II–Induced Hypertension. *Circulation*. 2001;104(3):346-351. doi:10.1161/01.CIR.104.3.346

124. Glenn DJ, Cardema MC, Ni W, et al. Cardiac steatosis potentiates angiotensin II effects in the heart. *American Journal of Physiology-Heart and Circulatory Physiology*. 2015;308(4):H339-H350. doi:10.1152/ajpheart.00742.2014

125. Chen H, Charlat O, Tartaglia LA, et al. Evidence That the Diabetes Gene Encodes the Leptin Receptor: Identification of a Mutation in the Leptin Receptor Gene in db/db Mice. *Cell*. 1996;84(3):491-495. doi:10.1016/S0092-8674(00)81294-5

126. Reil JC, Hohl M, Reil GH, et al. Heart rate reduction by If-inhibition improves vascular stiffness and left ventricular systolic and diastolic function in a mouse model of heart failure with preserved ejection fraction. *European Heart Journal*. 2013;34(36):2839-2849. doi:10.1093/eurheartj/ehs218

127. Barouch LA, Berkowitz DE, Harrison RW, O'Donnell CP, Hare JM. Disruption of Leptin Signaling Contributes to Cardiac Hypertrophy Independently of Body Weight in Mice. *Circulation*. 2003;108(6):754-759. doi:10.1161/01.CIR.0000083716.82622.FD

128. Lindström P. The Physiology of Obese-Hyperglycemic Mice [*ob/ob* Mice]. *The Scientific World JOURNAL*. 2007;7:666-685. doi:10.1100/tsw.2007.117

129. Roh JD, Houstis N, Yu A, et al. Exercise training reverses cardiac aging phenotypes associated with heart failure with preserved ejection fraction in male mice. *Aging Cell*. 2020;19(6):e13159. doi:10.1111/acel.13159

130. Aurich AC, Niemann B, Pan R, et al. Age-dependent effects of high fat-diet on murine left ventricles: role of palmitate. *Basic Res Cardiol*. 2013;108(5):369. doi:10.1007/s00395-013-0369-6

131. Hariri N, Thibault L. High-fat diet-induced obesity in animal models. *Nutr Res Rev*. 2010;23(2):270-299. doi:10.1017/S0954422410000168

132. Meng Q, Lai YC, Kelly NJ, et al. Development of a Mouse Model of Metabolic Syndrome, Pulmonary Hypertension, and Heart Failure with Preserved Ejection Fraction. *Am J Respir Cell Mol Biol*. 2017;56(4):497-505. doi:10.1165/rcmb.2016-0177OC

133. Piek A, Koonen DPY, Schouten EM, et al. Pharmacological myeloperoxidase (MPO) inhibition in an obese/hypertensive mouse model attenuates obesity and liver damage, but not cardiac remodeling. *Sci Rep*. 2019;9(1):18765. doi:10.1038/s41598-019-55263-y

134. Aimaretti E, Chimienti G, Rubeo C, et al. Different Effects of High-Fat/High-Sucrose and High-Fructose Diets on Advanced Glycation End-Product Accumulation and on Mitochondrial Involvement in Heart and Skeletal Muscle in Mice. *Nutrients*. 2023;15(23):4874. doi:10.3390/nu15234874

135. Price AN. Cardiovascular Magnetic Resonance Imaging in Experimental Models. *TOCMJ*. 2010;4(1):278-292. doi:10.2174/1874192401004010278

136. Berr SS, Roy RJ, French BA, et al. Black blood gradient echo cine magnetic resonance imaging of the mouse heart. *Magnetic Resonance in Med*. 2005;53(5):1074-1079. doi:10.1002/mrm.20487

137. Van Laar PJ, Van Der Grond J, Hendrikse J. Brain Perfusion Territory Imaging: Methods and Clinical Applications of Selective Arterial Spin-labeling MR Imaging. *Radiology*. 2008;246(2):354-364. doi:10.1148/radiol.2462061775

138. Vandsburger MH, Janiczek RL, Xu Y, et al. Improved arterial spin labeling after myocardial infarction in mice using cardiac and respiratory gated look-locker imaging with fuzzy C-means clustering: ASL in Mice After Myocardial Infarction. *Magn Reson Med*. 2010;63(3):648-657. doi:10.1002/mrm.22280

139. Di Salvo G, Di Bello V, Salustri A, et al. The Prognostic Value of Early Left Ventricular Longitudinal Systolic Dysfunction in Asymptomatic Subjects With Cardiovascular Risk Factors. *Clinical Cardiology*. 2011;34(8):500-506. doi:10.1002/clc.20933

140. Kim D, Gilson WD, Kramer CM, Epstein FH. Myocardial Tissue Tracking with Two-dimensional Cine Displacement-encoded MR Imaging: Development and Initial Evaluation. *Radiology*. 2004;230(3):862-871. doi:10.1148/radiol.2303021213

141. Ghadimi S, Abdi M, Epstein FH. Improved computation of Lagrangian tissue displacement and strain for cine DENSE MRI using a regularized spatiotemporal least squares method. *Front Cardiovasc Med*. 2023;10. doi:10.3389/fcvm.2023.1095159

142. Smiseth OA, Rider O, Cvijic M, Valkovič L, Remme EW, Voigt JU. Myocardial Strain Imaging. *JACC: Cardiovascular Imaging*. 2025;18(3):340-381. doi:10.1016/j.jcmg.2024.07.011

143. Haggerty CM, Kramer SP, Binkley CM, et al. Reproducibility of cine displacement encoding with stimulated echoes (DENSE) cardiovascular magnetic resonance for measuring left ventricular strains, torsion, and synchrony in mice. *Journal of Cardiovascular Magnetic Resonance*. 2013;15(1):71. doi:10.1186/1532-429X-15-71

144. Vandsburger MH, French BA, Kramer CM, Zhong X, Epstein FH. Displacement-encoded and manganese-enhanced cardiac MRI reveal that nNOS, not eNOS, plays a dominant role in modulating contraction and calcium influx in the mammalian heart. *American Journal of Physiology-Heart and Circulatory Physiology*. 2012;302(2):H412-H419. doi:10.1152/ajpheart.00705.2011

145. He J, Yang W, Wu W, et al. Early Diastolic Longitudinal Strain Rate at MRI and Outcomes in Heart Failure with Preserved Ejection Fraction. *Radiology*. 2021;301(3):582-592. doi:10.1148/radiol.2021210188

146. Klöting N, Blüher M. Adipocyte dysfunction, inflammation and metabolic syndrome. *Rev Endocr Metab Disord*. 2014;15(4):277-287. doi:10.1007/s11154-014-9301-0

147. Salgado-Somoza A, Teijeira-Fernández E, Fernández ÁL, González-Juanatey JR, Eiras S. Proteomic analysis of epicardial and subcutaneous adipose tissue reveals differences in proteins

involved in oxidative stress. *Am J Physiol Heart Circ Physiol*. 2010;299(1):H202-H209. doi:10.1152/ajpheart.00120.2010

148. Ralston JC, Lyons CL, Kennedy EB, Kirwan AM, Roche HM. Fatty Acids and NLRP3 Inflammasome–Mediated Inflammation in Metabolic Tissues. *Annu Rev Nutr*. 2017;37(1):77-102. doi:10.1146/annurev-nutr-071816-064836

149. Zhou H, Urso C, Jadeja V. Saturated Fatty Acids in Obesity-Associated Inflammation. *J Inflamm Res*. 2020;13:1-14. doi:10.2147/JIR.S229691

150. McMurray JJV, Solomon SD, Inzucchi SE, et al. Dapagliflozin in Patients with Heart Failure and Reduced Ejection Fraction. *N Engl J Med*. 2019;381(21):1995-2008. doi:10.1056/NEJMoa1911303

151. Xu L, Nagata N, Nagashimada M, et al. SGLT2 Inhibition by Empagliflozin Promotes Fat Utilization and Browning and Attenuates Inflammation and Insulin Resistance by Polarizing M2 Macrophages in Diet-induced Obese Mice. *EBioMedicine*. 2017;20:137-149. doi:10.1016/j.ebiom.2017.05.028

152. Taylor AJ, Salerno M, Dharmakumar R, Jerosch-Herold M. T1 Mapping. *JACC: Cardiovascular Imaging*. 2016;9(1):67-81. doi:10.1016/j.jcmg.2015.11.005

153. Nakajima H, Nakanishi N, Miyoshi T, et al. Inulin reduces visceral adipose tissue mass and improves glucose tolerance through altering gut metabolites. *Nutr Metab (Lond)*. 2022;19:50. doi:10.1186/s12986-022-00685-1

154. Bustin A, Lima da Cruz G, Jaubert O, Lopez K, Botnar RM, Prieto C. High-dimensionality undersampled patch-based reconstruction (HD-PROST) for accelerated multi-contrast MRI. *Magn Reson Med*. 2019;81(6):3705-3719. doi:10.1002/mrm.27694

155. Fessler JA. On NUFFT-based gridding for non-Cartesian MRI. *J Magn Reson*. 2007;188(2):191-195. doi:10.1016/j.jmr.2007.06.012

156. Uecker M, Lai P, Murphy MJ, et al. ESPIRiT—an eigenvalue approach to autocalibrating parallel MRI: Where SENSE meets GRAPPA. *Magn Reson Med*. 2014;71(3):990-1001. doi:10.1002/mrm.24751

157. Boyd S. Distributed Optimization and Statistical Learning via the Alternating Direction Method of Multipliers. *FNT in Machine Learning*. 2010;3(1):1-122. doi:10.1561/2200000016

158. Gavish M, Donoho DL. The Optimal Hard Threshold for Singular Values is \(4/\sqrt {3}\). *IEEE Trans Inform Theory*. 2014;60(8):5040-5053. doi:10.1109/TIT.2014.2323359

159. Berglund J, Ahlström H, Kullberg J. Model-based mapping of fat unsaturation and chain length by chemical shift imaging-phantom validation and in vivo feasibility. *Magn Reson Med*. 2012;68(6):1815-1827. doi:10.1002/mrm.24196

160. Block KT, Uecker M. Simple Method for Adaptive Gradient-Delay Compensation in Radial MRI. In: *Proceedings of the 19th Annual Meeting of ISMRM*. Montreal, Canada; 2011.

161. Peters DC, Derbyshire JA, McVeigh ER. Centering the projection reconstruction trajectory: Reducing gradient delay errors. *Magn Reson Med*. 2003;50(1):1-6. doi:10.1002/mrm.10501

162. Berglund J, Kullberg J. Three-dimensional water/fat separation and T2* estimation based on whole-image optimization—Application in breathhold liver imaging at 1.5 T. *Magn Reson Med*. 2012;67(6):1684-1693. doi:10.1002/mrm.23185

163. Zhou Wang, Bovik AC, Sheikh HR, Simoncelli EP. Image quality assessment: from error visibility to structural similarity. *IEEE Trans on Image Process*. 2004;13(4):600-612. doi:10.1109/TIP.2003.819861

164. National Research Council (U.S.), Institute for Laboratory Animal Research (U.S.), National Academies Press (U.S.), eds. *Guide for the Care and Use of Laboratory Animals*. 8th ed. Washington, D.C: National Academies Press; 2011.

165. Kaess BM, Pedley A, Massaro JM, Murabito J, Hoffmann U, Fox CS. The ratio of visceral to subcutaneous fat, a metric of body fat distribution, is a unique correlate of cardiometabolic risk. *Diabetologia*. 2012;55(10):2622-2630. doi:10.1007/s00125-012-2639-5

166. U-Din M, Ahmed BA, Syed SA, et al. Characteristics of Abdominal Visceral Adipose Tissue, Metabolic Health and the Gut Microbiome in Adults. *J Clin Endocrinol Metab*. 2024;109(3):680-690. doi:10.1210/clinem/dgad604

167. Porter SA, Massaro JM, Hoffmann U, Vasan RS, O'Donnel CJ, Fox CS. Abdominal Subcutaneous Adipose Tissue: A Protective Fat Depot? *Diabetes Care*. 2009;32(6):1068-1075. doi:10.2337/dc08-2280

168. Baiges-Gaya G, Fernández-Arroyo S, Luciano-Mateo F, et al. Hepatic metabolic adaptation and adipose tissue expansion are altered in mice with steatohepatitis induced by high-fat high sucrose diet. *J Nutr Biochem*. 2021;89:108559. doi:10.1016/j.jnutbio.2020.108559

169. Yaribeygi H, Maleki M, Reiner Ž, Jamialahmadi T, Sahebkar A. Mechanistic View on the Effects of SGLT2 Inhibitors on Lipid Metabolism in Diabetic Milieu. *J Clin Med*. 2022;11(21):6544. doi:10.3390/jcm11216544

170. Lewin AA, Storey P, Moccaldi M, Moy L, Kim SG. Fatty acid composition in mammary adipose tissue measured by Gradient-echo Spectroscopic MRI and its association with breast cancers. *Eur J Radiol*. 2019;116:205-211. doi:10.1016/j.ejrad.2019.04.024

171. Liu Y, Hamilton J, Eck B, Griswold M, Seiberlich N. Myocardial T_1 and T_2 quantification and water–fat separation using cardiac MR fingerprinting with rosette trajectories at 3T and 1.5T. *Magn Reson Med*. 2021;85(1):103-119. doi:10.1002/mrm.28404

172. Nezafat M, Nakamori S, Basha TA, Fahmy AS, Hauser T, Botnar RM. Imaging sequence for joint myocardial T_1 mapping and fat/water separation. *Magn Reson Med*. 2019;81(1):486-494. doi:10.1002/mrm.27390

173. Milotta G, Bustin A, Jaubert O, Neji R, Prieto C, Botnar RM. 3D whole-heart isotropic-resolution motion-compensated joint T_1 /T_2 mapping and water/fat imaging. *Magn Reson Med*. 2020;84(6):3009-3026. doi:10.1002/mrm.28330

174. Ostenson J, Robison RK, Brittain EL, Damon BM. Feasibility of joint mapping of triglyceride saturation and water longitudinal relaxation in a single breath hold applied to high fat-fraction adipose depots in the periclavicular anatomy. *Magn Reson Imaging*. 2023;99:58-66. doi:10.1016/j.mri.2023.02.001

175. Chavakis T, Alexaki VI, Ferrante AW. Macrophage function in adipose tissue homeostasis and metabolic inflammation. *Nat Immunol*. 2023;24(5):757-766. doi:10.1038/s41590-023-01479-0

176. Kim DH, Sandoval D, Reed JA, et al. The role of GM-CSF in adipose tissue inflammation. *Am J Physiol Endocrinol Metab*. 2008;295(5):E1038-E1046. doi:10.1152/ajpendo.00061.2008

177. Postiglione L, Montagnani S, Ladogana P, et al. Granulocyte Macrophage-Colony Stimulating Factor receptor expression on human cardiomyocytes from end-stage heart failure patients. *European J of Heart Fail*. 2006;8(6):564-570. doi:10.1016/j.ejheart.2005.12.007

178. Zouein FA, Kurdi M, Booz GW. LIF and the heart: Just Another Brick in the Wall? *European Cytokine Network*. 2013;24(1):11-19. doi:10.1684/ecn.2013.0335

179. Eiken HG, Øie E, Damås JK, et al. Myocardial gene expression of leukaemia inhibitory factor, interleukin-6 and glycoprotein 130 in end-stage human heart failure. *Eur J Clin Investigation*. 2001;31(5):389-397. doi:10.1046/j.1365-2362.2001.00795.x

180. Hirota H, Izumi M, Hamaguchi T, et al. Circulating interleukin-6 family cytokines and their receptors in patients with congestive heart failure. *Heart Vessels*. 2004;19(5). doi:10.1007/s00380-004-0770-z

181. Iyer SS, Cheng G. Role of Interleukin 10 Transcriptional Regulation in Inflammation and Autoimmune Disease. *Crit Rev Immunol*. 2012;32(1):23-63. doi:10.1615/CritRevImmunol.v32.i1.30

182. LaMarche NM, Kane H, Kohlgruber AC, Dong H, Lynch L, Brenner MB. Distinct iNKT Cell Populations Use IFNγ or ER Stress-Induced IL-10 to Control Adipose Tissue Homeostasis. *Cell Metabolism*. 2020;32(2):243-258.e6. doi:10.1016/j.cmet.2020.05.017

183. Elyasi A, Voloshyna I, Ahmed S, et al. The role of interferon-γ in cardiovascular disease: an update. *Inflamm Res*. 2020;69(10):975-988. doi:10.1007/s00011-020-01382-6

184. Bujak M, Frangogiannis NG. The role of IL-1 in the pathogenesis of heart disease. *Arch Immunol Ther Exp*. 2009;57(3):165-176. doi:10.1007/s00005-009-0024-y

185. De Rham C, Ferrari-Lacraz S, Jendly S, Schneiter G, Dayer JM, Villard J. The proinflammatory cytokines IL-2, IL-15 and IL-21 modulate the repertoire of mature human natural killer cell receptors. *Arthritis Res Ther*. 2007;9(6):R125. doi:10.1186/ar2336

186. Huber J, Kiefer FW, Zeyda M, et al. CC Chemokine and CC Chemokine Receptor Profiles in Visceral and Subcutaneous Adipose Tissue Are Altered in Human Obesity. *The Journal of Clinical Endocrinology & Metabolism*. 2008;93(8):3215-3221. doi:10.1210/jc.2007-2630

187. Aukrust P, Ueland T, Müller F, et al. Elevated Circulating Levels of C-C Chemokines in Patients With Congestive Heart Failure. *Circulation*. 1998;97(12):1136-1143. doi:10.1161/01.CIR.97.12.1136

188. Franconi F, Lemaire L, Saint-Jalmes H, Saulnier P. Tissue oxygenation mapping by combined chemical shift and T1 magnetic resonance imaging. *Magn Reson Med*. 2018;79(4):1981-1991. doi:10.1002/mrm.26857

189. Zhong Q, Liu H, Feng Y, et al. Detecting white adipose tissue browning in mice with in vivo R2∗ mapping at 9.4T MRI. *J Lipid Res*. 2025;66(2):100735. doi:10.1016/j.jlr.2024.100735

190. Kosiborod MN, Abildstrøm SZ, Borlaug BA, et al. Semaglutide in Patients with Heart Failure with Preserved Ejection Fraction and Obesity. *N Engl J Med*. 2023;389(12):1069-1084. doi:10.1056/NEJMoa2306963

191. Patel VB, Mori J, McLean BA, et al. ACE2 Deficiency Worsens Epicardial Adipose Tissue Inflammation and Cardiac Dysfunction in Response to Diet-Induced Obesity. *Diabetes*. 2016;65(1):85-95. doi:10.2337/db15-0399

192. Habibi J, Aroor AR, Sowers JR, et al. Sodium glucose transporter 2 (SGLT2) inhibition with empagliflozin improves cardiac diastolic function in a female rodent model of diabetes. *Cardiovasc Diabetol*. 2017;16:9. doi:10.1186/s12933-016-0489-z

193. Shah SA, Cui SX, Waters CD, et al. Nitroxide-enhanced MRI of cardiovascular oxidative stress. *NMR in Biomedicine*. 2020;33(9). doi:10.1002/nbm.4359

194. Capron T, Troalen T, Cozzone PJ, Bernard M, Kober F. Cine-ASL: A steady-pulsed arterial spin labeling method for myocardial perfusion mapping in mice. Part II. Theoretical model and sensitivity optimization: Cine-ASL: Theory. *Magn Reson Med*. 2013;70(5):1399-1408. doi:10.1002/mrm.24588

195. Troalen T, Capron T, Cozzone PJ, Bernard M, Kober F. Cine-ASL: A steady-pulsed arterial spin labeling method for myocardial perfusion mapping in mice. Part I. Experimental study: Cine-ASL: Experimental Study. *Magn Reson Med*. 2013;70(5):1389-1398. doi:10.1002/mrm.24565

196. Bresticker JE, Echols JT, Epstein FH. Accelerated Method for Joint Fatty Acid Composition and T1 (FACT) Mapping of Epicardial Adipose Tissue in Mice at 9.4 T. In: *Proceedings of the International Society for Magnetic Resonance in Medicine*. Singapore; 2024.

197. Echols JT, Wang S, Patel AR, Hogwood AC, Abbate A, Epstein FH. Fatty acid composition MRI of epicardial adipose tissue: Methods and detection of proinflammatory biomarkers in ST-segment elevation myocardial infarction patients. *Magn Reson Med*. 2024;93(2):519-535. doi:10.1002/mrm.30285

198. Spottiswoode BS, Zhong X, Hess AT, et al. Tracking Myocardial Motion From Cine DENSE Images Using Spatiotemporal Phase Unwrapping and Temporal Fitting. *IEEE Trans Med Imaging*. 2007;26(1):15-30. doi:10.1109/TMI.2006.884215

199. Berglund J, Skorpil M. Multi-scale graph-cut algorithm for efficient water-fat separation. *Magn Reson Med*. 2017;78(3):941-949. doi:10.1002/mrm.26479

200. Sakaguchi K, Takeda K, Maeda M, et al. Glucose area under the curve during oral glucose tolerance test as an index of glucose intolerance. *Diabetol Int*. 2015;7(1):53-58. doi:10.1007/s13340-015-0212-4

201. Billaud M, Lohman AW, Straub AC, Parpaite T, Johnstone SR, Isakson BE. Characterization of the thoracodorsal artery: morphology and reactivity. *Microcirculation*. 2012;19(4):360-372. doi:10.1111/j.1549-8719.2012.00172.x

202. Kuo L, Davis MJ, Chilian WM. Endothelium-dependent, flow-induced dilation of isolated coronary arterioles. *American Journal of Physiology-Heart and Circulatory Physiology*. 1990;259(4):H1063-H1070. doi:10.1152/ajpheart.1990.259.4.H1063

203. Stapleton PA, Minarchick VC, Cumpston AM, et al. Impairment of Coronary Arteriolar Endothelium-Dependent Dilation after Multi-Walled Carbon Nanotube Inhalation: A Time-Course Study. *Int J Mol Sci*. 2012;13(11):13781-13803. doi:10.3390/ijms131113781

204. Ackers-Johnson Matthew, Li Peter Yiqing, Holmes Andrew P., O'Brien Sian-Marie, Pavlovic Davor, Foo Roger S. A Simplified, Langendorff-Free Method for Concomitant Isolation of Viable Cardiac Myocytes and Nonmyocytes From the Adult Mouse Heart. *Circulation Research*. 2016;119(8):909-920. doi:10.1161/CIRCRESAHA.116.309202

205. Lehmann S, Linder N, Retschlag U, et al. MRI assessment of changes in adipose tissue parameters after bariatric surgery. Kaser S, ed. *PLoS ONE*. 2018;13(11):e0206735. doi:10.1371/journal.pone.0206735

206. Gaborit B, Ancel P, Abdullah AE, et al. Effect of empagliflozin on ectopic fat stores and myocardial energetics in type 2 diabetes: the EMPACEF study. *Cardiovasc Diabetol*. 2021;20(1):57. doi:10.1186/s12933-021-01237-2

207. Bouchi R, Terashima M, Sasahara Y, et al. Luseogliflozin reduces epicardial fat accumulation in patients with type 2 diabetes: a pilot study. *Cardiovasc Diabetol*. 2017;16(1):32. doi:10.1186/s12933-017-0516-8

208. Fukuda T, Bouchi R, Terashima M, et al. Ipragliflozin Reduces Epicardial Fat Accumulation in Non-Obese Type 2 Diabetic Patients with Visceral Obesity: A Pilot Study. *Diabetes Ther*. 2017;8(4):851-861. doi:10.1007/s13300-017-0279-y

209. Yagi S, Hirata Y, Ise T, et al. Canagliflozin reduces epicardial fat in patients with type 2 diabetes mellitus. *Diabetol Metab Syndr*. 2017;9(1):78. doi:10.1186/s13098-017-0275-4

210. Aragón-Herrera A, Moraña-Fernández S, Otero-Santiago M, et al. The lipidomic and inflammatory profiles of visceral and subcutaneous adipose tissues are distinctly regulated by the SGLT2 inhibitor empagliflozin in Zucker diabetic fatty rats. *Biomedicine & Pharmacotherapy*. 2023;161:114535. doi:10.1016/j.biopha.2023.114535

211. Yang X, Liu Q, Li Y, et al. Inhibition of the sodium–glucose co-transporter SGLT2 by canagliflozin ameliorates diet-induced obesity by increasing intra-adipose sympathetic innervation. *British Journal of Pharmacology*. 2021;178(8):1756-1771. doi:10.1111/bph.15381

212. Yaribeygi H, Atkin SL, Butler AE, Sahebkar A. Sodium–glucose cotransporter inhibitors and oxidative stress: An update. *Journal of Cellular Physiology*. 2019;234(4):3231-3237. doi:10.1002/jcp.26760

213. Lee TM, Chang NC, Lin SZ. Dapagliflozin, a selective SGLT2 Inhibitor, attenuated cardiac fibrosis by regulating the macrophage polarization via STAT3 signaling in infarcted rat hearts. *Free Radical Biology and Medicine*. 2017;104:298-310. doi:10.1016/j.freeradbiomed.2017.01.035

214. Serbulea V, Upchurch CM, Schappe MS, et al. Macrophage phenotype and bioenergetics are controlled by oxidized phospholipids identified in lean and obese adipose tissue. *Proc Natl Acad Sci USA*. 2018;115(27):E6254-E6263. doi:10.1073/pnas.1800544115

215. Leccisotti L, Cinti F, Sorice GP, et al. Dapagliflozin improves myocardial flow reserve in patients with type 2 diabetes: the DAPAHEART Trial: a preliminary report. *Cardiovasc Diabetol*. 2022;21:173. doi:10.1186/s12933-022-01607-4

216. Adingupu DD, Göpel SO, Grönros J, et al. SGLT2 inhibition with empagliflozin improves coronary microvascular function and cardiac contractility in prediabetic ob/ob−/− mice. *Cardiovasc Diabetol*. 2019;18(1):16. doi:10.1186/s12933-019-0820-6

217. Borlaug BA. The pathophysiology of heart failure with preserved ejection fraction. *Nat Rev Cardiol*. 2014;11(9):507-515. doi:10.1038/nrcardio.2014.83

218. Ambale-Venkatesh B, Armstrong AC, Liu CY, et al. Diastolic function assessed from tagged MRI predicts heart failure and atrial fibrillation over an 8-year follow-up period: the multi-ethnic study of atherosclerosis. *Eur Heart J Cardiovasc Imaging*. 2014;15(4):442-449. doi:10.1093/ehjci/jet189

219. Bogdan C, Röllinghoff M, Diefenbach A. The role of nitric oxide in innate immunity: NO in innate immunity. *Immunological Reviews*. 2000;173(1):17-26. doi:10.1034/j.1600-065X.2000.917307.x

220. Perreault M, Marette A. Targeted disruption of inducible nitric oxide synthase protects against obesity-linked insulin resistance in muscle. *Nat Med*. 2001;7(10):1138-1143. doi:10.1038/nm1001-1138

221. Gilson WD, Epstein FH, Yang Z, et al. Borderzone Contractile Dysfunction Is Transiently Attenuated and Left Ventricular Structural Remodeling Is Markedly Reduced Following Reperfused Myocardial Infarction in Inducible Nitric Oxide Synthase Knockout Mice. *Journal of the American College of Cardiology*. 2007;50(18):1799-1807. doi:10.1016/j.jacc.2007.07.047

222. Schiattarella GG, Alcaide P, Condorelli G, et al. Immunometabolic mechanisms of heart failure with preserved ejection fraction. *Nat Cardiovasc Res*. 2022;1(3):211-222. doi:10.1038/s44161-022-00032-w

223. Chen R, Zhang H, Tang B, et al. Macrophages in cardiovascular diseases: molecular mechanisms and therapeutic targets. *Sig Transduct Target Ther*. 2024;9(1):130. doi:10.1038/s41392-024-01840-1

224. Vilela VR, Samson N, Nachbar R, et al. Adipocyte-specific Nos2 deletion improves insulin resistance and dyslipidemia through brown fat activation in diet-induced obese mice. *Molecular Metabolism*. 2022;57:101437. doi:10.1016/j.molmet.2022.101437

225. Daou D, Gillette TG, Hill JA. Inflammatory Mechanisms in Heart Failure with Preserved Ejection Fraction. *Physiology*. 2023;38(5):217-230. doi:10.1152/physiol.00004.2023

226. Weisberg SP, McCann D, Desai M, Rosenbaum M, Leibel RL, Ferrante AW. Obesity is associated with macrophage accumulation in adipose tissue. *J Clin Invest*. 2003;112(12):1796-1808. doi:10.1172/JCI200319246

227. Lu M, Li P, Olefsky JM. Inducible Nitric Oxide Synthase Deficiency in Myeloid Cells Does Not Prevent Diet-Induced Insulin Resistance.

228. Miyoshi T, Li Y, Shih DM, et al. Deficiency of inducible NO synthase reduces advanced but not early atherosclerosis in apolipoprotein E-deficient mice. *Life Sciences*. 2006;79(6):525-531. doi:10.1016/j.lfs.2006.01.043

229. Kingery JR, Hamid T, Lewis RK, et al. Leukocyte iNOS is required for inflammation and pathological remodeling in ischemic heart failure. *Basic Res Cardiol*. 2017;112(2):19. doi:10.1007/s00395-017-0609-2

230. Gredic M, Wu CY, Hadzic S, et al. Myeloid-cell-specific deletion of inducible nitric oxide synthase protects against smoke-induced pulmonary hypertension in mice. *Eur Respir J*. 2022;59(4):2101153. doi:10.1183/13993003.01153-2021

231. Heger J, Gödecke A, Flögel U, et al. Cardiac-Specific Overexpression of Inducible Nitric Oxide Synthase Does Not Result in Severe Cardiac Dysfunction. *Circulation Research*. 2002;90(1):93-99. doi:10.1161/hh0102.102757

232. Abegunewardene N, Schmidt KH, Vosseler M, et al. Gene therapy with iNOS enhances regional contractility and reduces delayed contrast enhancement in a model of postischemic congestive heart failure. *Clinical Hemorheology and Microcirculation*. 2011;49(1-4):271-278. doi:10.3233/CH-2011-1477

233. Sava R, Pepine C, March K. Immune Dysregulation in HFpEF: A Target for Mesenchymal Stem/Stromal Cell Therapy. *JCM*. 2020;9(1):241. doi:10.3390/jcm9010241

234. Hill AA, Reid Bolus W, Hasty AH. A decade of progress in adipose tissue macrophage biology. *Immunol Rev*. 2014;262(1):134-152. doi:10.1111/imr.12216

235. Peterson P, Svensson J, Månsson S. Relaxation effects in MRI-based quantification of fat content and fatty acid composition. *Magnetic Resonance in Medicine*. 2014;72(5):1320-1329. doi:10.1002/mrm.25048

236. Alharbi SH. Anti-inflammatory role of glucagon-like peptide 1 receptor agonists and its clinical implications. *Therapeutic Advances in Endocrinology*. 2024;15:20420188231222367. doi:10.1177/20420188231222367

237. Singh A, Singh R. Gender difference in cardiovascular outcomes with SGLT-2 inhibitors and GLP-1 receptor agonist in type 2 diabetes: A systematic review and meta-analysis of cardio-vascular outcome trials. doi:https://doi.org/10.1016/j.dsx.2020.02.012

238. Rivera FB, Tang VAS, De Luna DV, et al. Sex differences in cardiovascular outcomes of SGLT-2 inhibitors in heart failure randomized controlled trials: A systematic review and meta-analysis. *American Heart Journal Plus: Cardiology Research and Practice*. 2023;26:100261. doi:10.1016/j.ahjo.2023.100261

239. Lumish HS, O'Reilly M, Reilly MP. Sex Differences in Genomic Drivers of Adipose Distribution and Related Cardiometabolic Disorders: Opportunities for Precision Medicine. *ATVB*. 2020;40(1):45-60. doi:10.1161/ATVBAHA.119.313154

List of Abbreviations

HFpEF	Heart failure with preserved ejection fraction
CMD	Coronary microvascular disease
EAT	Epicardial adipose tissue
MRI	Magnetic resonance imaging
SGLT2	Sodium-glucose cotransporter-2
NOS2	Inducible nitric oxide synthase
SFA	Saturated fatty acid
MUFA	Monounsaturated fatty acid
PUFA	Polyunsaturated fatty acid
SAT	Subcutaneous adipose tissue
CMR	Cardiac MRI
EMPA	Empagliflozin
HFHSD	High-fat high-sucrose diet
MPR	Myocardial perfusion reserve
NMR	Nuclear magnetic resonance
RF	Radiofrequency
FT	Fourier Transform
FOV	Field-of-view
GRE	Gradient echo
TE	Echo time
IR	Inversion recovery
TI	Inversion time
MOLLI	Modified look locker inversion recovery
PDFF	Proton density fat fraction
ndb	Number of double bonds

nmidb	Number of methylene-interrupted double bonds
cl	Chain length
FAC	Fatty acid composition
HF	Heart failure
EF	Ejection fraction
HFrEF	Heart failure with reduced ejection fraction
LV	Left ventricular
NO	Nitric oxide
nNOS	Neuronal nitric oxide synthase
eNOS	Endothelial nitric oxide synthase
PET	Positron emission tomography
CFR	Coronary flow reserve
HFD	High-fat diet
BMI	Body mass index
VAT	Visceral adipose tissue
WHtR	Waist-to-hip ratio
TLR4	Toll-like receptor 4
TNF-α	Tumor necrosis factor-alpha
FAI	Fat attenuation index
SD	Standard diet
DENSE	Displacement encoding with stimulated echoes
ASL	Arterial spin labeling
DIR	Double inversion recovery
FLASH	Fast low angle shot
EDV	End-diastolic volume
ESV	End-systolic volume

EDWT	End-diastolic wall thickness
ESWT	End-systolic wall thickness
MBF	Myocardial blood flow
ECG	Electrocardiogram
UFA	Unsaturated fatty acid
SVHT	Singular value hard thresholding
NUFFT	Non-uniform fast Fourier transform
HOSVD	Higher-order singular value decomposition
SVD	Singular value decomposition
HR	Heart rate
FCM	Fuzzy C-means
Gd	Gadolinium
BW	Bandwidth
ROI	Region-of-interest
MAE	Mean absolute error
SSIM	Structural similarity
H&E	Hematoxylin and eosin
GM-CSF	Granulocyte-macrophage colony-stimulating factor
IL	Interleukin
LIF	Leukemia inhibitor factor
MIP-1a	Macrophage inflammatory protein 1-alpha
GLP-1RA	Glucagon-like peptide-1 receptor agonists
PDSR	Peak diastolic strain rate
TR	Repetition time
AUC	Area under the curve
VSMC	Vascular smooth muscle cell

SNP	Sodium nitroprusside
RM	Repeated measures
ANOVA	Analysis of variance